1-1-2022

Development Of Silicon-Based Anodes With Coal-Derived Materials For High-Performance Lithium-Ion Batteries

Shuai Xu

DEVELOPMENT OF SILICON-BASED ANODES WITH COAL-DERIVED MATERIALS FOR HIGH-PERFORMANCE LITHIUM-ION BATTERIES

by

Shuai Xu

Master of Science, Guangxi University, China, 2016

Bachelor of Science, Hainan University, China, 2012

A Dissertation

Submitted to the Graduate Faculty

of the

University of North Dakota

in partial fulfillment of the requirements

for the degree of

Doctor of Philosophy

Grand Forks, North Dakota

August

2022

Name: Shuai Xu

Degree: Doctor of Philosophy

This document, submitted in partial fulfillment of the requirements for the degree from the University of North Dakota, has been read by the Faculty Advisory Committee under whom the work has been done and is hereby approved.

DocuSigned by:
Xiaodong Hou
E7615FCEEED945B...
Name of Chairperson

DocuSigned by:
Michael Mann
46F0545EE5FF405...
Name of Co-Chair/Committee Member 2

DocuSigned by:
Yun Ji
DAF32AD915374F8...
Name of Member 3 - delete if not needed

DocuSigned by:
Nuri Oncel
F42D61CB47C3491...
Name of Member 4 - delete if not needed

Name of Member 5 - delete if not needed

DocuSigned by:
Dr. Julia Xiaojun Zhao
130DD6CE7E0643D...
Name of Member 6 - delete if not needed

This document is being submitted by the appointed advisory committee as having met all the requirements of the School of Graduate Studies at the University of North Dakota and is hereby approved.

DocuSigned by:
Chris Nelson
2E0AF088C733403...
Chris Nelson
Dean of the School of Graduate Studies

7/26/2022
Date

PERMISSION

Title	Development of Silicon-based Anodes with Coal-Derived Materials for High-Performance Lithium-Ion Batteries
Department	Institute for Energy Studies
Degree	Doctor of Philosophy

In presenting this document in partial fulfillment of the requirements for a graduate degree from the University of North Dakota, I agree that the library of this University shall make it freely available for inspection. I further agree that permission for extensive copying for scholarly purposes may be granted by the professor who supervised my dissertation work or, in his/her absence, by the Chairperson of the department or the dean of the School of Graduate Studies. It is understood that any copying or publication or other use of this dissertation or part thereof for financial gain shall not be allowed without my written permission. It is also understood that due recognition shall be given to me and to the University of North Dakota in any scholarly use which may be made of any material in my dissertation.

Shuai Xu
Date: August 2022

Abbreviations

CFA	Coal fly ash
CMC	Carboxymethyl cellulose
CTAB	Cetyltrimethyl ammonium bromide
CTP	Coal tar pitch
DDBAC	Dodecyl dimethyl benzyl ammonium chloride
DMC	Dimethyl carbonate
D-SiO@G	Disproportionated SiO with graphene coating
EC	Ethylene carbonate
EMC	Ethyl methyl carbonate
FEC	Fluoroethylene carbonate
FEC	Fluoroethylene carbonate
HA	Humic acid
HPSi@C	Hollow porous silicon with carbon coating
HPSi@C	Hollow porous Si with carbon coating
HS-CTP	High softening point coal tar pitch
ICE	Initial coulombic efficiency
LIB	Lithium-ion battery
LS-CTP	Low softening point coal tar pitch

mAh	Milli ampere-hour
mpSi@C	Microsized porous silicon with carbon coating
MR reaction	Magnesiothermic reduction reaction
MS-CTP	Medium softening point coal tar pitch
PDDA	Polydiallyldimethylammonium chloride
PEG 4000	Polyethylene glycol 4000
rGO	Reduced graphene oxide
SDBS	Sodium dodecylbenzene sulfonate
SEI	Solid electrolyte interface
SEM	Scanning electron microscope
SiO/G/C	SiO and graphite with carbon coating
TEM	Transmission electron microscope
VC	Vinylene carbonate
XRD	X-ray powder diffraction

TABLE OF CONTENT

LIST OF FIGURES

LIST OF TABLES

ACKNOWLEDGMENTS

Without the support from my advisors, my advisory committee members, faculty from the IES and the university-wide, as well as my friends and family over the past four years, I would have not reached this stage.

I would like to give my sincere gratitude to my supervisor Dr. Xiaodong Hou who make this work possible. His invaluable advice and patient guidance carried me through the study.

I would like to gratefully thank my director Dr. Michael Mann and Dr. Daniel Laudal for their trust and support. I appreciate all they has done for me.

I would like to express my sincere appreciation to Dr. Julia Xiaojun Zhao for her guidance and help in both my research and daily life. I cannot thank you enough for all that you have done for me.

Many thanks are also given to my committee members: Dr. Yun Ji and Dr. Nuri Oncel for their guidance and help during my studies. Thank Dr. Yong Hou and Dr. Jin Zhang for giving me the support in my research and my life.

I would like to extend thanks to the IES members. They are Dr. Johannes George Van Der Watt, Dr. Laudal Danel, Mr. Harry Feilen, Dr. Brittany Rew, Dr. Olusegun Tomomewo, Ms. Teagan Nelson, Dr. Nicholas Dyrstad-Cinotta, Dr. Theaker Nolan, and Ms. Angie Olson. I appreciate their technical and financial support.

The support from the UND graduate school, the College of Engineering & Mines, the United States Department of Energy, the National Energy Technology Laboratory, NDSU, and the Canadian Light Source is greatly appreciated.

Finally, I would like to thank my parents for their enduring love and support to make all these possible.

ABSTRACT

The increasing demands on high energy density and long cycling life in electronics and energy storage systems require lithium-ion batteries (LIBs) with higher capacity anodes to replace the present commercial anode, graphite, which has a limited capacity of only 372 mAh g^{-1}. Silicon-based materials (silicon and silicon suboxides) are among the most attractive alternative because of their high theoretical capacity but can hardly reach commercialization due to numerous technical and engineering barriers. The effort in this dissertation focuses on improving the electrochemical performance of SiO and Si anode materials, trying to pave a way to a greener and cleaner energy industry. A total of 5 projects (from Chapter II to ChapterVI) are included in this dissertation as follows.

The first chapter introduces the background and challenges in the development of anode materials for LIBs, followed by the motivation of my work in the years of pursuing the Ph.D. degree.

In Chapter II, low-cost coal-derived humic acid (HA) is used as a feedstock to synthesize in situ graphene-coated disproportionated SiO (D-SiO@G) anode with a facile method. HR-TEM and XRD confirm the well-coated graphene layers on a SiO surface. Scanning transmission X-ray microscopy and X-ray absorption near-edge structure spectra analyses indicate that the graphene coating effectively hinders the side-reactions between the electrolyte and SiO particles. As a result, the D-SiO@G anode presents an initial discharge capacity of 1937.6 mAh g^{-1} at 0.1 A g^{-1} and an initial coulombic efficiency of 78.2%. High

reversible capacity (1023 mAh g^{-1} at 2.0 A g^{-1}), excellent cycling performance (72.4% capacity retention after 500 cycles at 2.0 A g^{-1}), and ratecapability (774 mAh g^{-1} at 5 A g^{-1}) results are substantial. Full coin cells assembled with $LiFePO_4$ electrodes and D-SiO@G electrodes display impressive rate performance. These results indicate promising potential for practical use in high-performance lithium-ion batteries. In addition, the effect of particle size and carbon content on the electrochemical performance of the SiO@G anode is also analyzed.

In Chapter III, the microstructure and composition evolution in amorphous SiO and graphene-coated SiO is investigated using different heat-treatment conditions. X-ray absorption near-edge structure techniques are also employed to analyze the surface and bulk composition change during the initial lithiation process, supplemented by physical or chemical characterization and electrochemical testing. The results reveal the structural transition of SiO during heat treatment, from amorphous to disproportionated hierarchical structure, where the as-formed dielectric exterior SiO_2 shell and interior SiO_2 matrix severely polarize electrodes, hindering the lithiation process. Carbon coating on SiO effectively restricts the growth of the SiO_2 shell and facilitates charge transfer, leading to improved electrochemical performance. A schematic model is proposed to reveal the relationship between the treatments, the resultant structural evolutions, and corresponding electrochemical behaviors.

Chapter IV depicts the work of using lignite-derived coal tar pitch to develop high-performance SiO/C/Gr anode composites. Two synthesis routes using high softening point pitch and low softening point pitch with SiO anode are discussed separately. Benefiting from the LS-CTP coating, the SiO/G/C composite shows a long cycle life with 84.5%

capacity retention after 500 cycles. The SiO/C composite synthesized by HS-CTP also shows a high reversible capacity (~1000 mAh g^{-1} at 2.0 A g^{-1}) with a considerable cycle life (85% capacity retention after 200 cycles).

In Chapter V, SiO_2 nanoparticles (nano-SiO_2) and low-cost coal-derived HA are used as feedstock, by magnesiothermic reduction and spray drying, to synthesize micrometer-sized porous Si coated with graphitized carbon shell (mpSi@C). Our Si-C anodes feature micrometer-sized porous Si coated with a graphitized carbon shell. The hierarchical graphitized carbon shell and porous silicon structure relieve the mechanical stress of the Si phase upon cycling, which stabilizes the structure. This mpSi@C composite design allows for a high initial discharge capacity of 2199.9 mAh g^{-1} at 0.1 A g^{-1} and a cycling performance of 68% capacity retention after 100 cycles at 1.0 A g^{-1}. The multipoint contact between the Si anode and C structure allows for a remarkable performance rate of 566.3 mAh g^{-1} at 5.0 A g^{-1}.

In Chapter VI, coal fly ash is used to replace SiO_2 nanoparticles as a low-cost feedstock and structure template to in-situ synthesize hierarchical hollow porous Si@C composites. The hollow and porous structure allows the Si anode to expand and contract freely during lithiation and delithiation. The in-situ synthesized tough carbon coating acts as an effective electrolyte barrier and structure sustainer to keep the electrochemical performance composites from decaying during long-time cycling. As a result of this hierarchical design, the synthesized HP Si@C composite presents an initial discharge capacity of 2502.3 mAh g^{-1} at 0.05 A g^{-1} and initial coulombic efficiency (ICE) of 81.7%. Besides, the multipoint contact between the Si anode and C shell leads to excellent rate performance even with high mass loads.

CHAPTER I

RESEARCH INTRODUCTION

1.1. Background – Anode Materials for Lithium-Ion Batteries

Lithium-ion (Li-ion) batteries (LIBs) are a type of rechargeable battery comprised of cathode electrodes, anode electrodes, separators, and electrolytes, where Li-ions exist as the energy transmission medium.[1-2] Compared with traditional batteries, such as Lead-acid batteries, LIBs possess much higher energy density, longer cycle life, and lower self-discharge.[3-4] Since its invention in 1991 by the Sony company, LIBs have been attracting intensive studies to improve their electrochemical performance.[5] The energy of a battery can be primarily calculated by its output voltage and specific capacity (Equation 1), which is determined by its cathode and anode materials:

$$E = \int \Delta U \times Idt = Q \times \Delta U \qquad \text{Equation 1}$$

Cathode materials have experienced a wide development (Table 1.1), with a steady increase in practical capacity from 145 mAh g^{-1} of $LiCoO_2$, 165 mAh g^{-1} of $LiFePO_4$, 170 mAh g^{-1} of NMC111, and 200 mAh g^{-1} of NMC811.[6-7] Less dramatic improvements have been achieved in the anode part, where graphite has been dominating for more than 30 years with a limited capacity of 372 mAh g^{-1}, which can hardly meet the urgent demand for high energy density batteries. Up to now, many higher Li storage anode materials based on alloying, such as Si (4200 mAh g^{-1}), Sn (960 mAh g^{-1}), P (2596 mAh g^{-1}), Ge (1600

mAh g^{-1}), as well as transition metal oxides based on conversion have been discovered.[6] However, none of them have reached mass commercialization.

Table 1. 1. Characteristics of representative cathode compound.

Materials	**Commercial capacity (mAh g^{-1})**	**Average voltage (V)**	**Level of Development**
$LiCoO_2$	145	3.8	Commercialized
$LiMn_2O_4$	120	4.1	Commercialized
$LiFePO_4$	165	3.4	Commercialized
NMC111 ($LiNi_{0.33}Mn_{0.33}Co_{0.33}$)	170	3.7	Commercialized
NMC811 ($LiNi_{0.8}Co_{0.1}Mn_{0.1}$)	200	3.8	Commercialized

1.2. Silicon Anode Materials

Table 1. 2. Properties of anode materials.

Materials	**Average Voltage (V)**	**Commercial capacity (mAh g^{-1})**	**Volume Change**	**Cyclability**
Graphite	0.1	370	10%	Excellent
Si	0.3	4200	300%	Terrible
SiO	0.3	2400	100%	Good

Silicon (Si) anodes are among the most attractive alternative mainly because of their high theoretical capacity,[8] wide availability, and low delithiation potential. It is consensus that

the alloy reaction can achieve much more capacity compared with the intercalation reaction. Graphite's capacity is from its intercalation reaction with Li, forming the compound LiC_6. In contrast (Table 1.2), Si can react with Li to form $Li_{22}Si_5$ alloy, delivering a much higher theoretical capacity of 4200 mAh g^{-1}.[9] However, the huge capacity of Si is paid for by its drastic volume change during lithiation and delithiation (approximately 400%, V/V_o), which pulverizes Si particles and subsequently makes them lose electrical contact with current collectors.[10-11] Moreover, the side reaction between Si and electrolytes forms the solid-electrolyte interphase (SEI), which is vulnerable in the following cycling and keeps consuming the electrolyte, resulting in a thick SEI and deteriorated Li^+ transport. All these problems combined lead to low cycling efficiency and rapid capacity loss.

So far, plenty of approaches have been proposed to address the above problems:

1) Nano-sized silicon. Si nanolization is widely considered to be one of the most effective solutions as Si with a nanometer-sized diameter (D < 150 nm) had been demonstrated to survive cycling without pulverization[12-13]. Nano-Si also decreases the diffusion length for lithium ions, leading to excellent rate capability[14-16]. Based on this, numerous types of nanowires,[17] nanotubes,[18-19] and nanospheres[20] have been synthesized and demonstrated to have improved performance. Nevertheless, these nano-Si structures are accompanied by enlarged surface areas, which enhances the side reactions between Si and electrolytes. Moreover, the synthesis of nano-Si requests complicated and strict processes, making nano-Si very expensive and less practical for mass production.[21]
2) Porous silicon. Compared to nano-silicon, porous silicon, which is taken as clusters of a great quantity of nano-Si particles and voids, has some unique advantages: smaller

surface area, much lower viscosity, and better thermodynamic stability.[11, 22] The voids in the porous structure accommodate silicon expansion and contraction freely during the lithiation/delithiation process.[11, 23-24] These merits attract a large amount of interest in exploring the synthetic processes of porous silicon anodes for LIBs.[25-28] Among them, the magnesiothermic reduction (MR reaction) of SiO_2 is considered a promising method to synthesize porous silicon for its much lower reaction temperatures than conventional silicon productions and controllable porosity.[29-31] Nanosized-porous and microsized-porous Si structures synthesized by MR reaction have been reported to have considerable cycling performance.[22, 32] However, one defect of the nano-porous structure is its severe consumption of the electrolyte due to the large surface area, leading to a low ICE. Microsized porous Si has a higher ICE as a result of a smaller surface area, however, its mechanical strength is also limited due to its much larger size than that of nano-porous Si, making it easier to fracture during cycling.[32]

3) Electrolyte additives. The huge volume change of Si during cycling breaks the SEI film repeatedly and causes the continuous formation of the SEI films. Apart from the structural designs, electrolyte design is focused on restricting the SEI growth during cycling and forming stable and robust SEI films. Some effective electrolyte additives, such as VC (Vinylene carbonate) and FEC (Fluoroethylene carbonate),[33] have been developed by the mechanism of reductive reactions to protect electrolyte solvents from decomposition, resulting in better cycle life. These findings are inspiring but still not good enough to make Si anode practical. New additives with higher reductive potential, high chemical compatibility, and good film-forming characteristics are urgently needed to further improve the stability of the interface between electrolytes and Si anodes.[34]

4) Binders. The repeated volume expansion and shrinkage of Si not only pulverize Si itself but also result in the delamination of Si from the current collector. The delaminated Si particles are electrically isolated from the battery circuit and lead to huge capacity loss. Well-designed binders with the properties of high elasticity,[35] mechanically robust,[36] and self-healing[37] have been developed and show a promising future in the LIB industry. Although the binders alone cannot solve Si's problems, high-performance binders can significantly alleviate the side effects of pulverization and simplify the complicated and costly synthesis process.[38]

1.3. SiO Anode Materials

Silicon monoxide (SiO) possesses a compromised theoretical capacity of ~ 2400 mAh g^{-1},[39] with a much smaller volume expansion (~ 200%), making it more practical for LIBs when compared to Si alone;[40-41] however, due to the uncommon valence state of silicon, an accurate structural model of the SiO materials remains controversial after decades of experimental and theoretical efforts.[42] Two structural models, the random-mixture (RM) and random-bonding (RB) were proposed to address SiO's composition and valence distribution.[43] The RM model posits that SiO exists as a stoichiometric mixture of amorphous SiO_2 and amorphous Si,[44] while the RB model posits that silicon exists with the valence of 0 to +4 randomly connecting the oxygen atoms.[45] A recent study indicates that Si nanoclusters (Si^0) are surrounded by an amorphous SiO_2 matrix (Si^{4+}). Some silicon exists with valences of +1, +2, and +3 in their interfacial regions.[46] SiO's unique composition and structure allow it to deliver better cycling performance than Si anodes. The reason for that is the amorphous SiO_2 matrix reacts with Li-ions (Equation 2) in the initial lithiation process (Figure 1.1), forming irreversible Li_2O and Li silicates. Both can

act as a buffer phase that effectively alleviates the significant volume change of the Si nanoclusters.[47]

$$SiO + Li \rightarrow Li_xSi_y + Li_2O + Li\ Silicates \qquad \text{Equation 2}$$

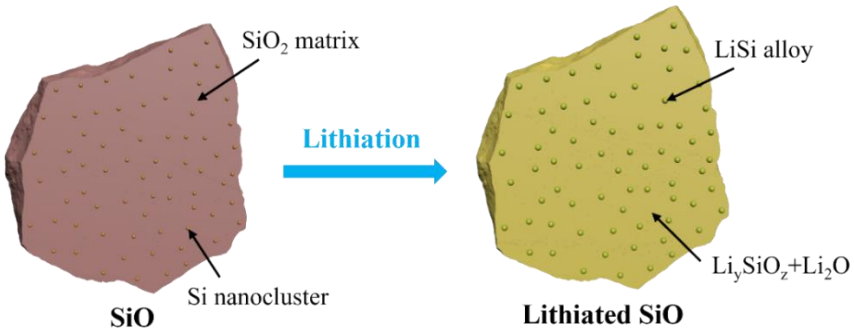

Figure 1. 1. Schematic illustration of the initial lithiation of SiO anode materials.

On the other hand, the irreversible reactions in the initial lithiation process also lead to a low initial coulombic efficiency (ICE).[48-49] Some other barriers include the intrinsic inferior electrical conductivity, the electrical isolation effect caused by volume changes during cycling,[50-51] and considerable side reactions with electrolytes.[52-53] These issues on SiO are not as severe as on Si anode and they have similar solutions, but still prevent the mass commercialization of SiO in LIBs.[54]

1.4. Graphene Coating

Apart from the aforementioned approaches to surmount the barriers on the way to the commercialization of Si and SiO anodes, some effective methods, including conductive coating,[55-56] structural design,[57-58] and chemical etching,[59-60] have been performed. Graphene coating is taken as one of the most effective ways to improve the electrochemical performance of Si-based (Si and SiO) anode materials. This coating can significantly increase electronic conductivity and prevent the reactions between Si and electrolytes.[61-62]

A multilayered graphene shell with excellent resilience and much higher conductivity can effectively accommodate the volume expansion of Si via a sliding process between adjacent layers without breaking the graphene shell.[63-66] Two approaches are frequently used to prepare Si and graphene composites: externally mixing Si with graphene, or reduced graphene oxide (rGO), and in-situ synthesis of graphene on the surface of the Si-based anode particles. The method of mixing Si with graphene has been extensively reported in other peer-reviewed journal articles. Xu et al.[67] used conductive rGO bubble films to capture SiO_x nanoparticles by electrostatic interaction. The synthesized SiO_x@G delivered excellent cycling performance, up to an 80% capacity retention after 1,000 cycles; however, rGO is generally produced under the harsh conditions of Hummers' method, which brings severe environmental issues. the complicated synthetic process of rGO is also accompanied by a significant increase in production cost, which limits its mass application in LIBs. Moreover, graphene sheets used as the coating material mostly possess a size of tens micrometers with very few functional groups, which limits its multi-contact with Si-based anode particles.[68] The poor contact offset the graphene's excellent conductivity. To make things worse, the large size of the graphene sheet severely blocks Li-ion from transporting, resulting in limited improvement in electrochemical performance.[69] Instead, in-situ synthesis of graphene on the surface of active material particles is expected to solve these issues and make graphene coating practical. Li et al.[70] synthesized in-situ graphene cages by catalyzing Ni to encapsulate Si microparticles, as one example. This process resulted in the graphene cage allowing the Si microparticles to expand while retaining electrical connectivity, showing a stable cyclability of 90% retention after 100 cycles. However, the existing reports of in-situ graphene synthesis

usually involve metallic catalysts, the complete removal of which is a significant challenge. Chemical vapor deposition (CVD) and other plasma-assistant methods can produce high-quality graphene, but those technologies remain costly due to the limit of production capacity.[55-56, 64]

1.5. Research Hypothesis and Significance

Coal is an abundant and low-cost sedimentary rock composed predominantly of carbon that has been demonstrated to be a promising material for a variety of applications.[71-72] It is formed from buried plant matter by coalification, during which buried plant matter changes from cellulose, which consists of glucose (Figure 1.2), through peat, lignite, and bituminous coal to anthracite.[73] Under extreme conditions, anthracite can change to graphite. In these changes, high temperature and pressure remove functional groups (mostly H and O) and aggregate C into benzene rings. The removal of H and O elements is accompanied by a decrease in solubility. When the coalification process comes to the anthracite, the benzene rings bond together tightly, just as graphite, making it insoluble and difficult to break into graphene.

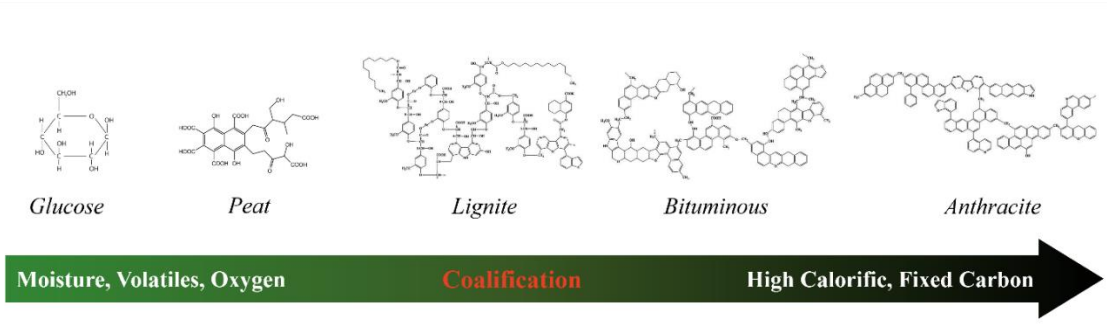

Figure 1. 2. Schematic of formula changes in the coalification process.

Because of this, low-rank coal, such as lignite, shows its unique value. Unlike graphite, a key characteristic of low-rank coal – in particular, lignite – is its loose intermolecular bonding that is significantly different from the strong intermolecular bonding (Van der Waals forces) within the layer-by-layer structure of graphite. The loose bonding implies the feasibility to produce graphene-like materials with quality comparable to commercial graphene in a facile condition. Moreover, the combustion of coal for energy production also brings plenty of coal byproducts, such as fly ash, gypsum, and slag.[74] Some of these byproducts have been used in the synthesis of soil amelioration agents and catalyst supports due to their unique structure and properties, which fit LIB material research very well.[75-76] With these potential benefits, coal and its derivatives show promising potential in the synthesis of high-performance anode materials at a considerably low cost.

The essential mission of the Institute for Energy Studies (IES) is to facilitate the advancement of energy technologies that are economically competitive, reliable, sustainable, and politically and environmentally acceptable. In recognition of North Dakota's vast energy resources – lignite coal, biomass, and other renewables, I have devoted myself to improving energy density and efficiency in renewable energy systems, aiming to play a positive role in the clean, efficient, and sustainable development of these precious resources.

CHAPTER II

SYNTHESIS OF GRAPHENE-COATED SILICON MONOXIDE ANODES FROM COAL-DERIVED HUMIC ACID FOR HIGH-PERFORMANCE LITHIUM-ION BATTERIES

Statement: This chapter is based in part on the previously published article listed below:

Xu, S.; Zhou, J.; Wang, J.; Pathiranage, S.; Oncel, N.; Robert Ilango, P.; Zhang, X.; Mann, M.; Hou, X., In Situ Synthesis of Graphene-Coated Silicon Monoxide Anodes from Coal-Derived Humic Acid for High-Performance Lithium-Ion Batteries. *Adv. Funct. Mater.* **2021,** *31* (32), 2101645.

2.1. Introduction

When used as the commercial anode material for LIBs, graphite has a limited capacity of 372 mAh g^{-1}, which does not meet the demand for high energy density applications. Silicon monoxide (SiO) is taken as a promising candidate due to its much higher theoretical capacity of ~ 2400 mAh g^{-1} and tolerable cycling performance.[40, 77] SiO can be synthesized by the vapor deposition reaction between Si and SiO_2 at high temperatures and can be modeled as a mixture of amorphous silicon and silica at the nanoscale.[46, 78] The Si-O bond (452 kJ/mol) is two times stronger than a Si-Si bond (223 kJ/mol), which creates a much smaller volume change (200%) during lithiation and delithiation.[40, 77, 79] The as-formed Li_2O and Li silicates during the initial lithiation of SiO act as a buffer to alleviate the expansion and shrinkage of Si clusters, resulting in improved cycling stability.[43, 80-81] Nevertheless, the intrinsic poor electronic conductivity and low initial coulombic

efficiency of SiO leads to poor rate performance and increased capacity decay, hindering its substantial application in LIBs.[47, 78]

Graphene coating is taken as one of the most effective ways to improve the electrochemical performance of SiO anode materials. This coating can significantly increase electronic conductivity and prevent the reactions between SiO and the electrolyte.[61-62] A multilayered graphene shell with excellent resilience and much higher conductivity can effectively accommodate the volume expansion of SiO via a sliding process between adjacent layers without breaking the graphene shell.[63-66] However, most graphene coating approaches either involve complicated synthetic processes or high costs with hazardous environmental impacts.[56] An approach that synthesizes graphene in-situ from low-cost feedstock that can be directly adopted to existing industrial processes for LIB electrode material production, therefore, is highly desired.

Coal is an abundant, cheap resource and has recently been used to prepare nanosized graphene.[72, 82] In these researches, harsh conditions similar to the Hummers' method have been used to create graphene from various types of coal. This method neglects an essential characteristic of coal, particularly low-rank coal such as lignite: loose intermolecular bonding significantly different from the strong intermolecular bonding, or Van der Waals forces, within the layer-by-layer structure of graphite. In low-rank coal, humic acid (HA) is the primary organic matter and one of the most abundant natural carbon resources. Chemically, HA is not a single molecule but a complex mixture of thousands of organic compounds with a wide range of molecular weights, from several hundred to millions.[83] Given the complexity of HA, the exact chemical structure is unclear; however, the basic structure of HA is polyaromatic rings, where two-thirds of the carbon atoms are sp^2 bonded,

with a variety of substitutional groups such as the predominantly carboxyl groups and hydroxyl groups.[84] Recent research indicates that HA can be converted into graphene-like materials with a quality comparable to rGO.[85-86] These approaches require expensive catalyst systems and harsh reaction conditions in a Parr reactor at high temperature and pressure and are not adoptable for use in existing industrial processes for LIB electrode material production.

Herein, we have developed a facile and low-cost route to synthesize an in-situ graphene-coated SiO anode using coal-derived HA as the carbon source (Fig. 1a). The abundant functional groups of HA make it highly soluble in alkali aqueous solutions. This property makes it much more effective to coat SiO particles with HA than using graphene or graphene oxide. HA was evenly coated on the surface of amorphous SiO (P-SiO@HA) in our experiments. The heat treatment performed afterward produced disproportionated SiO while converting HA into graphene coating in situ. Physical and chemical characterization and electrochemical testing were performed to confirm the effectiveness of the design.

2.2. Methods

2.2.1. Synthesis of D-SiO@G: 2.0 g of pristine silicon monoxide (P-SiO) powder (3 – 7 μm, Sigma Aldrich) and 0.5 g of HA, extracted and purified from North Dakota lignite, were mixed in 25 mL of DI water. 2.0 mL of ammonium (28% – 30%, LabChem, USA) was added dropwise into the mixture to completely dissolve the HA. This mixture was stirred for 1 h at room temperature, then elevated to 80 ℃ with continuous stirring to evaporate solvents and precipitate HA on the surface of the SiO particles. The obtained P-SiO@HA precursor was completely ground and sintered at 300 ℃ for 2 h and subsequently at 1000 ℃ for 8 h in a high-purity Ar atmosphere. A disproportionated SiO coated with

graphene (D-SiO@G) composite was obtained when the mixture was cooled to room temperature.

2.2.2. Materials Characterization: X-ray powder diffraction (XRD) was performed on an X-ray diffractometer (Smartlab, Rigaku) operated at 40 kV and 44 mA using Cu Kα radiation at a scan rate of 4°/min from 10° – 80°. The D-SiO@G particle cross-section was made by polishing the powder sample embedded in an epoxy resin on a LaboPol-21 polisher to investigate its internal structure. The particle morphology and element composition were analyzed with a field-emission scanning electron microscope (FEI Quanta 650 FEG SEM) equipped with an energy dispersive X-ray (EDX) spectrometer and field-emission transmission electron microscopy (FE-TEM, JEM-2100F, JEOL, 200 kV). The Raman spectra were collected with a Raman microscope (HORIBA LabRAM HR Evolution, 532 nm, 1800 grating). TEM images were analyzed with Digital Micrograph software to calculate the interplanar spacing of the crystal lattices. The element valence and bonding configuration on the sample's surface was analyzed with X-ray photoelectron spectroscopy (Al Kα, 1486.6 eV, PHI-5400). The carbon content of the D-SiO@G was analyzed with a carbon analyzer (TOC-V, SHIMADZU) with an SSM 5000A module for the solid samples. Thermogravimetric analysis (TGA) was conducted on a TA instrument, SDT Q600, from room temperature to 800 ℃ at 5 ℃ min^{-1} in an Ar atmosphere.

Scanning transmission X-ray microscopy (STXM) and X-ray absorption near-edge structure (XANES) spectroscopy were conducted at the SM beamline of the Canadian Light Source. Coin cells with target electrodes after completing 50 cycles were disassembled in a glove box. The coating powder was scraped off of the cycled target electrodes, dispersed in acetonitrile by brief sonication, and deposited on holey TEM grids

after complete drying under a vacuum. All samples were sealed in argon-filled aluminum composite bags and transferred to the vacuum chamber (10^{-9} Torr base pressure) of the beamline's end station without air exposure. A Fresnel zone plate focused the monochromatic X-ray beam to a 30 nm spot on the sample during testing, and the sample was raster-scanned at the selected sample region with a synchronized detection of transmitted X-rays. This method generated image stacks over a range of photon energy across Si K-edge, C K-edge, and O K-edge at specific sample regions. The acquired STXM data were analyzed by a Xis2000.[87-88]

2.2.3. Electrochemical Measurements: The electrode slurry was prepared by mixing the active material, conductive agent (acetylene black), and binders CMC (Carboxymethyl Cellulose, average weight of 450K, MTI, USA) and SBR (Styrene-Butadiene Rubber, MTI, USA) at a mass ratio of 60:20:8:12 in DI water. This slurry was then coated onto copper foil and dried in a vacuum oven at 100 ℃ overnight. CR2032 coin-type cells were assembled in an Ar-filled glovebox with the active materials as the working electrode, lithium foil as the counter electrode, a Celgard 2400 membrane as the separator, and 1.2 M $LiPF_6$ in EC/DMC/EMC (1/1/1 in wt%) with 10 wt% FEC as the electrolyte. The cells were tested with galvanostatic charge-discharge between 0.001 V and 2.0 V (vs. Li/Li^+) using a Neware Battery Testing System (CT-4008, Neware Technology Limited, Shenzhen. China). The current densities and specific capacities were calculated based on the mass of active materials in the working electrode. Cyclic voltammetry (CV) and electrochemical impedance spectroscopy (EIS) was performed on a Gamry Series G 750 electrochemical workstation (Gamry Instruments, Warminster, USA). CV measurements were conducted within the voltage range of 0.01-2.5V at 0.1 mV S^{-1}. EIS measurements

were completed at an AC voltage amplitude of 10 mV and a frequency from 300 kHz to 0.01 Hz. Full cells were fabricated using the D-SiO@G electrodes and LFP electrodes with an N/P ratio of 1.15. The D-SiO@G anode for full cells was prelithiated in half cells for 20% of its hypothetical capacity in advance.

2.3. Results and Discussion

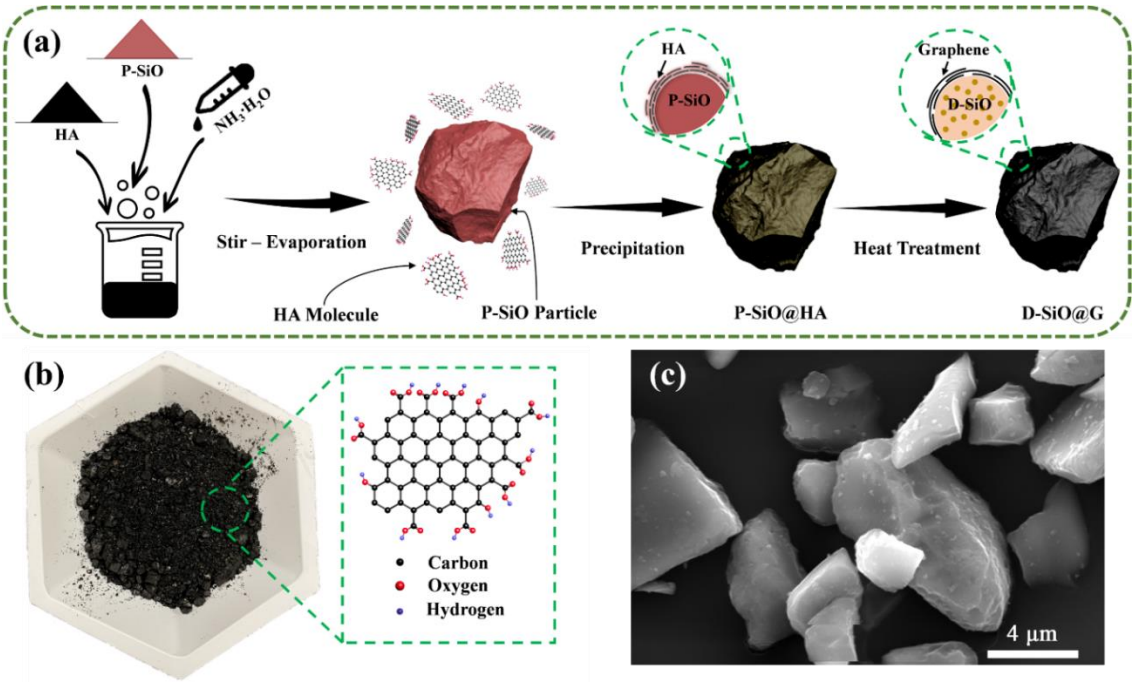

Figure 2. 1. (a) Schematic of the synthetic process of D-SiO@G anode materials. (b) Humic acid (HA) and its typical molecular model. SEM images of (c) Pristine SiO (P-SiO).

Figure 2.1a illustrates the synthesis schematic of the D-SiO@G anode material. The HA used in this work is a dark brown powder (Figure 2.1b), with a typical molecular structure that contains several carboxyl and hydroxyl groups surrounding a graphene-like core.[86] The pristine SiO powder used has a narrow particle size distribution from 3 – 7 μm (Figure 2.1c). While mixing, the added $NH_3 \cdot H_2O$ solution provides an alkaline environment to react with the carboxyl groups of HA, forming a soluble ammonium humate salt. The Zeta potential measurement (Figure 2.2a) indicates that both P-SiO and HA are negatively

charged in the alkaline environment (pH = 10). As a result, the NH_4^+ cations in the suspension of SiO and HA mixture act as electropositive protonated media to connect SiO particles with HA molecules by electrostatic interactions (Figure 2.2b),[67] which drives the deposit of HA coating on the surface of the SiO particles in the evaporation process. After the evaporation of the solvents, a noticeable HA coating was found on the surface of the SiO particles from the SEM image (Figure 2.2c).

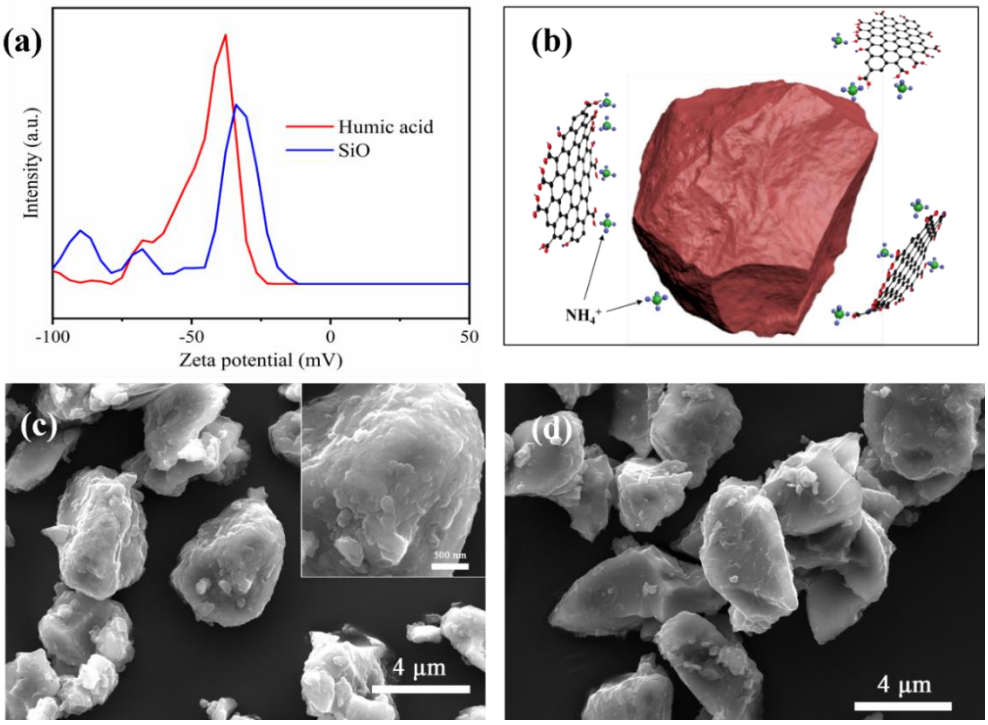

Figure 2. 2. (a) Zeta potential of the HA and SiO suspensions in the alkaline environment (pH = 10). (b) Schematic of NH_4^+ cations connecting HA molecules with a P-SiO particle by electrostatic interactions. (c) SEM image of the P-SiO@HA precursor after the stir-evaporation process (c). (d) SEM image of the D-SiO@G composite.

D-SiO@G displays morphology similar to P-SiO (Figure 2.2d) after heat treatment except for a few carbon lumps that originated from a small amount of excessive HA, indicating a thin and even coating. The D-SiO@G particles were etched with 5% HF solution for 45 min to confirm these findings. The etching occurs on the D-SiO particles, as indicated in

Figure 2.3a, leaving residual D-SiO cores encapsulated by thin graphene shells, which are nearly identical in shape to the unetched D-SiO@G particles. This thin shell preserves its original shape during etching, which implies it is mechanically robust and should prevent the D-SiO particle from fracture during cycling.[89] D-SiO@G is an agglomerate-free powder in contrast to anodes coated by prevalently used carbon sources in the industry such as pitch, in which breaking down the agglomerate after calcination is mandatory. This synthesis procedure is facile and straightforward compared with other in-situ graphene coatings with no toxic reagents, expensive catalysts, or harsh conditions involved.[55, 66, 70]

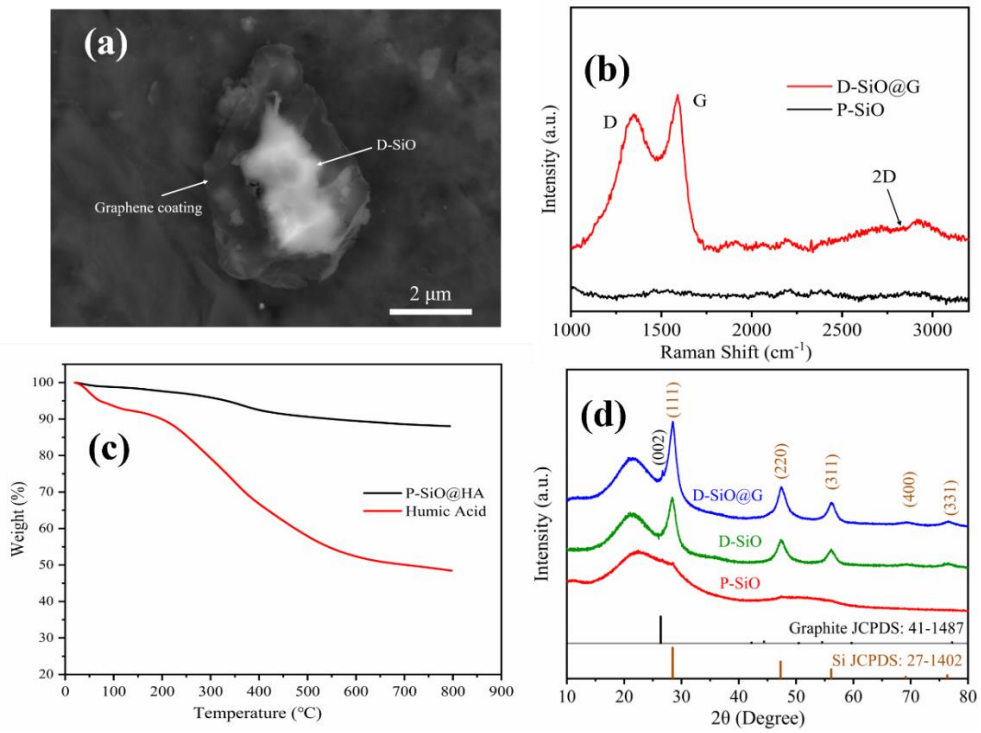

Figure 2. 3. SEM images of (a) HF-etched D-SiO@G particles. Insert shows the backscattered electrons (BSE) image. (b) Raman spectra of P-SiO and D-SiO@G. (c) TGA curves of the HA and SiO@HA precursors at the ramp of 5 °C min^{-1} under an Ar atmosphere. (d) XRD patterns of Pristine SiO, Disproportionated SiO (D-SiO), and D-SiO@G samples.

The nature of this coating was further studied by Raman spectroscopy. The pronounced G-band (1585 cm^{-1}) in Figure 2.3b demonstrates the highly graphitic nature of the in-situ

synthesized graphene shell. The significant D-band (1350 cm^{-1}) indicates many defects, which facilitate Li-ion transport through the shell. Also, the intensive silicon bands in D-SiO@G compared to P-SiO confirm the formation of the Si phase by disproportionation reaction. TGA (Figure 2.3c) was used to investigate the weight change of pure HA and P-SiO@HA over heat treatment. The TGA curve of pure HA exhibits two sharp weight losses in the temperature ranges of room temperature – 150 ℃ and 200 ℃ – 600 ℃. The weight loss at the lower temperature range represents the evaporation of the moisture in HA, and the higher temperature range weight loss can be attributed to the decomposition and volatilization of the functional groups during carbonization. The weight retention of HA is over 55% from 200 ℃ to 800 ℃, which is higher than most carbon sources and would lead to significant mechanical strength and press density due to its chemical structure characteristics.[90-91] Carbon analysis indicates a 9.8% D-SiO@G powder residual carbon content.

The XRD patterns displayed in Figure 2.3d indicate phase changes over the synthetic process. A halo observed at 2θ =15~35° indicates the amorphous nature of SiO with underlying silicon characteristic peaks,[92] which were amplified dramatically in the patterns of both D-SiO and D-SiO@G. These phase changes reflect the thermal disproportionation of amorphous SiO:[81]

$$2SiO \rightarrow Si + SiO_2$$

A small but sharp peak appears at approximately 2θ=26.6° in the D-SiO@G pattern, which can be attributed to the graphitic nature of the coated shells.[66, 92-93] This phase evolution agrees with the Raman spectra analysis results.

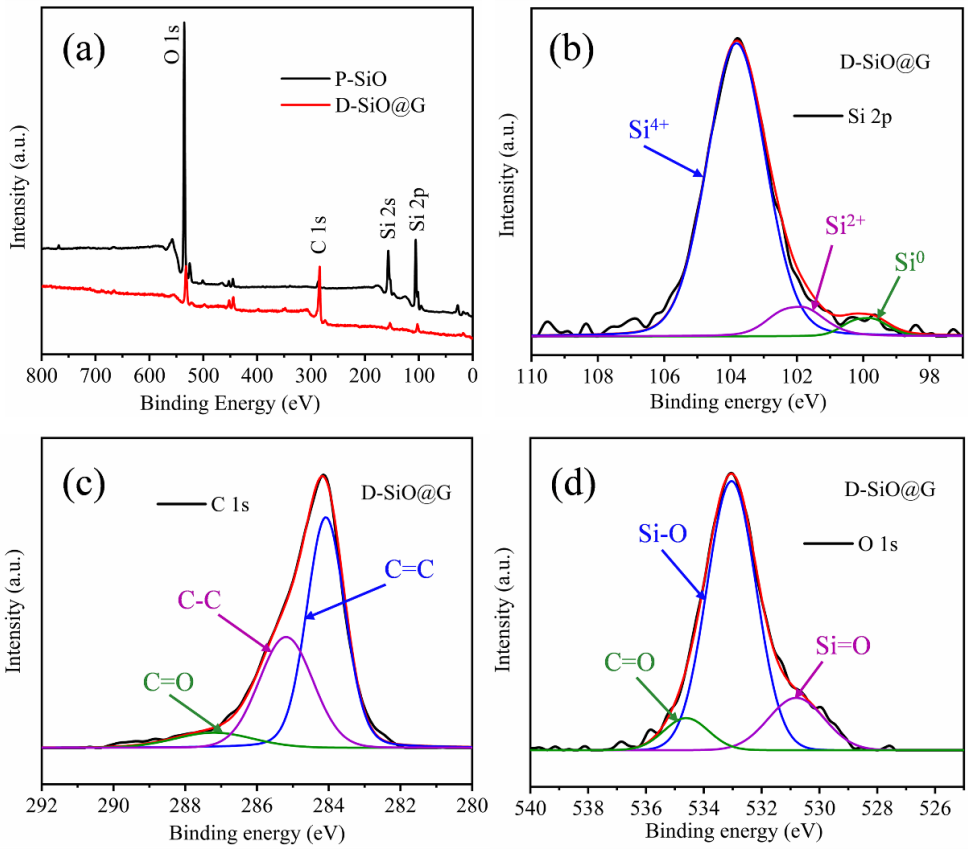

Figure 2. 4. (a) XPS survey spectra of P-SiO and D-SiO@G. (b) Si 2p spectrum of D-SiO@G. (c) C 1s XPS spectrum of D-SiO@G. (d) O 1s XPS spectrum of D-SiO@G.

XPS, as a surface-sensitive spectroscopic technique, was used to investigate the surface chemical features, such as valences and composition, of SiO materials (Figure 2.4). The XPS spectra of P-SiO and D-SiO@G between 800 and 0 eV (Figure 2.4a) indicate an intense C1s peak, but much smaller O1s and Si2p peaks in D-SiO@G compared to that of P-SiO due to effective graphene coating. The Si 2p peak of D-SiO@G is fitted with three subpeaks, corresponding to Si^{4+} (103.8 eV), Si^{2+} (102.0 eV), and Si^{0} (99.8 eV), confirming the existence of the elemental Si phase,[94] as shown in Figure 2.4b. The C1s peak (Figure 2.4c) is deconvoluted into C=C, C-C, and C=O subpeaks. Among these peaks, the significant proportion of the C=C subpeak and relatively smaller C-C subpeaks indicate that the carbon coating is mainly graphitic with some defects.[56] The small C=O peak may

come from CO_2 contamination,[95] or residual carboxylic acid groups of HA. The dominant proportion of the Si^{4+} peak (Figure 2.4b) and Si-O (Figure 2.4d) implies that on the particle surface, amorphous SiO_2 is more abundant than the elemental Si phase, as the detective depth of XPS for solid materials is only a few nanometers.

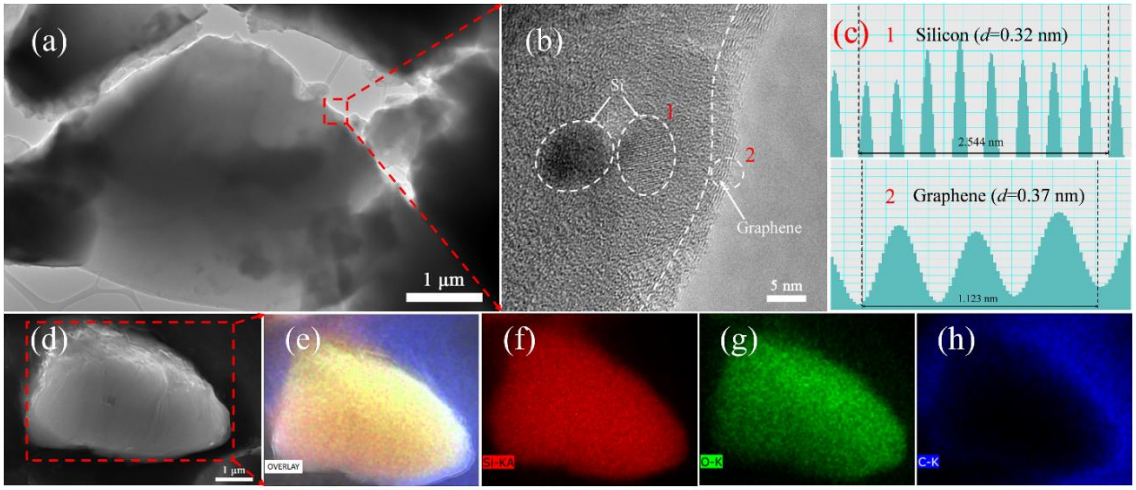

Figure 2. 5. (a, b) The low and high magnification of TEM images of D-SiO@G. (c) The interplanar-spacing of Si nanocrystal and Graphene layers corresponding to areas 1 and 2, respectively. (d) SEM image of the cross-section of a D-SiO@G particle. (e-h) corresponding EDX elemental mapping.

High-resolution transmission electron microscopy (HRTEM) and Energy Dispersive Spectroscopy (EDS) was used to analyze the microstructure and chemical composition of D-SiO@G particles (Figure 2.5). Closer inspection (Figure 2.5b) reveals that the D-SiO particle is coated with an even 5 nm thick graphene shell, confirming the conversion of HA to graphene. The Si nanocrystal clusters can be found embedded in the amorphous phase (SiO_2 matrix). The amorphous SiO_2 matrix can react with Li-ions during lithiation, forming Li_2O and Li silicates, which could alleviate the Si phase's considerable volume change in the following cycles.[77] The interplanar spacing of the Si nanocrystal and coated graphene layers, corresponding to areas 1 and 2, respectively, was measured from the TEM image.

The *d*-spacing of area 1, calculated with the Gatan Digital Micrograph, is ascribed to the interplanar spacing of Si (111) (Figure 2.5c1). The *d*-spacing of graphene layers is calculated to be approximately 0.37 nm (Figure 2.5c2), and the calculated *d*-spacing is slightly larger than that calculated by the XRD results (d-spacing calculated from $2\theta=26.6°$: 0.34 nm). This difference may be due to the TEM, as a localized technique, representing a small portion of graphene disrupted with testing environments such as observation angle and measurement setup. XRD is the standard method for lattice measurements, which represents the whole property. EDS elemental mapping of the cross-section of D-SiO@G displays the distribution of silicon (Figure 2.5f), oxygen (Figure 2.5g), carbon (Figure 2.5h), and their overlays (Figure 2.5e). Evenly distributed silicon and oxygen mappings indicate that the domain size of individual Si clusters is much smaller than the resolution limit of EDS, around 1 μm, and therefore can hardly be detected from the SiO_2 matrix.

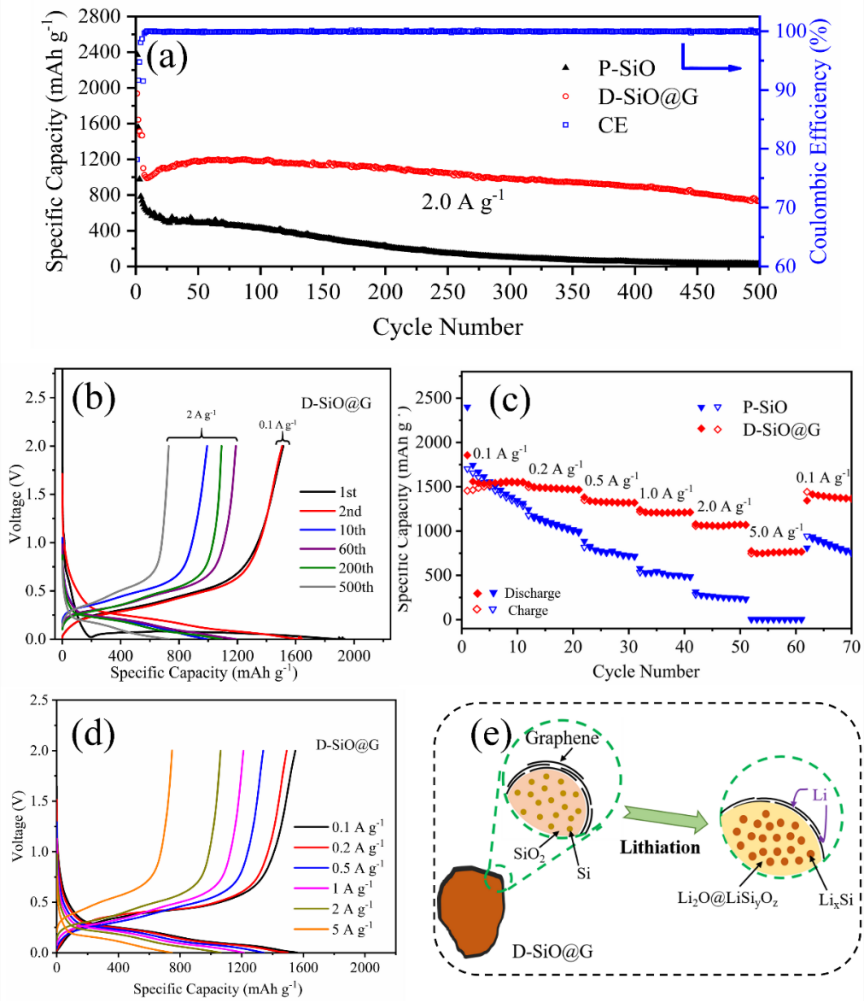

Figure 2. 6. (a) Cycling performance and coulombic efficiency of D-SiO@G and cycling performance of P-SiO at 1 A g^{-1}. (b) Charge-discharge profiles of the D-SiO@G electrode at different cycles. (c) Rate capabilities of P-SiO and D-SiO@G. (d) Charge-discharge profiles of D-SiO@G at different current densities. (e) Illustration of D-SiO@G in lithiation showing the graphene layers can buffer the expansion of SiO.

The well-coated graphene shell on the D-SiO anode creates a remarkable improvement in the electrochemical performance compared to P-SiO (Figure 2.6). As shown in Figure 2.6a, the P-SiO electrode shows a low initial coulombic efficiency (ICE) of 66.3% and poor cycling performance, with a high initial discharge capacity of 2374 mAh g^{-1} at 0.1A g^{-1}. The D-SiO@G electrode exhibits a much higher ICE of 78.2%, one of the highest results among previous reports, and approaches the hypothetical limit of a SiO-based anode with

an excellent cycling performance of 72.4% capacity retention at 500th cycles.[40, 78] A relatively lower initial discharge capacity of 1937.6 mAh g^{-1} at 0.1 A g^{-1} is ascribed to carbon coating counted as the active material, and the disproportionation of SiO, where the partial SiO_2 phase formed by the disproportionation is not lithiation-active.[92] ICE is a critical parameter for anode materials in practical application as the majority capacity loss occurs in the initial cycle due to the formation of the SEI and irreversible reactions. The high ICE of the D-SiO@G electrode should be attributed to the complete graphene coating, which effectively prevents the SEI from growing. The coulombic efficiency of the D-SiO@G electrode increases rapidly, exceeds 99.8% within ten cycles, and stays above 99.8% in most of the following cycles, indicating that the thin and tough graphene shell successfully prevents active particles from fracturing during cycling. This process limits irreversible reactions between the SiO_x and the electrolyte. Figure 2.6b presents the charge-discharge profiles of the D-SiO@G electrode at different cycles. As current density increases to 2.0 A g^{-1}, there is an apparent capacity increase from the 10th to 60th cycle which reaches 1191.8 mAh g^{-1}, likely due to electrolyte penetration in the incipient tens of cycles. Compared to the electrochemical performance of other recent research on SiO_x-based anodes, the D-SiO@G anode in this work displays both high specific capacity and longer life cycles at a higher current density.

Rate capability tests were also conducted and analyzed (Figure 2.6c). As the current density increases from 0.1 A g^{-1}, the specific capacity of D-SiO@G electrodes decreases gradually but still exhibits a discharge capacity of 774.0 mAh g^{-1} at a high current of 5.0 A g^{-1}. As a comparison, the specific capacity of P-SiO decays quickly with an increase of current and delivers a discharge capacity of only 4.7 mAh g^{-1} at 5.0 A g^{-1}. When the value of the current

density returned to 0.1 A g^{-1}, the capacity of the D-SiO@G electrode was restored to nearly the original value, exhibiting excellent rate performance. The charge-discharge profiles for the different current densities (Figure 2.6d) display a similar shape without an apparent voltage plateau change, manifesting the composite's high electrochemical stability over heavy current cycling. The excellent cycling and rate performance can be significantly attributed to the outer graphene shell (Figure 2.6e), which significantly improves the anode's electric conductivity and acts as a significant barrier that prevents side-reactions between D-SiO particles and the electrolyte during cycling.[70]

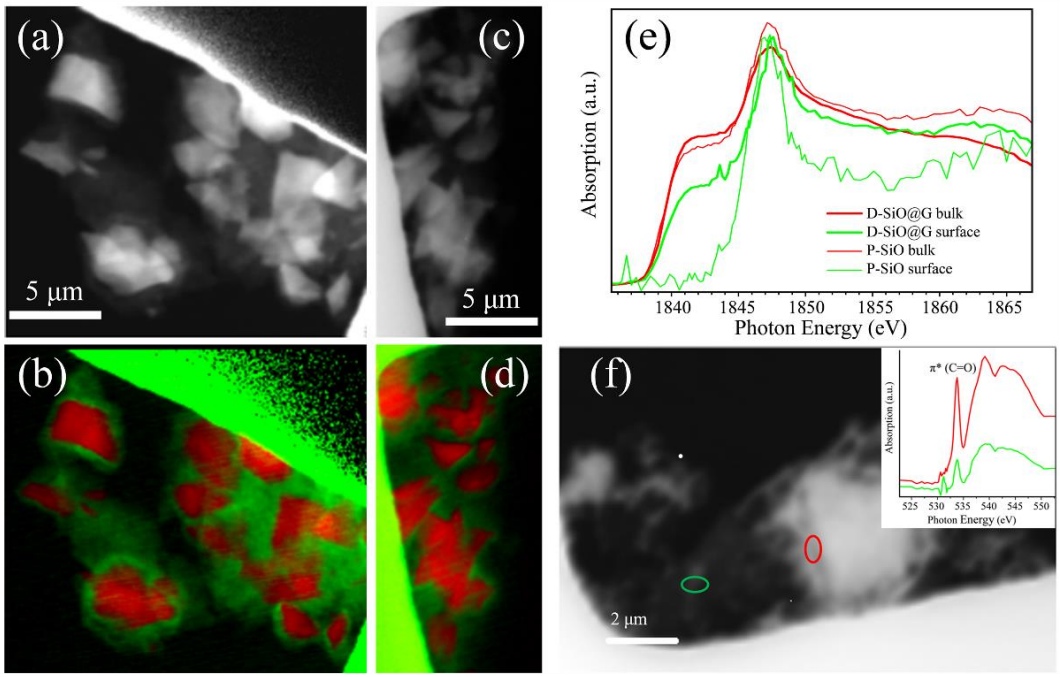

Figure 2. 7. Morphology of (a) P-SiO particles and (c) D-SiO@G particles after cycling 50 times by averaging STXM image stack at Si K-edge, and their chemical mapping at (b) and (d), respectively. (e) Si K-edge XANES spectra of P-SiO bulk (thin red line), and P-SiO surface (thin green line), D-SiO@G bulk (thick red line), D-SiO@G surface (thick green line). (f) Morphology of cycled D-SiO@G particles by averaging O K-edge STXM image stack and the O K-edge XANES spectra (in-site) corresponding to the selected regions in the morphology mapping.

Synchrotron-based scanning transmission X-ray microscopy (STXM) is a powerful tool for imaging and analyzing the chemical composition and structure of various nanomaterials.[88] In this paper, STXM and X-ray absorption near edge structure (XANES) spectra were conducted to explore the morphology and chemical composition of P-SiO and D-SiO@G particles that had been charged and discharged at 1 A g^{-1} for 50 cycles. Figure 2.7a (P-SiO) and Figure 2.7c (D-SiO@G) show the Si atom-sensitive morphology of the cycled particles by averaging STXM image stacks at the Si K-edge. The brightness in these graphs is proportional to the X-ray absorbed by the Si atoms, thereby reflecting the Si concentration. Both samples present large Si-contained particles and morphology resembling that seen in the SEM images, illustrated in Figure 2.2d. Both samples also show morphology features with much lower X-ray absorption in addition to the large bright particles diffused away from large particles. This behavior may be due to SEI in the cycled particles that have fallen off during STXM sample preparation. The chemistry difference between the large particles and the possible missing SEI can be distinguished by extracted Si K-edge XANES spectra, depicted in Figure 2.7e. Chemical mapping of the distribution of bulk anode particle and SEI components in D-SiO@G and P-SiO was conducted by fitting the STXM stack with Si K-edge XANES, the results of which are displayed in Figures 2.7b and 7d, respectively. The mapping confirms the spatial separation between these two components in both samples. Compared with the D-SiO@G (Figure 2.7d), the P-SiO (Figure 2.7b) has more non-anode particle Si-containing species, which infers a higher non-stable SEI film. These results indicate that the graphene shell boosted the growth of the stable SEI film during cycling. Figure 2.7e depicts the Si K-edge XANES spectra of the bulk P-SiO and D-SiO@G (red in Figures 2.7b and 7d) and the SEI in P-

SiO and D-SiO@G (green in Figures 2.7b and 7d). The XANES adsorption feature at approximately 1840 eV is attributed to a silicon phase, and the feature at 1847 eV is oxidized Si, such as SiO_2 and Li_2SiO_3. The Silicon (Si^0) concentration decreases following the trend of bulk D-SiO@G >bulk P-SiO > SEI in D-SiO@G > SEI in P-SiO, while at the same time the oxidized silicon shows an opposite change trend. Since STXM is a transmission technique and, therefore, a bulk sensitive probe, the observed enhanced silicon feature in bulk P-SiO and SEI in D-SiO@G, relative to that in P-SiO, verifies a thinner and more stable SEI in D-SiO@G.[87] This point is further validated by the detection of Li_2CO_3, a stable SEI in carbon-based anodes via O K-edge XANES spectra and STXM images of the cycled D-SiO@G particles in Figure 2.7f. The inset XANES spectra of the specified STXM spots exhibit the π* (C=O) bond's spectroscopic feature via the peak at 533 eV and the peak splitting at ~ 540 and 545 eV in the D-SiO@G particle indicating the existence of Li_2CO_3.[96] Li_2CO_3 must be formed by the reaction between the graphene shell and electrolyte during battery cycling and is considered an active phase to prevent solvent co-intercalation and carbon exfoliation.[97]

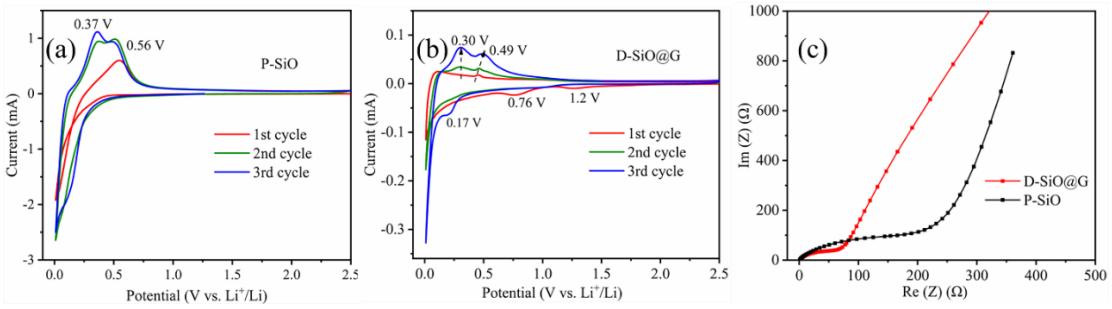

Figure 2. 8. (a) Cyclic Voltammetry curves of P-SiO and (b) D-SiO@G at a scanning rate of 0.1 $mV \cdot S^{-1}$ for the first 3 cycles. (c) The Nyquist plots of P-SiO and D-SiO@G based electrodes before cycling.

The CV profiles in Figure 2.8(a-b) delineate the first three cycles of the prepared P-SiO and D-SiO@G at the scanning rate of 0.1 $mV \cdot S^{-1}$. The broad cathodic peaks at both 1.2V and 0.76V for D-SiO@G in the first reduction process can be assigned to the formation of a solid electrolyte interphase (SEI) film.[98] The cathodic peak at 0.01 – 0.2 V for both P-SiO and D-SiO@G corresponds to the reaction of Li-ions and SiO, forming Li_xSi, Li_2O, and lithium silicates.[56] In the following oxidation process, the anodic peaks at 0.37 V and 0.56 V for P-SiO, 0.30 V and 0.49 V for D-SiO@G can be ascribed to the lithium's removal from the Li_xSi phase.[99] The values of the D-SiO@G redox peak increase in subsequent cycles as more silicon participates in the lithiation/delithiation process.[100] The difference between each redox peak potential (ΔE_p) for D-SiO@G (0.01V and 0.30V) is smaller than that of the P-SiO anode (0.01V and 0.37V), which is due to the coated graphene shell that assists in the transfer of Li-ions and electrons and stabilizes the SEI film.[63-64] This explanation is also supported by the electrochemical impedance spectroscopy (EIS) analysis (Figure 2.8c). Nyquist plots for both instances exhibited depressed semicircles at high and medium frequencies corresponding to charge transfer resistance (R_{ct}), along with an oblique line at a low frequency associated with Li-ion diffusion. Compared to the P-SiO electrode (R_{ct} = 149.3 Ω), the D-SiO@G electrode (R_{ct} = 52.6 Ω) presents a much smaller charge-transfer resistance, demonstrating that the graphene shell can significantly improve interface properties and electronic conductivity.[65]

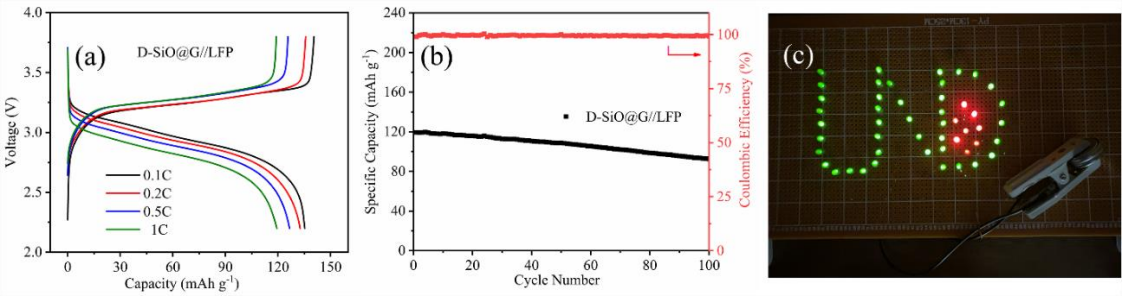

Figure 2. 9. (a) Discharge and charge profiles of the D-SiO@G//LFP full cell at different rates. (b) The cycling performance of the D-SiO@G//LFP full cell. (c) LED matrix successfully lit by the D-SiO@G//LFP full cells.

Several full cells in coin cell configuration were created by pairing the D-SiO@G electrodes with the LFP electrodes to demonstrate the feasibility of practical application in LIBs. The D-SiO@G electrodes were prelithiated to improve the coulombic efficiency in the first cycle. The assembled D-SiO@G//LFP full coin cell demonstrates an excellent rate capability with the increase of a charge-discharge rate from 0.1 C to 1 C (1 C=170 mA g^{-1}). The discharge capacities have a slight decay, from 135.3 mAh g^{-1} to 119.3 mAh g^{-1} (Figure 2.9a). This decay should be attributed to the capacity loss of the LFP cathode from 0.1C to 1C. Further cycling tests within the cell potential range of 2.0 – 3.8 V at 1 C (Figure 2.9b) indicate that the full cell can retain a considerable capacity of 75% after 100 cycles. Two of the assembled full cells were successfully connected to an LED matrix, which reacted with an intensely bright light (Figure 2.9c), suggesting an excellent full cell performance based on the D-SiO@G anode and LFP cathode.

2.4. Conclusion

In summary, a simple approach to in-situ synthesizing high-performance silicon and graphene anode materials for LIBs has been developed using coal-derived HA as a carbon source. We have confirmed the simultaneous conversion of HA to graphene and the disproportionation reaction of SiO with various characterization tools. The well-coated

graphene shell hinders the reaction between the electrolyte and the SiO particles while significantly improving the SiO anode's conductivity. As a result, The D-SiO@G anode presents excellent cycling performance and rate capabilities, exhibiting high reversible specific capacities of 1023 mAh g^{-1} and 774 mAh g^{-1} at a current density of 2 A g^{-1} and 5 A g^{-1}, respectively, along with an initial coulombic efficiency (ICE) of 78.2%. We also performed tests indicating a successful high current capability using D-SiO@C electrodes paired with LFP electrodes to illuminate an LED matrix.

The in-situ graphene coating approach can be easily adapted to an existing industrial procedure for LIB electrode material production. No toxic reagents, expensive catalysts, or harsh conditions were involved in the synthesis process, creating an efficient scaling method. Our work's adaptability and scalability are substantially different from most graphene coating reports for LIBs;[55, 64, 67, 70, 93] therefore, this simple process combined with the abundant and low-cost raw materials indicates a significant potential for successful commercialization. This work not only advances the current technology of preparing high-performance silicon and graphene anode materials, it also provides an excellent method of developing "coal-to-high value product" technology under a carbon-strain environment.

CHAPTER III

INVERSTIGATION OF THE EFFECTS OF HEAT TREATMENT AND CARBON COATING ON THE ELECTROCHEMICAL BEHAVIORS OF SILICON MONOXIDE ANODE

Statement: This chapter is based in part on the previously published article listed below:

Xu, S.; Hou, X.; Wang, D.; Zuin, L.; Zhou, J.; Hou, Y.; Mann, M., Insights into the Effect of Heat Treatment and Carbon Coating on the Electrochemical Behaviors of SiO Anodes for Li-Ion Batteries. *Adv Energy Mater.* **2022**, 2200127.

3.1. Introduction

SiO's high capacity with relatively stable cycling performance attracts intensive interest in its application in LIBs. Some approaches have been conceived to improve the electrochemical performance of SiO anode, including conductive coating,[11] structural design,[12] and chemical etching,[13] which are effective. These approaches usually involve a common heat treatment process to calcinate the SiO-related precursors; however, most of these reports did not consider the heat treatment's impact on SiO since it is thermally unstable due to its unique structure. Heat treatment can expedite the disproportionation reaction of SiO:[14]

$$2SiO \rightarrow Si + SiO_2$$

The disproportionation reaction accelerates at temperatures higher than 800 ℃, promoting the Si and SiO_2 phase separation.[15] Higher temperatures and longer heating times increase

the degree of disproportionation, which can be indicated by the increased nanocluster size and crystallinity of the Si phase.[14]

Intensive SiO studies have demonstrated that the growth and separation of the Si and SiO_2 phase caused by heat treatment can significantly impact its electrochemical performance.[5a, 15a] The electric resistance of the disproportionated SiO materials increases when heated at high temperatures since the SiO_2 matrix phase becomes denser and more dielectric.[16] The disproportionated SiO (D-SiO) becomes inert during lithiation because of the high electrical resistance caused by the SiO_2 matrix when heated at temperatures higher than 1,150 °C;[15a] however, there are still some unsolved questions about the effect of heat treatments on SiO. *1)* How do heat treatments impact the electrochemical performance of SiO anodes? Several researchers have investigated ICE and cycling life, but their results are often contradictory.[17] *2)* How does the surface composition and structure of the SiO anode particle change during heat treatment? Reports studying the disproportionation of SiO have focused on its bulk properties, overlooking the composition and structure change on its surface, which plays a crucial role in the electrochemical behaviors of SiO materials, including SEI formation, initial lithiation, and charge transfer resistance. The overpotential that appeared in the initial lithiation of disproportionated SiO materials has not been thoroughly investigated yet.[15a, 17a] *3)* What is the cause of "Si nanowire" formations often observed during SiO heat treatment?[18] "Si nanowires" formed on the surface of SiO particles when heated from 900-1100 °C. These nanowires were deemed conducive to the electrochemical performance of a SiO-based anode; however, the report failed to provide a detailed analysis of its formation mechanism, synthetic atmosphere, distribution, and

content.[19] *4)* How does carbon coating impact the composition and nanostructure evolution of SiO materials during heat treatment?

To shed a light on those fundamental questions, herein we present a systematic study on this matter. We start with investigating the effects of heat treatment and carbon coating processes on the morphology, microstructure, and chemical composition of SiO by using a series of microanalysis techniques, such as SEM, Raman, and XRD. Our work focused on analyzing the dynamic evolution of the Si and SiO_2 phases during the process. We further analyzed and compared three anode particles, namely pristine SiO (P-SiO), D-SiO, and carbon-coated D-SiO (D-SiO@G), before and after cycling by XANES technique (Li-K and Si L-edge), supplemented with battery cycling life and Electrochemical Impedance Spectroscopy (EIS) testing. At last, we proposed a SiO structural model to illustrate the relationships of "synthetic processes-microstructure-electrochemical behaviors".

3.2. Methods

3.2.1. D-SiO Preparation: Disproportionated SiO (D-SiO) powder was prepared by sintering pristine SiO (P-SiO, D_{50} = 5 μm, the atomic ratio of Si and O = 1:1, Alibaba) using a series of heat treatment processes (300 ℃ for 2 h, and then at 800 ℃ for 2 h, 900 ℃ for 2 h, 1,000 ℃ for 2 h, 1,000 ℃ for 8 h, and 1 000 ℃ for 20 h) with a ramp rate of 5 ℃ min^{-1} under a reducing atmosphere (10% H_2 with 90% Ar) in a TFM2 two-zone tube furnace (Across International, USA). The obtained D-SiO samples were named D-SiO-800-2, D-SiO-900-2, D-SiO-1000-2, D-SiO-1000-8, and D-SiO-1000-20. Another series of disproportionated SiO (D-SiO) powder was prepared using the same heat treatment process except under a pure Ar atmosphere.

3.2.2. D-SiO@G Preparation: Humic acid, extracted and purified from North Dakota lignite according to our previous reports, was used as the carbon source in the carbon coating process.[101] Humic acid (2.5 g) and 10 g of P-SiO powder were mixed in 100 mL of DI water, then 1 mL of ammonium (28% - 30%, LabChem USA) was added dropwise into the mixture to dissolve the humic acid completely. This slurry was stirred vigorously for 1 hour then spray dried (Spray Dryer TP-S15, Toption) with an inlet temperature of 200 ℃. The powder was then sintered using the same heat treatment process as the D-SiO preparation. A series of D-SiO with graphene coating composites (D-SiO@G) were obtained upon cooling to room temperature. The obtained D-SiO@G composites were named D-SiO@G-800-2, D-SiO@G-900-2, D-SiO@G-1000-2, D-SiO@G-1000-8, and D-SiO@G-1000-20.

3.2.3. Materials Characterization: Powder X-ray diffraction (XRD) profiles were collected using an X-ray diffractometer (Smartlab, Rigaku) at an accelerating voltage of 40 kV, a tube current of 44 mA, and a scan rate of 2° min^{-1} from 10° to 80°. Field-emission transmission electron microscopy (FE-TEM, JEM-2100F, JEOL, 200 kV) and field-emission scanning electron microscopy (FE-SEM, Quanta 650 FEG, FEI) were conducted to analyze particle morphology and microstructure. X-ray photoelectron spectroscopy was conducted using a PHI 5600ci spectrometer equipped with a hemispherical electron analyzer and a monochromatic Al Kα (1486.6 eV) radiation source. A carbon analyzer (TOC-V, SHIMADZU) with an SSM 5000A module was used to calculate the carbon content of the D-SiO@G composites.

3.2.4. Electrochemical Measurements: Active materials, conductive agent (acetylene black), CMC (Carboxymethyl Cellulose), and SBR (Styrene-Butadiene Rubber) with a

mass ratio of 60:20:8:12 were mixed with DI water for 8 h to prepare the electrode paste. The paste was spread onto a copper foil and dried overnight in a vacuum at 100 ℃. The coated copper foil was punched into disks with a diameter of 14 mm to create working electrodes, in company with lithium foil as the counter electrodes, 1.2 M $LiPF_6$ in EC/DMC/EMC (1/1/1 in wt%) with 10 wt% FEC as the electrolyte, and Celgard 2400 membrane as the separator to assemble CR2032 coin cells. Galvanostatic charge-discharge testing between 0.001 V and 2.0 V (vs. Li/Li^+) was performed with a battery testing system (CT-4008, Neware Technology Limited, Shenzhen, China) at room temperature. In this work, the discharge process represented the lithiation process while the charge was delithiation. Cyclic voltammetry (CV) and electrochemical impedance spectroscopy (EIS) were conducted on a potentiostat (Interface 1010E, Gamry Instruments, USA).

P-SiO, D-SiO-1000-8, and D-SiO@G-1000-8 electrodes with an initial status of lithiation (SoL) were investigated with Si L-edge and Li K-edge X-ray Absorption Near-Edge Structure spectroscopy (XANES) at the VLS-PGM beamline of the Canadian Light Source, University of Saskatchewan. Electrodes in half coin cells were first lithiated to a specific state of lithiation (SoL) then disassembled and rinsed with acetonitrile (>99.5%, Fisher Chemical) in a glovebox. The electrodes were dried in an ultra-pure Ar atmosphere, attached to the sample holders under an Ar atmosphere, then transferred into the vacuum chamber of the beamline's endstation. The XANES spectra were collected and analyzed using a microchannel plate detector in the fluorescent yield mode (FLY).[102] A high vacuum ($< 1 \times 10^{-7}$ torr) was maintained in the experimental chamber during the test. The collected FLY data were normalized with the I_0 current and measured using a nickel mesh

placed in front of the sample. The energy shift of the beamline was calibrated by the LiCl during the test. Please refer to the reference for detailed operation procedures.[103]

3.3. Results and Discussion

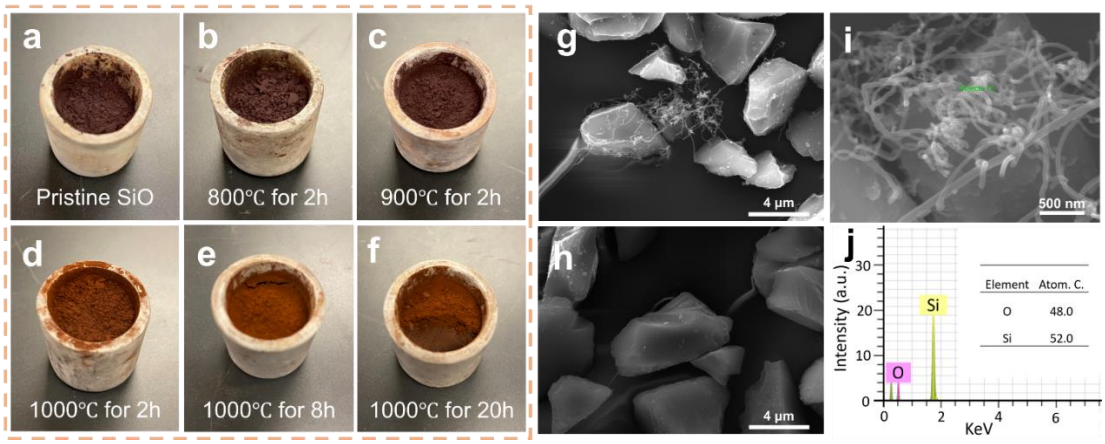

Figure 3. 1. (a-f) Photos of crucibles with SiO powder after heat treatments. SEM images of (g) the D-SiO particles in the top red-brown substance (TRS), and (h) D-SiO particles under the TRS. (i) EDX analysis spot of the Si nanowires, and (j) corresponding elemental content.

Figure 3.1a-f depicts the photos of the pristine SiO (P-SiO) and D-SiO samples after heat treatments under a reducing atmosphere. The pristine P-SiO powder (Figure 3.1a) is brownish-black, similar to the appearance of the D-SiO samples prepared at lower temperatures (Figures 3.1b and c). The D-SiO powder in the crucibles is covered with a thin topping of a reddish-brown substance (TRS) when heated at 1 000 ℃ for 2 h and above in the reducing atmosphere (Figure 3.1d-1f), as indicated by the cross-section of the D-SiO-1000-20 powder (Figure 3.1f). The TRS accounts for about 1/25 (1000 ℃ for 2h) to 1/9 (1000 ℃ for 20h) in weight of the D-SiO powder. After the topping was removed, all the following characterizations were focused on the bottom part. SEM inspection reveals that some nanowires (Figure 3.1g) are attached to D-SiO particles in the TRS layer, while the bulk of the D-SiO powder under the TRS is composed of D-SiO particles (Figure 3.1h)

that are identical to the P-SiO particles (Figure 3.2m) with no interparticle nanowires. The EDX elemental analysis (Figure 3.1j) reveals that the nanowires consist of silicon and oxygen with atomic contents of 48.0 and 52.0%, respectively. The atomic ratio of silicon to oxygen (~ 1:1) indicates that the so-called "Si nanowires" are primarily SiO, formed by the sublimation of SiO and the subsequent deposition of SiO vapor under high temperatures. These Si nanowires should have a crystalline silicon core and an amorphous SiO_2 sheath structure, as indicated by previous reports.[104-105] The electrochemical improvements, if any, by the Si nanowires would be restricted to their insulating structure (dielectric SiO_2 sheath), small quantity, and localized distribution. It is worth noting that under ultra-pure argon, which is one of the most widely-used atmospheres in research, a topping of white (instead of reddish-brown) nanowires in the TRS layer was observed. The white nanowires are composed of SiO_2 (Figure 3.2a-f). Therefore we suspect SiO is oxidized by the trace oxygen in the high purity argon, which indicates the SiO is extremely reactive at a high temperature. The color of the D-SiO powder (Figure 3.2g-l) becomes lighter with an increase in heating temperature and time, from brownish-black similar to the P-SiO to brown when heated at 1000 ℃ for 20 h. This observation implies that a layer of the lighter color substance is likely enriched on the SiO particle surface. During the high-temperature treatment, the SiO vapor consisting of $(SiO)_n$ ($n \geq 1$) clusters would also deposit onto its surrounding D-SiO surfaces in addition to the formation of Si nanowires. Higher binding energy and lower surface strain are the driving forces of a stable configuration as calculated by the density-functional theory, which makes it energetically favorable for oxygen atoms to migrate from the core to the surface, causing the structural

transition:[59, 106] An exterior SiO_2 shell forms on the surface of D-SiO particles, while the Si phase remains in the core, making the color of D-SiO powder lighter.

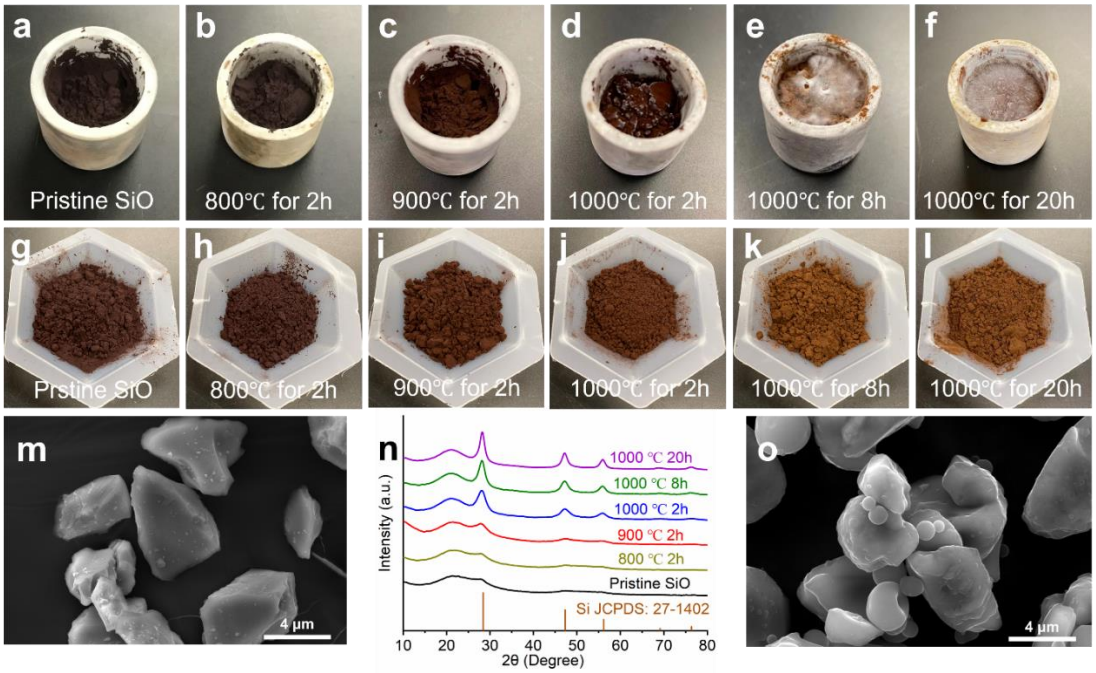

Figure 3. 2. (a-f) Photos of SiO powder in crucibles after heat treatments in ultra-pure Ar atmosphere. (g-l) Photos of the SiO powder after heat treatments (toppings removed). (m) SEM image of the pristine SiO (P-SiO). (n) XRD patterns of the P-SiO and D-SiO samples. (o) SEM image of the D-SiO@G particles.

Another consequence of the heat treatment process is the evolution of the XRD patterns (Figure 3.2n). P-SiO exhibits an XRD pattern with a bump peak (15-30°). D-SiO-800-2 shows a similar XRD pattern as P-SiO, indicating that no apparent disproportionation reaction happens when heated at 800 ℃ for 2 h. Several peaks belonging to crystalline Si appear, and become sharper and more intense as the temperature and heating time increase, while a broad peak (18 – 25°) attributed to amorphous SiO_2 is also separated from the SiO bump peak.[107]

The effect of the carbon coating on the SiO morphology evolution during the heat treatment process was also investigated. We used humic acid as the carbon source to create a conductive and resilient nano-graphene coating during the heat treatment process.[101] The synthesized D-SiO@G composites (Figure 3.2o) possess a similar particle size to P-SiO but with a rounded-edge shape because of the graphene coating. Importantly, no Si nanowire is found in the powder. The coating accounts for 9.1 wt% of the D-SiO@G and does not change the XRD patterns compared to the D-SiO materials.

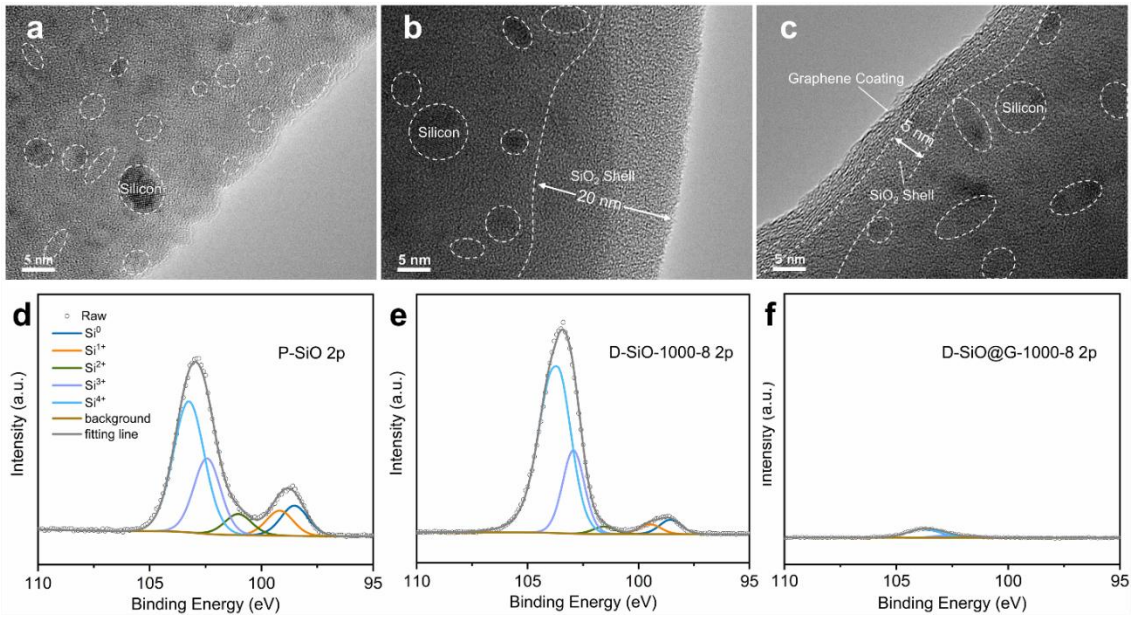

Figure 3. 3. TEM images of (a) P-SiO, (b) D-SiO-1000-8, and (c) D-SiO@G-1000-8. XPS spectra and their corresponding fitting peaks for (d) P-SiO, (e) D-SiO-1000-8, and (f) D-SiO@G-1000-8.

High-resolution transmission electron microscopy (HRTEM) was performed to inspect the SiO's surface composition and microstructure changes during the heat treatment and graphene coating process. The observable lattice fringes belonging to Si nanoclusters are enclosed by the amorphous matrix, represented by white dashed circles in Figures 3.3a, 3b, and 3c. The HRTEM image of P-SiO (Figure 3.3a) indicates a swarm of Si nanoclusters a

few nanometers in size randomly distributed in the amorphous SiO_2 matrix in the radial direction of the particle.[46] The HRTEM image of a D-SiO-1000-8 particle (Figure 3.3b) indicates that no Si nanoclusters can be found near the particle surface except for a thick amorphous SiO_2 shell (~ 20 nm) because of the heat treatment. The Si nanoclusters are fewer but larger in size compared with P-SiO.[108-109] The HRTEM image of a D-SiO@G-1000-8 particle (Figure 3.3c) reveals the Si nanoclusters similar in size to D-SiO-1000-8, however, possess a much thinner amorphous SiO_2 shell (5 nm). The surface difference can be attributed to the intact graphene coating, which limits the sublimation and subsequent deposition of SiO and hinders oxygen migration from the core to the surface effectively, resulting in a thinner SiO_2 shell and the absence of Si nanowires in all carbon-coated samples. The TEM observations are also supported by X-ray photoelectron spectroscopy (XPS) results. The Si 2p peaks in all P-SiO spectra (Figure 3.3d), D-SiO-1000-8 (Figure 3.3e), and D-SiO@G-1000-8 (Figure 3.3f) can be fitted with five subpeaks corresponding to Si^0 (Si nanocluster), Si^{1+}, Si^{2+}, Si^{3+}, and Si^{4+} (SiO_2 matrix). The considerable Si and SiO_2 subpeaks in the P-SiO spectrum indicate prevalent Si nanoclusters and SiO_2 phases on the P-SiO particle surface, which agree well with the TEM results. Intermediate valence (Si^{1+}, Si^{2+}, Si^{3+}) subpeaks experience considerable shrinkage from P-SiO to D-SiO-1000-8 due to the heat treatment process, since these valences disproportionate into Si^0 and Si^{4+}, forming larger Si nanoclusters and denser SiO_2 matrices; however, the Si^0 subpeak in D-SiO-1000-8 does not increase accordingly with the Si^{4+} peak but suffers significant reduction, which should be attributed to the cover of the exterior SiO_2 shell since the XPS only has a detective depth of a few nanometers for solid materials. The intact graphene coating of the D-SiO@G-1000-8 composite (Figure 3.3f) leads to a very weak Si 2p peak,

in which the Si^{4+} subpeak dominates, demonstrating the existence of the SiO_2 shell beneath the graphene coating.

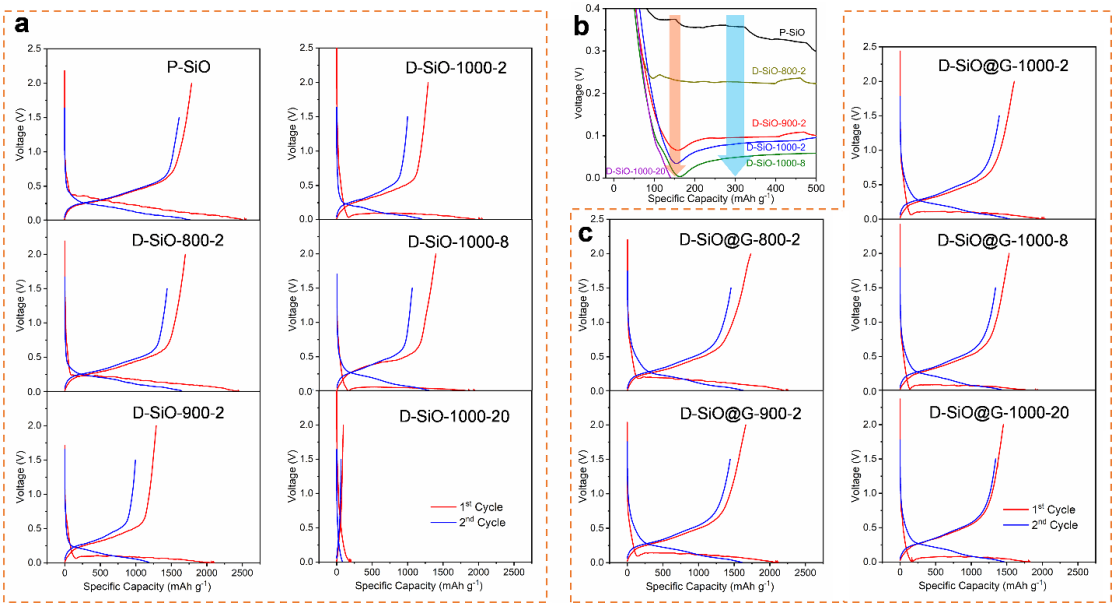

Figure 3. 4. (a) First and second charge-discharge SiO curves after different heat treatments, and (b) the overpotential of SiO samples. (c) First and second charge-discharge curves for D-SiO@G samples.

We used half coin-cell testing to further investigate the effect of the heat treatment and carbon coating process on the SiO electrochemical behavior. Figure 3.4a illustrates the charge-discharge profiles of the first and second cycles of the P-SiO and D-SiO electrodes. P-SiO delivers the highest discharge capacity of 2564.8 mAh g^{-1} (Table 1) at a current density of 50 mA g^{-1}. D-SiO-800-2 delivers a capacity (2461.2 mAh g^{-1}) close to P-SiO since the heat treatment at 800°C for 2 h cannot make substantial changes to P-SiO. The initial discharge capacity decreases with an increase in temperature and heating time, accompanied by a decline in the discharge plateau potential, indicating that the overpotential of the electrodes increases drastically.[78] Figure 3.4b specifically depicts the overpotential evolution of all SiO samples. As lithiation begins, the max-overpotential

point appears at the incipient stage of lithiation, at approximately 150 mAh g^{-1}. Higher heating temperatures and longer heating times facilitate the formation of a thicker and denser SiO_2 shell, making it more resistant to electrochemical reactions.[110-111] The shell with high electrical resistance and low Li^+ transport acts as a barrier, preventing the migration of Li-ions through the surface of the particles, causing the maximum resistance overpotential (orange arrow, Figure 3.4b). When the heat treatment is performed at 1000 °C for 20 h, the exterior SiO_2 shell is thick enough to completely prevent Li-ions from passing through, making the lithiation potential drop to 0 V versus the counter electrode (lithium metal), which indicates that Li-ions cannot penetrate through the SiO_2 shell and begin to deposit on the surface of the D-SiO particles, resulting in the capacity dive of D-SiO-1000-20. Li-ions can pass through the barrier and react with Si nanoclusters inside the D-SiO particles with lower heating temperatures or less heating times, releasing more capacity (> 150 mAh g^{-1}, Figure 3.4b). The following lithiation process is also accompanied by the drop of the discharge plateau potential (blue arrow, Figure 3.4b), from 0.35 V for P-SiO to 0.07 V for D-SiO-1000-8 at the capacity of ~300 mAh g^{-1}, indicating that the amorphous interior SiO_2 matrix also becomes denser and more inert at high temperatures, causing a new resistance overpotential. Another valuable finding was that once Li-ions react with the SiO_2 shells and SiO_2 matrix, they form irreversible Li_2O and Li silicates, which are conducive to charge transfer and act as the access point for Li^+ transport in the following cycles.[47] As a result, no resistance overpotential was observed after the first cycle of all samples (Figures 3.4a and 4c).

Table 3. 1. Initial Discharge Capacity and ICE for pristine SiO, D-SiO, and D-SiO@G samples.

SiO samples	Initial Cycle			D-SiO@G samples	Initial Cycle		
	Discharge (mAh g^{-1})	Charge (mAh g^{-1})	Efficiency (%)		Discharge (mAh g^{-1})	Charge (mAh g^{-1})	Efficiency (%)
P-SiO	2564.8	1709.3	69.8				
D-SiO-800-2	2461.2	1697.4	69.0	D-SiO@G-800-2	2264.4	1733.1	76.5
D-SiO-900-2	2107.9	1287.9	61.1	D-SiO@G-900-2	2124.2	1662.6	78.3
D-SiO-1000-2	1992.1	1204.2	60.4	D-SiO@G-1000-2	2044.0	1604.0	78.5
D-SiO-1000-8	1968.9	1395.0	70.9	D-SiO@G-1000-8	1942.8	1533.4	78.9
D-SiO-1000-20	207.9	93.9	45.2	D-SiO@G-1000-20	1831.1	1452.8	79.3

Figure 3.4c depicts the effect of graphene coating on the charge-discharge behaviors of the D-SiO samples. D-SiO@G samples treated at higher temperatures and longer times also present a decrease in initial discharge capacity, which is similar to the P-SiO and D-SiO samples; however, the sample D-SiO@G-1000-20 could overcome the overpotential barrier and deliver a considerable discharge capacity (1831.1 mAh g^{-1}), while its uncoated counterpart D-SiO-1000-20 could not. This difference should be attributed to the graphene coating that favors thinner SiO_2 shells and makes the D-SiO particles more conductive, which alleviates the overpotential and facilitates charge transfer.[55, 112] The graphene coating can significantly increase the ICE, as depicted in Table 1: D-SiO-800-2 has an ICE of only 69.0%, while the ICE of D-SiO@G-800-2 significantly increased to 76.5%. With the increase in heating temperature and time, the ICE further increases to 79.3% for D-

SiO@G-1000-20. Two reasons for that are: 1) the graphene coating prevents the side reactions between the electrolyte and SiO materials, limiting the growth of the SEI film and leaving more Li-ions reversible, and 2) a higher temperature and longer heating time make the SiO_2 domains denser and more electrical resistant, limiting the formation of Li silicate, a well-known low Coulombic efficiency byproduct[113].

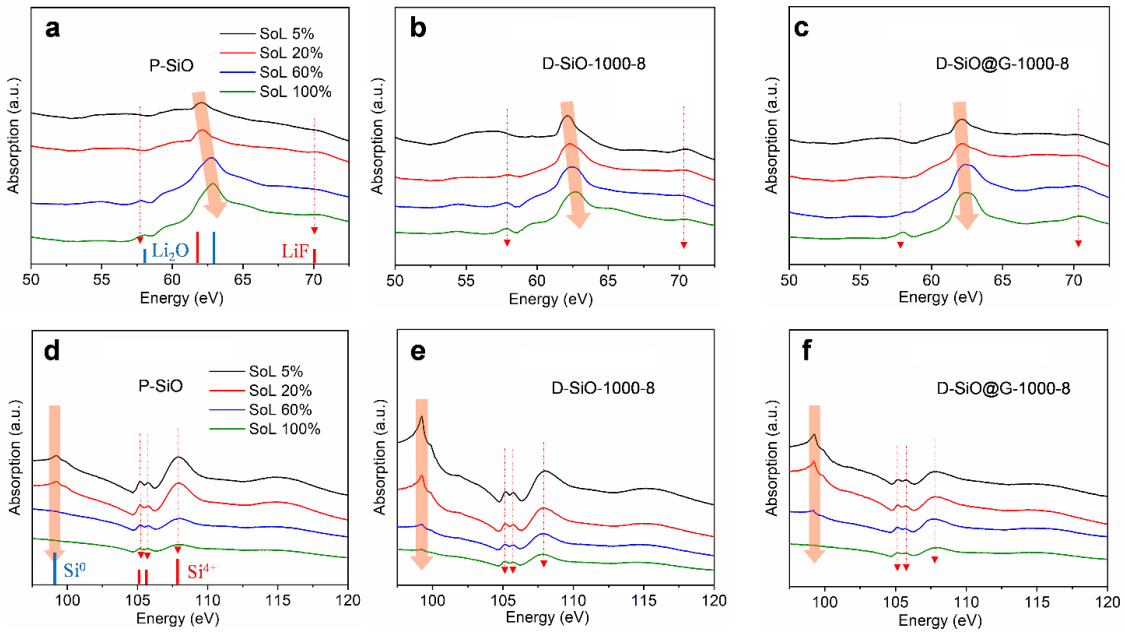

Figure 3. 5. Li K-edge XANES spectra of (a) P-SiO, (b) D-SiO-1000-8, and (c) D-SiO@G-1000-8 electrodes at a series of SoL. Si L-edge XANES spectra of (d) P-SiO, (e) D-SiO-1000-8, and (f) D-SiO@G-1000-8 electrodes at a series of SoL.

X-ray Absorption Near-Edge Structure spectroscopy (XANES) as a powerful tool for analyzing the chemical composition and distribution of electrode interface and bulk was conducted at the VLS-PGM beamline of the Canadian Light Source. Figures 3.5a, 5b, and 5c reveal the Li-K edge XANES spectra of the P-SiO, D-SiO-1000-8, and D-SiO@G-1000-8 electrodes respectively as a function of the state of lithiation (SoL) (5%, 20%, 60%, and 100%) in the first lithiation. In the three graphs, three peaks can be allocated to two compounds, LiF (peaks at ~ 62 eV and ~ 70 eV) and Li_2O (~ 58 eV and ~ 63 eV), as

indicated in the XANES library for lithium compounds.[103] Li_2O originates through two routes: 1) the lithiation reaction of SiO, and 2) the decomposition product of two unstable SEI components, Li_2O_2 and Li_2CO_3, caused by the soft X-ray radiation during the XANES measurement. Route 2 is trivial and neglectable in our testing due to limited X-ray exposure time (<10 min).[53, 103, 114] The low Li-K edge excitation energy (50 eV- 75 eV) leads to an analysis depth of approximately 15 nm, which is ideal for analyzing the chemical composition of the SEI film formed in the initial lithiation process. All three spectra (SoL 5%) in Figures 5a, b, and c had two peaks (~ 62 V and ~ 70 eV) in the initial discharge (lithiation) process corresponding to a lithiation potential of 0.5 V, attributable to LiF: a major characteristic component of SEI film.[53] A new peak at ~58 eV appears with an SoL increase of 5% to 100%, accompanied by the shift of the main peak from ~ 62 eV to ~ 63 eV. The peak shift degree was in the order: P-SiO > D-SiO-1000-8 > D-SiO@G-1000-8, as indicated by the orange arrow (Figure 3.5a-c). With the SoL of 100%, the main peak in P-SiO had the largest shift, indicating the Li_2O overtake LiF on the particle surface, while the D-SiO@G-1000-8 peak has no apparent shift, indicating LiF remains dominant along with Li_2O. In other words, the latter has a more stable surface chemical composition. Since the analysis depth of the Li-K edge is greatly overlapped with the thickness of the SEI film formed in the initial lithiation, it is safe to conclude that the SEI film formed on the D-SiO@G-1000-8 is more stable than the other two counterparts. Combining with the initial lithiation (discharge) capacity data in Table 1, P-SiO (2564.8 mAh g^{-1}) delivered a capacity 30.3% higher than D-SiO-1000-8 (1968.9 mAh g^{-1}). We further infer that the accompanied severe volume change from the high capacity of P-SiO breaks the as-formed SEI, leaving more Li_2O in lithiated SiO exposed and then detected.[87]

Figure 3.5 (d, e, and f) illustrates the Si-L edge XANES spectra of the P-SiO, D-SiO-1000-8, and D-SiO@G-1000-8 electrodes with an initial SoL series of 5%, 20%, 60%, and 100%, respectively. The peaks at 99 eV in each graph are associated with Si^0, also referred to as Si nanoclusters, while those from 104 –109 eV are attributable to Si^{4+}, also referred to as the SiO_2 phase.[115] Specifically speaking, the first two peaks around 105-106 eV can assign to Si3s, while the broad peak at 108 eV is Si3d state.[116] D-SiO-1000-8 exhibits the most intense Si peak due to the disproportionation of SiO, while the Si peak for D-SiO@G-1000-8 is slightly weaker due to carbon coating. It is also visible that D-SiO@G-1000-8 has a lower Si3d state, which might reflect the Si-O-C interaction, and this is the key electronic structure observation by XANES. The detection depth of the Si L-edge XANES spectra can be 150 nm at 99 eV, which is deep enough to gain the bulk information inside particles. With the increase of SoL in the initial lithiation process, Si reacts with Li-ions, forming Li_xSi alloys, while SiO_2 reacts with Li-ions, and mainly forms Li_2O and Li silicates, leading to the declination of all peaks. All three electrodes show a gradual decrease of Si3d intensity along with lithiation which might indicate that charge compensation involves Si3d state. The Si^0 peak of the P-SiO and D-SiO@G-1000-8 electrodes disappear when the SoL reaches 100%, while the D-SiO-1000-8 electrode still has some residual. This observation indicates that some Si nanoclusters are not able to react with Li-ions in D-SiO due to the resistance of the exterior SiO_2 shell and interior SiO_2 matrix, resulting in a capacity loss. As for sample D-SiO@G-1000-8, the graphene coating limits the growth of the SiO_2 shell and makes the particles more conductive than D-SiO-1000-8, leading to a higher lithiation degree. The evolution of the surface and bulk composition revealed by the XAENS analysis agrees well with their electrochemical performance.

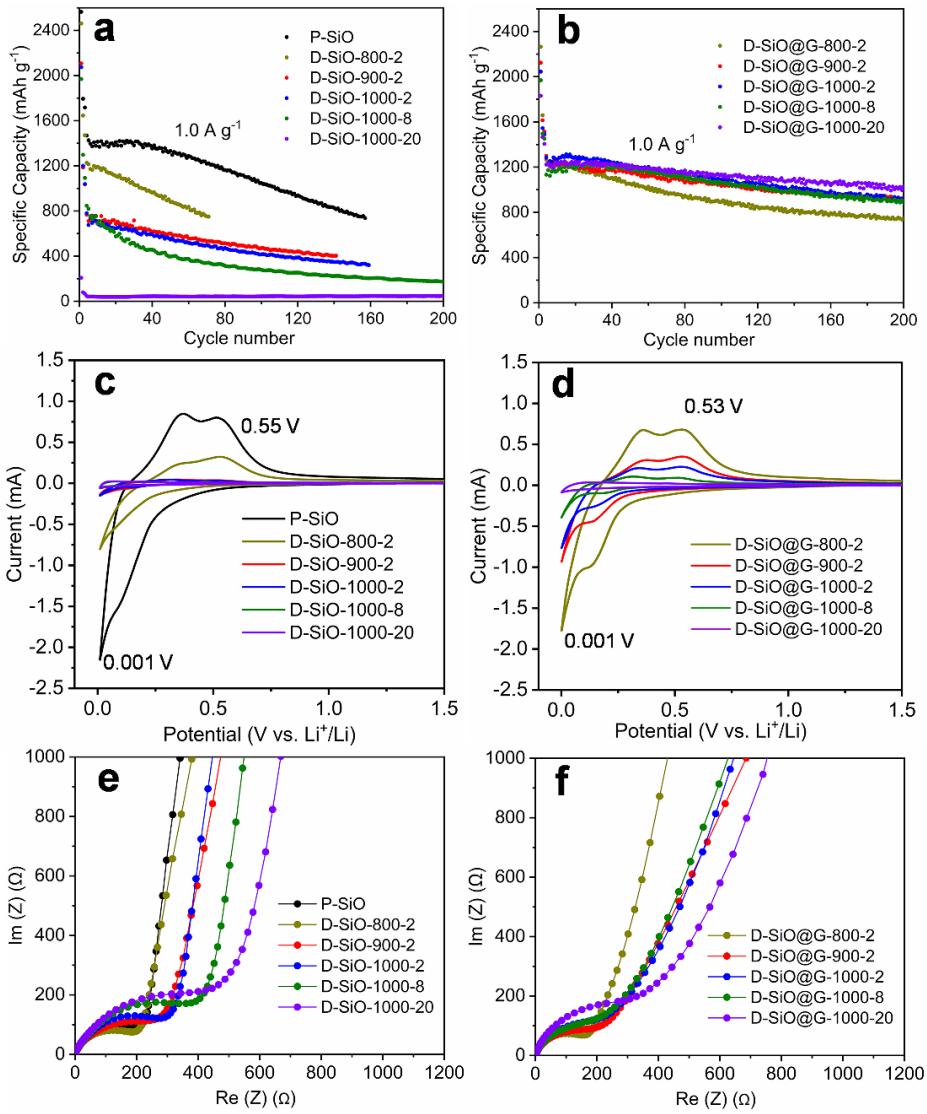

Figure 3. 6. Cycling performance of (a) SiO and (b) D-SiO@G samples (50 mA g^{-1} for the first cycle, 200 mA g^{-1} for the second and third cycles, and 1,000 mA g^{-1} for the rest cycles). Cyclic voltammetry curves (third cycles) for the (c) SiO and (d) D-SiO@G samples. Nyquist plots of the (e) SiO and (f) D-SiO@G samples.

The effect of heat treatment and carbon coating on electrochemical performance is further illustrated in Figure 3.6. P-SiO has the best cycling performance among SiO samples, delivering a reversible capacity of 1468.2 mAh g^{-1} at 1000 mA g^{-1} with a capacity retention of 51.2% after 150 cycles (Figure 3.6a). The cycling performance of D-SiO significantly deteriorates with an increase in heating temperature and time. The Si nanoclusters inside

the D-SiO particles cannot react with Li-ions when heat-treated at 1000 ℃ for 20 h due to the impenetrable exterior SiO_2 shell, resulting in a limited reversible capacity of 45.6 mAh g^{-1} at 1000 mA g^{-1}. In contrast, D-SiO samples with carbon coating tend to have improved cycling performance (Figure 3.6b). D-SiO@G-1000-20 had the best cycling performance with a reversible capacity of 1223.2 mAh g^{-1} and capacity retention of 84.2% after 200 cycles. This improvement can be explained by two reasons: 1) the carbon coating prevents the side reactions between D-SiO particles and the electrolyte, facilitating durable cycling,[61] and 2) the heat treatment process increases the density and resistivity of the SiO_2 phase,[110] making Li-ion transport difficult, and resulting in a lower capacity accompanied by a smaller volume change during cycling, which is conducive to a longer cycling life. A capacity increase can be detected from the samples heat-treated at 1000 ℃ and some reports,[55-56] in the incipient tens of cycles (Figure 3.6b), which can be attributed to the additional lithiation of the unreacted SiO_2 phase and its embedded Si nanoclusters.

The cyclic voltammetry (CV) of the SiO and D-SiO@G samples was performed at a scan rate of 0.1 mV S^{-1}. The SiO (Figure 3.6c) and D-SiO@G samples (Figure 3.6d) exhibit reduction peaks in the range of 0.001-0.2 V corresponding to the lithiation of SiO during the third CV cycle, while the oxidation peaks at 0.3-0.5 V can be attributed to the delithiation process. D-SiO@G samples have a smaller redox peak potential difference (ΔE_p: ~ 0.53 V for D-SiO@G samples and ~ 0.55 V for D-SiO samples), and larger redox currents than their corresponding D-SiO samples, indicating a faster and more intense redox reaction response due to the graphene coating. These results are also supported by the electrochemical impedance spectroscopy (EIS) results. The Nyquist plots for all SiO (Figure 3.6e) and D-SiO@G samples (Figure 3.6f) possess one depressed semicircle in the

high-frequency area corresponding to charge transfer and an inclined line in the low-frequency area associated with Li-ion diffusion. The charge-transfer resistance for SiO samples increases when heat-treated at a higher temperature and longer time. The D-SiO@G samples deliver a smaller charge-transfer resistance than the corresponding D-SiO samples for the same reason as the CV results: the graphene coating and the subsequent reduced exterior SiO_2 shell facilitate electron transfer and Li-ion transport.

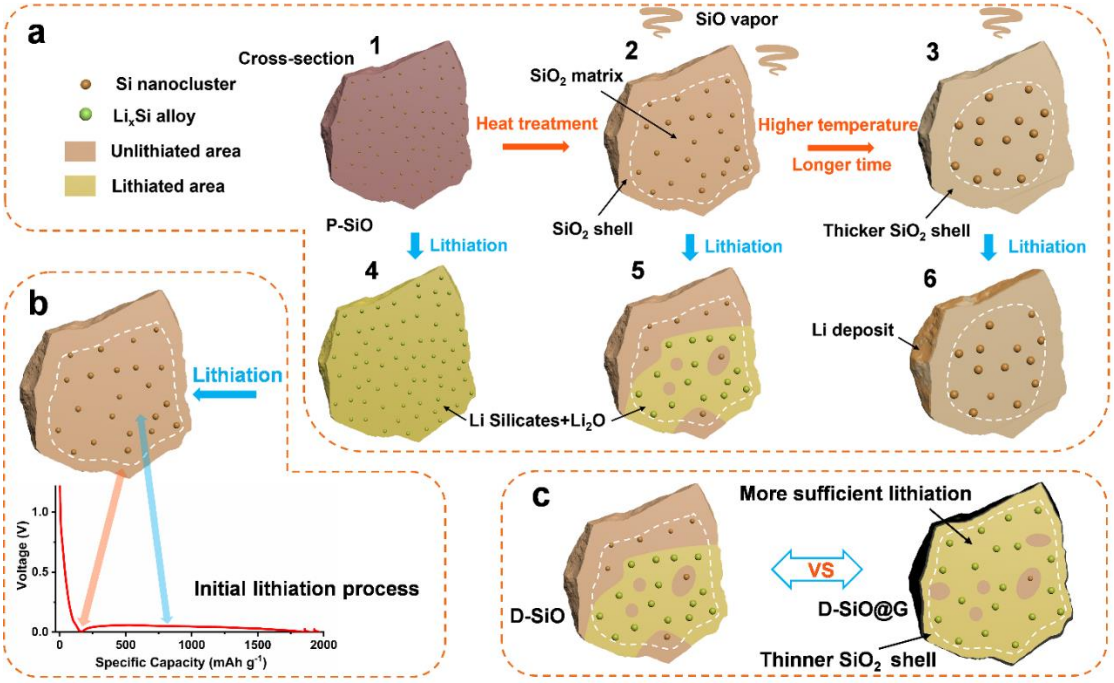

Figure 3. 7. (a) Schematic diagram of the relationship between the electrochemical behavior and the composition and microstructure of SiO induced by heat treatments. The dashed line in each particle denotes the schematic boundary between the SiO_2 shell and SiO_2 matrix. (b) Schematic diagram of D-SiO materials in the initial lithiation process. (c) Schematic diagram of the effect of graphene coating. The particle colors reflect the actual color change observed in the experiment. The dashed line indicates the boundary between the surface and the bulk, corresponding to the boundaries labeled in the HR-TEM image in Figure 3.3. The yellow section in Figures 3.7a4, 7a5, and 7c depict the areas where lithiation occurs effectively.

We investigated the effects of heat treatment and carbon coating processes on SiO composition and microstructure changes and explicated the relationships between their

morphology and electrochemical behaviors. Here, we propose a schematic model in Figure 3.7 to establish the SiO structure evolution during the heat treatment and carbon coating processes. P-SiO has Si nanoclusters in the surrounding amorphous SiO_2 matrix, delivering considerable discharge capacity during the lithiation process (Figures 3.7a1→7a4). The high-temperature heat treatment applied to P-SiO (Figure 3.7a1) triggers disproportionation (Figures 3.7a1→7a2), expediting the Si and SiO_2 phase separation and forming a more inert and denser SiO_2 matrix and larger Si nanoclusters. High temperature also sublimates a certain amount of SiO, generating SiO vapor, which partially deposits onto the top of the sample powder, forming Si nanowires, while a certain proportion condensed and deposited onto the surface of the surrounding SiO particles where oxygen atoms tend to enrich, forming an exterior layer of SiO_2 shell (Figure 3.7a2). The lithiation depicted in Figure 3.7a2→7a5 is insufficient, as evidenced by a capacity loss, compared with P-SiO (Figure 3.7a1) because 1) the SiO_2 phase, including both the exterior SiO_2 shell and interior SiO_2 matrix, has a higher lithiation energy barrier and only partially participated in the lithiation reaction, and 2) the SiO_2 shell on the surface hinders the lithiation of the Si phase since Li-ions must migrate through it before reacting with the interior Si nanoclusters (Figure 3.7b), causing the max overpotential (Figure 3.7b, orange arrow). Further lithiation of the interior Si nanoclusters is also hindered by the inert and resistive interior SiO_2 matrix, resulting in decreased lithiation plateau potential (Figure 3.7b, blue arrow) and some unreacted areas (Figure 3.7a5). When treated at a higher temperature and longer time, the exterior SiO_2 shell becomes thick enough to prevent Li-ions from passing through and cause a Li-deposit onto the D-SiO surface (Figure 3.7a3→Figure 3.7a6) (Figure 3.7a2→7a3), resulting in a significant capacity loss. The

graphene coating process illustrated in Figure 3.6c significantly limited the growth of the exterior SiO_2 shell by confining SiO sublimation at high temperatures, facilitating the charge transfer through the surface, and preventing the side-reactions between SiO and the electrolyte, leading to a thinner and more stable SEI, higher ICE, and better cycling performance.

3.4. Conclusion

In summary, we systematically investigated the composition and structure evolution of amorphous SiO under a series of heat and carbon coating treatments, as well as the resultant electrochemical behaviors, including the initial lithiation profiles, ICEs, and cycling life. SEM and TEM results provide direct evidence of the formation of Si nanowires, the exterior SiO_2 shell, and the interior SiO_2 matrix. Electrochemical testing and XANES analysis indicate the as-formed dielectric SiO_2 phase severely hinders the lithiation process, polarizes electrodes, and subsequently causes severe overpotential, leading to capacity loss and deteriorated cycling life. Carbon coating on SiO effectively restricts the growth of the SiO_2 shell, facilitating the alloy reactions of Li-ions and the interior Si nanoclusters, accompanied by a stable SEI. As a result, a higher ICE (79.3%) and improved cyclability (84.2% after 200 cycles) are achieved. Our findings resolve some of the long-standing questions on SiO, while also offering important insights for the future design and application of SiO-based anode materials.

CHAPTER IV

LIGNITE DERIVED COAL TAR PITCH FOR HIGH-PERFORMANCE SIO/GRAPHITE/C ANODE MATERIALS

4.1. Introduction

Similar to coal-derived HA, which is successfully used as a feedstock for in situ graphene coating, showing promising potential for reducing the cost of synthesizing high-performance anode materials, coal tar pitch also has attracted intensive interest from the LIB industry. Coal tar pitch (CTP) is a bright black solid substance at room temperature, showing a glass phase. That is, as the temperature gradually increases, the CTP will slowly transform from a hard solid state to a soft transition state, which is generally defined as the softening point. Based on the softening point, CTP is divided into low softening point CTP (< 75℃, LS-CTP), medium softening point CTP (75℃ - 95℃, MS-CTP), and high softening point CTP (> 95℃, HS-CTP). Compared with petroleum pitch, CTP usually has a higher degree of polymerization and aromaticity, which is a property of conjugated cycloalkenes in which the stabilization of the molecule is enhanced due to the ability of the electrons in the π orbitals to delocalize.[71, 117] Because of this, carbonized CTP can form a highly conductive network, which is of excellent merit when used in electrode materials. Many high-value carbon materials, such as carbon foam,[118] activated carbon,[71] carbon nanosheets,[119] and graphitic carbons[120] have been successfully synthesized by using CTP as the precursor. These applications indicate a promising potential of CTP in improving SiO's conductivity and volume change during cycling. However, due to the viscous and

organic nature of CTP, previous reports working on CTP mostly involve toxic and organic solvents, such as DMF,[121] NMP,[122] and alcohol,[123] which produce hazardous wastes to the environment and are not cost efficient. A synthesis process that can disperse CTP in water-based solvents and coat SiO at a low cost for LIB electrode material production is highly desired.

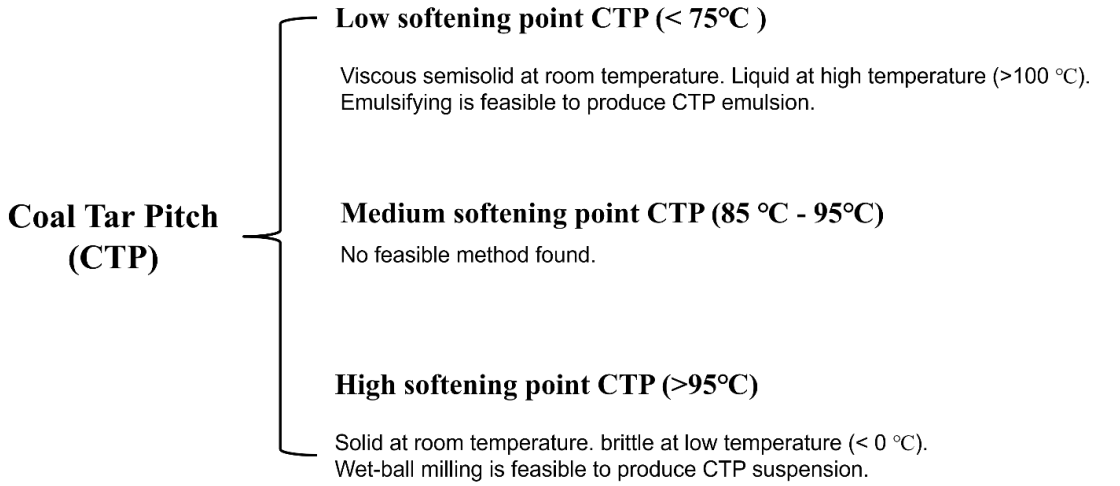

Figure 4. 1. CTP with different softening points.

Herein, SiO anode materials accompanied by low-cost lignite-derived CTP to design effective morphologies and hierarchical structures for high-performance LIBs were performed. We proposed two routes to disperse low softening point CTP and high softening point CTP to synthesize SiO/C composites, respectively. In this study, we closely examined the effects of the composition and softening point of CTPs on the yield and electrochemical performance of SiO/C composites. Due to the confidentiality of an ongoing DOE project, specific information pertaining to specific materials and experimental conditions used is withheld from disclosure.

4.2. Methods

4.2.1. Preparation of LS-CTP Emulsion: The LS-CTP emulsion was prepared with our proprietary process.

4.2.2. Synthesis of SiO/G/C Composite: A SiO/G/C composite was obtained by using the LS-CTP emulsion.

4.2.3. Preparation of HS-CTP Suspension: The LS-CTP emulsion was prepared with our proprietary process.

4.2.4. Synthesis of SiO/C Composite: A SiO/C composite was obtained by using the HS-CTP suspension.

4.2.5. Materials Characterization: Field-emission scanning electron microscopy (FEI Quanta 650 FEG SEM) was used to analyze the particle morphology.

4.2.6. Electrochemical Measurements: The electrode paste was prepared by mixing the composite, a conductive agent (Carbon nanotube), and CMC (Carboxymethyl Cellulose) at a mass ratio of 90: 4: 6 in D.I. water. The paste was then spread onto copper foil and dried overnight at 80 ℃ in a vacuum oven. The coated foil was punched into disk electrodes with diameters of 14 mm. Coin-type cell (CR2032) assembly was performed in an Ar-filled glovebox using the electrode as the working electrode, lithium foil as the counter electrode, a Celgard 2400 membrane as the separator, and 1.2 M $LiPF_6$ in EC/DMC/EMC = 1/1/1 (wt%) with 10 wt% FEC as the electrolyte. The cells were evaluated at 25 ℃ with galvanostatic charge-discharge testing between 0.01 V and 1.5 V (vs. Li/Li^+) on a Neware Battery testing system (CT-4008, Neware Technology Limited, Shenzhen. China). The

current densities and specific capacities were calculated based on the mass of the active materials in the working electrode.

4.3. Results and Discussion

4.3.1. Analysis of SiO/G/C Composite Synthesized by LS-CTP

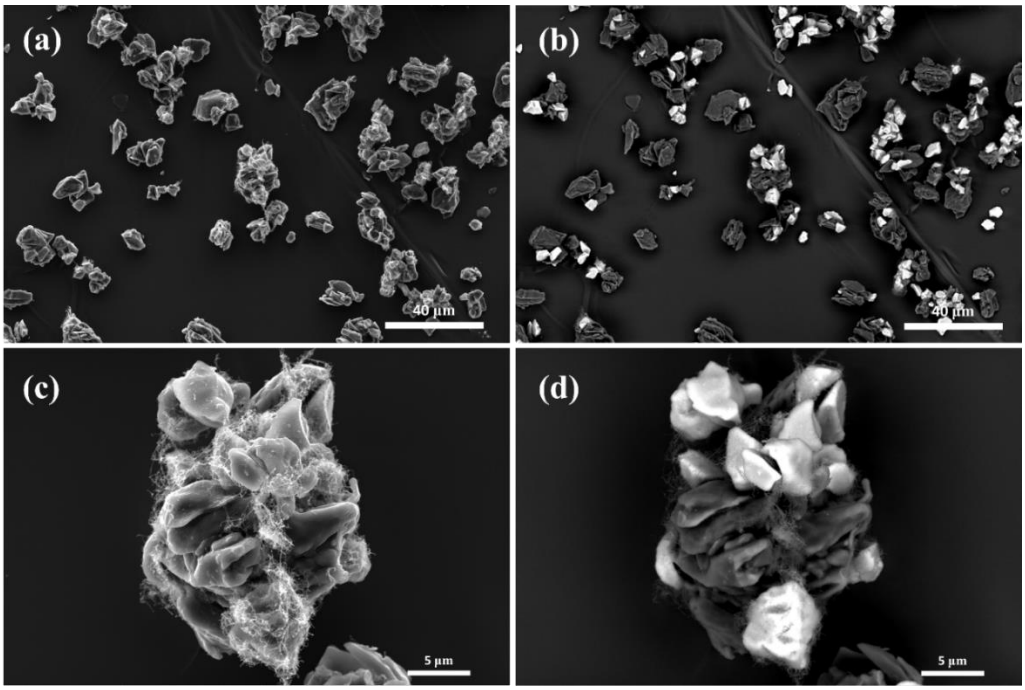

Figure 4. 2. (a) SEM image and (b) corresponding backscatter electron image of SiO/G/C composite. (c) a SEM image and (d) its BSE image of SiO/G/C composite particle.

By using the optimized LS-CTP emulsion, a SiO/G/C composite was obtained after spray drying and calcination. The SEM image of the SiO/G/C composite (Figure 4.6a) exhibits the particle size ranging from 5 to 20 μm. The corresponding BSE image (Figure 4.6b) indicates the even distribution of the brighter SiO among the darker graphite particles. The magnified SEM image (Figure 4.6c) of a SiO/G/C particle shows abundant carbon nanofibers around the particle surface. The carbon nanofibers are formed by the carbonization of CTP during calcination. The corresponding BSE image (Figure 4.6d) indicates the carbon nanofibers act as ropes to bind graphite and SiO particles together.

The close contact of SiO with graphite effectively alleviates SiO's dielectric nature. Moreover, the conductive nature of the nanofibers is conducive to electron transfer and thus facilitates fast charging and discharging.

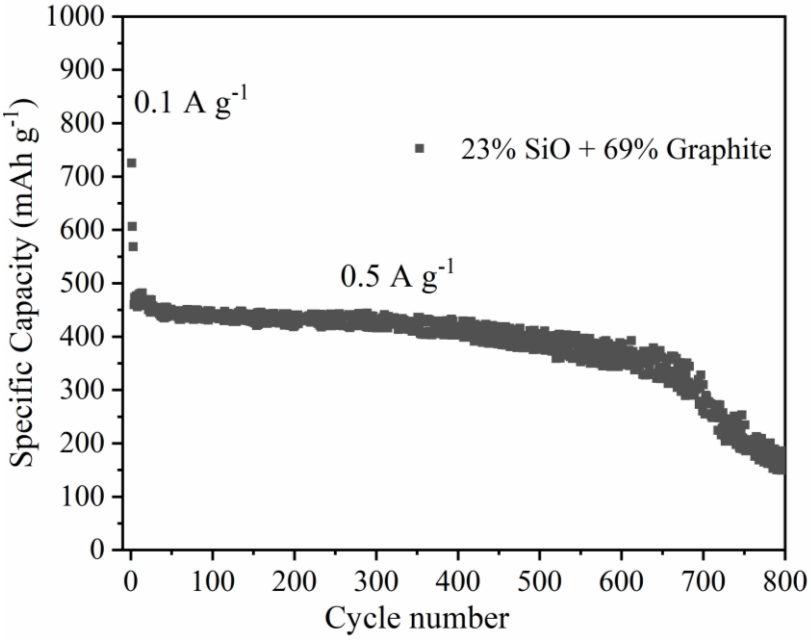

Figure 4. 3. (a) Discharge capacity and cycling performance of the SiO/G/C composite.

The well-connected carbon nanofibers on the SiO and graphite surface create a remarkable improvement in the electrochemical performance, as shown in Figure 4.7. The SiO/G/C composite presents an excellent cycling performance of 84.5% capacity retention after 500 cycles.

4.3.2. Analysis of SiO/C Composite Synthesized by HS-CTP.

The SiO/C composite (Figure 4.8) synthesized by HS-CTP suspension delivers a lithiation capacity close to 2000 mAh g^{-1} at the current density of 0.1 A g^{-1}. When the cycling current increases to 2.0 A g^{-1}, the SiO/C still releases a high reversible capacity (~1000 mAh g^{-1})

with a considerable cycle life (85% capacity retention after 200 cycles), which should be ascribed to the highly conductive carbon coating derived from the high softening CTP.

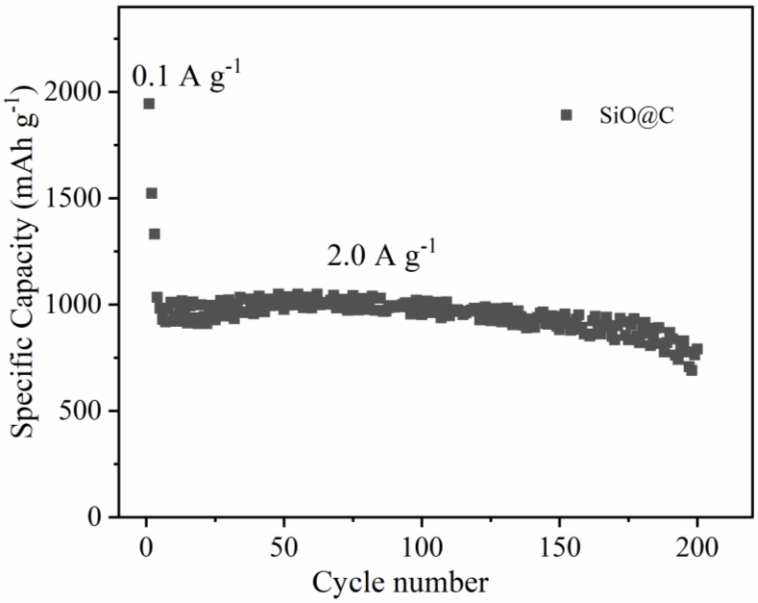

Figure 4. 4. (a) Discharge capacity and cycling performance of the SiO/C composite.

4.4. Conclusion

In summary, we have developed two routes to make the most of CTP in LIB anode materials. By using LS-CTP, the obtained SiO/G/C particle surface presents a conductive network, which binds SiO with graphite closely. Benefiting from the structure, the composite shows a long cycle life with 84.5% capacity retention after 500 cycles. The SiO/C composite synthesized by HS-CTP also shows a high reversible capacity (~1000 mAh g^{-1} at 2.0 A g^{-1}) with a considerable cycle life (85% capacity retention after 200 cycles). Despite the results in this chapter being summarized from an unfinished project

and the lack of many characterizations and testing, the encouraging results have exhibited a bright future for the application of CTP in LIBs.

CHAPTER V

SYNTHESIS OF MICROMETER-SIZED HIERARCHICAL POROUS SI@C ANODES FOR HIGH-PERFRMANCE LITHIUM-ION BATTERIES

5.1. Introduction

Silicon anodes can possess a capacity of 4,200 mAh g^{-1}, which is about double that of SiO anode materials. Silicon resources are also widely available and abundant.[1, 124-125] The high capacity, however, is offset by its drastic volume change during lithiation and delithiation, which pulverizes the Si particles and lowers the electrical contacts with current collectors.[10-11] The side reactions between Si and the electrolyte form the solid-electrolyte interphase (SEI), which is vulnerable to repeated cycling and consumes the electrolyte, resulting in a thick SEI and deteriorated Li^+ transport. These problems all lead to low cycling efficiency and rapid capacity loss.

As discussed in Chapter II, the MR reaction of SiO_2 is an easy and low-cost method to produce microsized porous Si, which has been taken as a promising approach to synthesizing high-performance Si anode materials due to its much smaller surface area compared to nanosized Si. Its mechanical strength is limited though due to its much larger size than that of nano-porous Si, making it easier to fracture during cycling.[32] Graphene coatings have been proposed as an ideal approach to support porous Si structures and limit the side reactions between Si and the electrolyte due to excellent resilience and high conductivity;[61, 68, 126] however, previously manufactured graphene coatings are

sophisticated, need catalysts, and endure harsh conditions during the synthesis process, limiting production substantially.

Coal is classified as low-rank, medium-rank, or high-rank according to the degree of coalification.[127] HA, the primary organic component of low-rank coal (lignite) is derived from peat and has a molecular weight range from several hundred to millions.[128] HA is a dark brown powder where two-thirds of the carbon atoms in its molecular are sp^2 bonded. The rest of the atoms exist primarily in carboxyl groups and hydroxyl groups (Figure 5.1). HA with the unique structure has been demonstrated above to convert to graphene coating facilely on SiO particles,[101] and may also be a promising solution for microsized porous Si.[62, 91, 129-130]

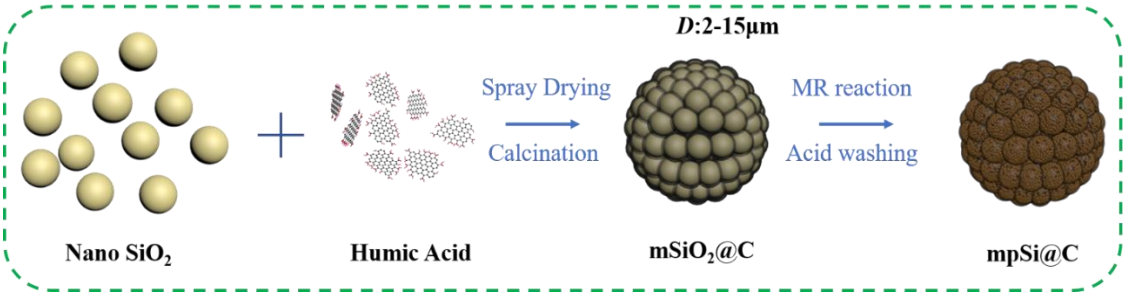

Figure 5. 1. Schematic illustration of the synthetic process of the mpSi@C composite.

In this work, we have introduced SiO_2 nanoparticles ($nSiO_2$) and a feedstock of low-cost coal-derived HA to synthesize micrometer-sized porous Si coated with a graphitized carbon shell (mpSi@C) through spray drying, calcination, and MR reactions (Figure 5.1). The obtained mpSi@C composite possesses a microsized hierarchical graphitized carbon structure that encapsulates the nanoporous Si (npSi) to effectively release the mechanical stress of the Si anode upon lithiation. Detailed electrochemical testing and characterizations were performed to determine the effectiveness of the design.

5.2. Methods

5.2.1. Synthesis of $mSiO_2$@C Composite: A quantity of 3.5 g HA, extracted and purified from North Dakota lignite, was dissolved in 30 mL of D.I. water with ammonium (1.0 mL, 28%–30%, LabChem, USA). The mixture was stirred at 200 rpm for 1 hour, followed by the addition of 10.0 g SiO_2 nanoparticles (500nm) and 0.45 g P123 as a surfactant. The result was stirred vigorously for 2 hours and then spray-dried at an inlet temperature of 200 ℃. The powder obtained from spray drying, $mSiO_2$@HA, was sintered at 300 ℃ for 2 hours, then at 800 ℃ for 5 hours in a high-purity Ar atmosphere to produce $mSiO_2$@C.

5.2.2. Synthesis of the mpSi@C Composite: A total of 0.81 g $mSiO_2$@C powder containing 0.7 g SiO_2 was completely mixed with 0.6g Magnesium powder (325 mesh, Sigma Aldrich, USA) and 4.0 g NaCl powder (Sigma Ultra, USA) in a glovebox. The mixture was sealed in a stainless-steel tube (Figure 5.2) and then heated to 700 ℃ for 5 hours at a heating rate of 4℃/min under an Ar atmosphere. The resulting powder was washed in sequence with HCl solution (10%, A.C.S) for 2 hours and a HF solution (5%, Sigma Aldrich, USA) for 20 minutes to remove impurities. The mpSi@C composite was obtained after D.I. water washing and vacuum drying.

Figure 5. 2. MR reaction in a stainless-steel tube.

5.2.3. Materials Characterization: Powder X-ray diffraction (XRD) was performed on an X-ray diffractometer (Smartlab, Rigaku) using Cu Kα radiation at a scan rate of 2°/minute, from 10°–80°. Field-emission scanning electron microscopy (FEI Quanta 650 FEG SEM) was used to analyze the particle morphology. The Raman spectra were collected with a Raman Spectrometer (HORIBA, 532 nm, 1800 grating). The mpSi@G carbon content was analyzed with a carbon analyzer (TOC-V, SHIMADZU) that uses an SSM 5000A module for solid samples.

5.2.4. Electrochemical Measurements: The electrode paste was prepared by mixing the mpSi@G composite, a conductive agent (Carbon nanotube, Tuball, Luxembourg), and binder (CMC, Tuball, Luxembourg) at a mass ratio of 90: 4: 6 in D.I. water. The paste was then laminated onto copper foil and dried overnight at 80 ℃ in a vacuum oven. The coated foil was punched into disk electrodes with diameters of 14 mm. Coin-type cell (CR2032) assembly was performed in an Ar-filled glovebox using the mpSi@G electrode as the working electrode, lithium foil as the counter electrode, a Celgard 2400 membrane as the

separator, and 1.2 M LiPF6 in EC/DMC/EMC = 1/1/1 (wt%) with 10 wt% FEC as the electrolyte. The cells were evaluated at 25 ℃ with galvanostatic charge-discharge testing between 0.01 V and 1.5 V (vs. Li/Li^+) on a Neware Battery testing system (CT-4008, Neware Technology Limited, Shenzhen. China). The current densities and specific capacities were calculated based on the mass of the active materials in the working electrode. Electrochemical impedance spectroscopy (EIS) and cyclic voltammetry (CV) were performed on a Gamry interface 1010E electrochemical workstation (Gamry Instruments, USA). CV measurements were conducted in the voltage range of 0.01-2.0 V at 0.1 mV S^{-1}. EIS measurements were performed at an AC voltage amplitude of 10 mV and a frequency of 1 MHz to 0.1 Hz.

5.3. Results and Discussion

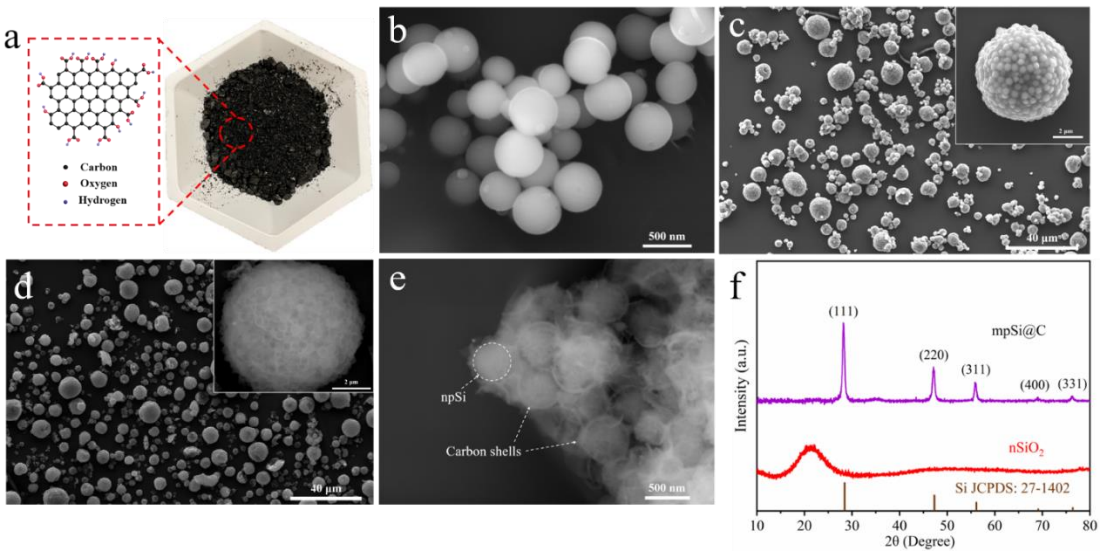

Figure 5. 3. (a) HA powder and its idealized molecular structure. SEM images of (b) $nSiO_2$ particles, (c) $mSiO_2$@C particles and a magnified inset image, (d) mpSi@C particles and a magnified BSE inset image, (e) a broken mpSi@C particle, and (f) XRD patterns of $nSiO_2$ powder and the mpSi@C composite.

We used $nSiO_2$ powder that consists of nano spherical particles with an average particle size of 500 nm (Figure 5.3b). Micrometer-sized SiO_2 coated with graphitized carbon ($mSiO_2$@C) was obtained by spray drying and calcination. Spray drying is a mature technology for the massive production of microsized particles.[131] An $nSiO_2$ and HA slurry was atomized into mist during spray drying, consisting of many small slurry droplets. The droplets contained a water solvent that evaporates instantaneously under the high-temperature inlet gas, leaving the $mSiO_2$@HA particles. The subsequent calcination converted $mSiO_2$@HA to $mSiO_2$@C with a carbon content of 13.6%. Most of the $mSiO_2$@C particles were spherical, with particle sizes ranging from 2-15 μm (Figure 5.3c). The magnified SEM image of a $mSiO_2$@C particle (Figure 5.3c inset) reveals the distribution of $nSiO_2$ and carbon, where $nSiO_2$ constitutes the main body of the $mSiO_2$@C particle and is connected and coated by carbon material. The $nSiO_2$ particles react with the Mg vapor from the sublimation of Mg powder at high temperature, forming Si and MgO, as shown in the magnesiothermic reaction (MR reaction):[29, 31]

$$SiO_2 + 2Mg = Si + 2MgO$$

HCl washing and HF etching removed the MgO and unreacted SiO_2, leaving the mpSi@C particles (Figure 5.3d) with a shape identical to the $mSiO_2$@C particles. The magnified BSE inset image in Figure 5.3d indicates that solid $nSiO_2$ particles were converted to a porous structure. This finding was supported by the high-resolution SEM image of a broken mpSi@C particle (Figure 5.3e), revealing nanoporous Si particles and surrounding carbon shells. This hierarchical structure is conducive to good electrochemical performance during cycling since the carbon network inside the mpSi@C particles increases its conductivity, while the outer carbon coating prevents side reactions between Si and the electrolytes. The XRD patterns in Figure 5.3f confirm the proposed phase change in Figure 1. The broad peak located at 2θ = 15 ~25° indicates the amorphous nature of the $nSiO_2$ powder. A high purity mpSi@C composite was collected after the synthesis process, with all peaks belonging to the Si phase. The Raman spectroscopy analysis was conducted (Figure 5.4), revealing a significant G-band (1585 cm^{-1}) that demonstrates the highly graphitic nature of the carbon in the mpSi@C composite, while the considerable D-band (1350 cm^{-1}) indicates many defects that will facilitate Li-ion transport through the micrometer-sized particles.

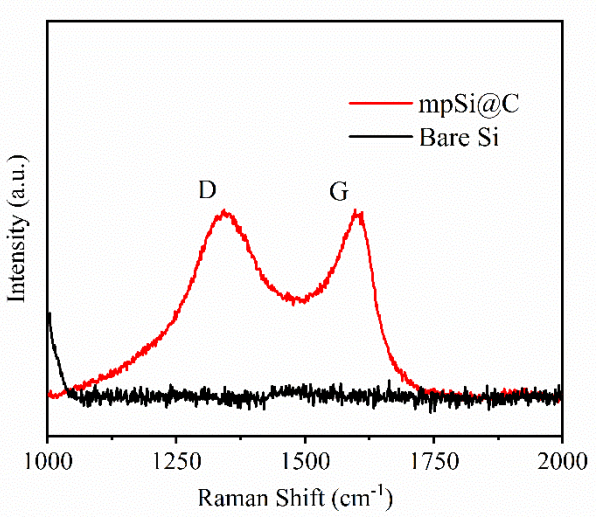

Figure 5. 4. Raman spectra of bare Si and the mpSi@C composites.

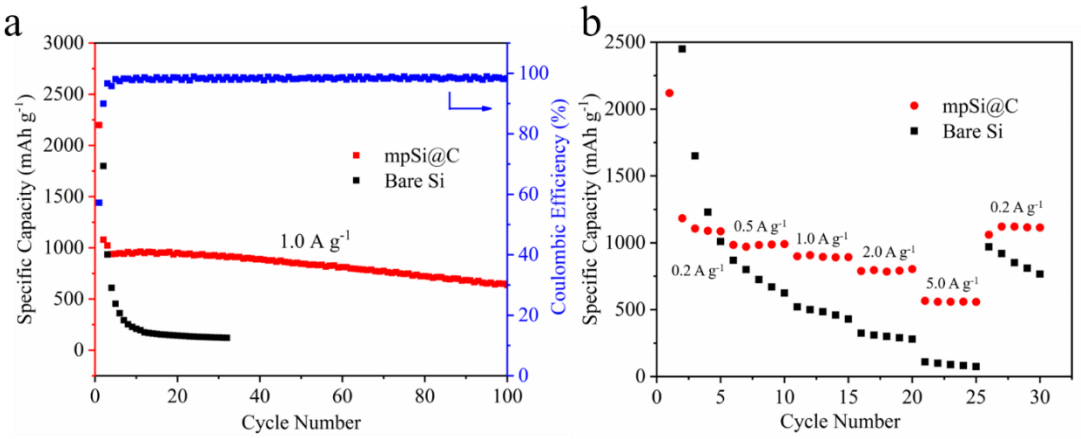

Figure 5. 5. (a) Cycling performance and coulombic efficiency of mpSi@C and the cycling performance of mpSi@C at 1.0 A g^{-1}. (b) Rate capabilities of bare-Si and mpSi@C electrodes.

Cycling and rate testing results (Figure 5.5) reveal a remarkable electrochemical improvement compared to bare Si material. The mpSi@C composite presents a high initial discharge capacity of 2199.9 mAh g^{-1} at 0.1 A g^{-1} (Figure 5.5a), which is lower than the bare Si capacity of 3310.4 mAh g^{-1}; however, due to the benefits from the well-designed hierarchical structure, the mpSi@C composite presents considerable cycling performance at 1.0 A g^{-1}, with a 68% capacity retention after 100 cycles. The capacity of bare Si dropped significantly, below 200 mAh g^{-1} in 10 cycles. The rate capability testing of the mpSi@C composite and bare Si were conducted at a series of current densities. The mpSi@C composite delivered reversible capacities of 1183.7, 984.6, 899.2, 789.1, and 566.3 mAh g^{-1} at current densities of 0.2, 0.5, 1.0, 2.0, 5.0 A g^{-1}, respectively (Figure 5.5b). When the current density was decreased to 0.2 A g^{-1}, the capacity nearly recovered to its original value of 1121.3 mAh g^{-1}. The capacity of bare Si dropped significantly with the increase in current density and could not recover its capacity when the current density returned to 0.2 A g^{-1}. The considerable cycling and rate performance of the mpSi@C composite are contributed to the Si and carbon structure in at least three ways: 1) the nanoporous Si

structure could accommodate the volume change of Si during lithiation/delithiation without breaking the surrounding carbon shell, 2) the highly graphitized carbon structure presented high electrical conductivity for charge transfer through the whole micrometer-sized particle, creating a high rate performance, and 3) the outer carbon coating effectively prevented the reactions between the embedded Si and electrolytes, limiting the growth of the SEI film.

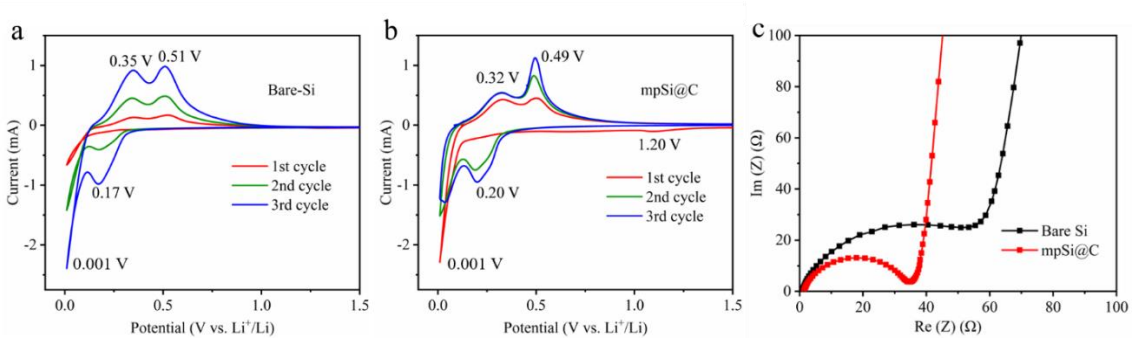

Figure 5. 6. (a) Cyclic voltammetry curves of bare-Si and (b) mpSi@C at a scan rate of 0.1 mV S^{-1} for the first three cycles. (c) Nyquist plots of bare-Si and mpSi@C electrodes before cycling.

The CV curves in Figures 5.6a and 5.6b describe the first three cycles of the bare-Si and mpSi@C composite at a scan rate of 0.1 mV S^{-1}. The initial mpSi@C cathodic scan revealed a broad peak at 1.2 V that should be attributed to the SEI film formation between the carbon shell and the electrolyte. The reductive peak in the range of 0.01-0.2V corresponds to the Si phase lithiation in bare Si and mpSi@C. The two oxidation peaks at 0.35 and 0.51 V for bare Si and 0.32 and 0.49 V for mpSi@C can be attributed to the removal of lithium from the as-formed Li_xSi alloy. The peak current increased gradually from the first to third cycle as more Si participated in the alloying process. The difference between the redox peak potential (ΔE_p) for mpSi@C at 0.001 V and 0.49 V was smaller than that of the bare Si at 0.001 V and 0.51 V, indicating a faster current response in mpSi@C due to the hierarchical Si and carbon structure, which facilitates electron transfer

and Li-ion transport during potential scanning. These results are supported by the Nyquist results (Figure 5.6c) obtained from electrochemical impedance spectroscopy (EIS) analysis. Nyquist plots for both bare Si and mpSi@C exhibit one depressed semicircle in the high-frequency range, corresponding to charge-transfer resistance and an inclined line in the low-frequency region associated with Li^+ diffusion.[132] Apparently, the mpSi@C composite possesses a much smaller charge-transfer resistance than bare Si due to its much smaller semicircle.

5.4. Conclusion

In summary, we have demonstrated a feasible approach to creating a mpSi@C composite using SiO_2 nanoparticles and a feedstock of coal-derived HA. The rationally designed carbon structure hinders the side reactions between the electrolyte and the embedded nanoporous Si, significantly improving the conductivity of the composite. The mpSi@C composite presents a remarkable cycling performance of 68% capacity retention after 100 cycles and rate capabilities of 566.3 mAh g^{-1} at 5.0 A g^{-1}. This work provides a new and practical approach for improving Si anode performance for use in LIBs.

CHAPTER VI

SYNTHESIS OF COAL FLY ASH DERIVED HOLLOW POROUS SI@G ANODE FOR HIGH-PERFORMANCE LITHIUM-ION BATTERIES

6.1. Introduction

Massively synthesizing high-performance Si anodes at an affordable cost to replace graphite is still challenging because this not only requests a delicate structure design to alleviate the dramatic volume change of Si during cycling but also needs a durable, conductive, and inert coating to prevent Si from consuming electrolytes. Microsized porous Si synthesized by the MR reaction of SiO_2 has been taken as a promising method to produce high-performance Si anode materials due to its much lower reaction temperatures than conventional silicon production and controllable porosity. Jia et al.[22] reported a typical microporous silicon composite synthesized by reducing micro-silica that was made by a microemulsion approach and demonstrated high rate capability (~ 650 mAh g^{-1} at 11 A g^{-1}) and cycling stability (370 cycles with 83% capacity retention), showing bright future for application. Moreover, the MR reaction used in this article has become a focus of research in recent years as many abundant and cheap silica resources, such as rice husk, sand, and coal fly ash (CFA), can be used as feedstocks to reduce synthesis costs. Unlike other massive silicon resources, there is a pressing and ongoing need to develop clean recycling methods for CFA as its improper disposal is a big environmental concern. With the huge global energy demand and colossal utilization of coal to meet energy needs, it is estimated about 750 million tons of coal fly ash were produced in a single year and only $1/4^{th}$ was

utilized[74, 133]. CFA is mostly collected from the electrostatic precipitator of power plants with a size distribution mainly from 2 μm to 50 μm. It is commonly a hollow or solid spherical structure (depending on parent coal), and contains 20-60% silica with porosity of 30-65%[133-134]. All these features – abundant and high silica content, microsize spheres, and hollow porous structure make it an excellent template and silicon source to synthesize high-performance silicon anodes. Xing et al.[135] used the "NaOH etching – HCl extracting – Mg reduction – HCl washing" process transforming fly ash into nanostructured silicon powders. The synthesized nanostructured silicon exhibited good electrochemical performance (1450.3 mAh g^{-1} at 4.0 A g^{-1}). However, the authors just took fly ash as a massive Si source to extract pure silica and didn't make the most of its unique spherical and hollow porous structure, which is extremely useful in silicon anode design.

Herein, based on the work in Chapter V, we further reduce the cost of synthesizing high-performance Si anodes by making the most of coal fly ash, a cheap and massive by-product from power plants, as the Si source and structure template to in-situ synthesize hierarchical hollow porous Si@C composites (HPSi@C). The hollow and porous structure allows the Si anode to expand and contract freely during lithiation and delithiation. The carbon coating acts as an effective electrolyte barrier and structure sustainer to keep the electrochemical performance composites from decaying during long-time cycling. The obtained HPSi@C composite possesses a microsized hierarchical graphitized carbon structure that encapsulates the hollow porous Si to effectively release the mechanical stress of the Si anode upon lithiation. Detailed electrochemical testing and characterizations were performed to determine the effectiveness of the design.

6.2. Methods

6.2.1. Pretreatment and Classification of Coal Fly Ash: Coal fly ash (191 g) from the Wabash River highland power plant was first calcinated at 700 ℃ for 5 h to fully oxidize residual carbon and subsequently leached with 200 mL D.I. water and 50 mL HCl (37%, Fisher Chemical, USA) overnight to remove reactive compounds. After this, the leached fly ash was mixed with 3% PEG 4000 (EMD Millipore, USA) and stirred vigorously to form a homogeneous suspension. The suspension was rested for a certain time to deposit. By adjusting the sedimentation time and repeated sedimentation (Figure 6.1a), a series of classified fly ash beads (CFAB) with even particle sizes were obtained (CFAB-1, CFAB-2, CFAB-3, CFAB-4) upon vacuum drying.

6.2.2. Synthesis of HPSi@SiC Beads: 0.65g CFAB beads were fully mixed with 0.43 g Mg powder and 6.0 g NaCl powder in a glovebox. The mixture was sealed in a stainless container and then heated to 750 ℃ for 5h at a heating rate of 4℃/min under an Ar atmosphere. After this magnesiothermic reduction, the obtained powder was soaked in HCl solution (5%) overnight followed by D.I. water washing. The resulting hollow porous beads (HPSib) were subsequently combined with NH_3 solution (28%, 3.0mL), D.I. water (200 mL), and CTAB (0.10 g). After vigorously stirring for 1 h, 0.4 g resorcinol (Alfa Aesar, USA) and 0.56 mL formaldehyde (37.0%, J.T Baker, USA) were added and stirred overnight. HPSi@RF beads were collected after filtering and drying under a vacuum. By sintering the HPSi@RF beads at 800 ℃ for 5 h under Ar flowing, followed by 5% HF etching for 1 h to fully remove unreacted SiO2, HPSi@C beads were obtained after water washing and drying in a vacuum.

6.2.3. Materials Characterization: Powder X-ray diffraction (XRD) was performed on an X-ray diffractometer (Smartlab, Rigaku) operated at 40kV and 44mA using Cu Kα radiation at a scan rate of 4°/min from 10° – 80°. The particle morphology and element composition were analyzed by a field-emission scanning electron microscopy (FEI Quanta 650 FEG SEM) equipped with an energy-dispersive X-ray (EDX) spectrometer and field-emission transmission electron microscopy (FE-TEM, JEM-2100F, JEOL, 200 kV).

6.2.4. Electrochemical Measurements: The HPSi@SiC electrode slurry was prepared by mixing HPSi@SiC beads, conductive agent (Carbon nanotube, Tuball), and binder (CMC, Tuball) at a ratio of 90: 4:6 in D.I. water. The slurry was then laminated onto copper foil and dried at 100 ℃ in a vacuum oven overnight. The coated foil was punched into disk electrodes with diameters of 14 mm. CR2032 coin-type cells were assembled in an Ar-filled glovebox with the HPSi@SiC electrode as the working electrode, lithium foil as the counter electrode, Celgard 2400 membrane as the separator, and 1.2 M $LiPF_6$ in EC/DMC/EMC = 1/1/1 (wt%) with 10 wt% FEC as the electrolyte. The Mass loading for HPSi@SiC beads was 0.7 mg cm^{-2}. The cells were tested by galvanostatic charge-discharge testing between 0.001 V and 2.0 V (vs. Li/Li^+) on a Neware Battery testing system (CT-4008, Neware Technology Limited, Shenzhen. China). The current densities and specific capacities were calculated based on the mass of active materials in the working electrode. CV (cyclic voltammetry) and EIS (electrochemical impedance spectroscopy) were performed on a Gamry Series G 750 electrochemical workstation (Gamry Instruments, Warminster, USA). CV measurements were conducted in the voltage range of 0.01-2.0V at 0.1 mV S^{-1}. EIS measurements were carried out at an AC voltage amplitude of 10 mV and frequency from 300 kHz to 0.01 Hz.

6.3. Results and Discussion

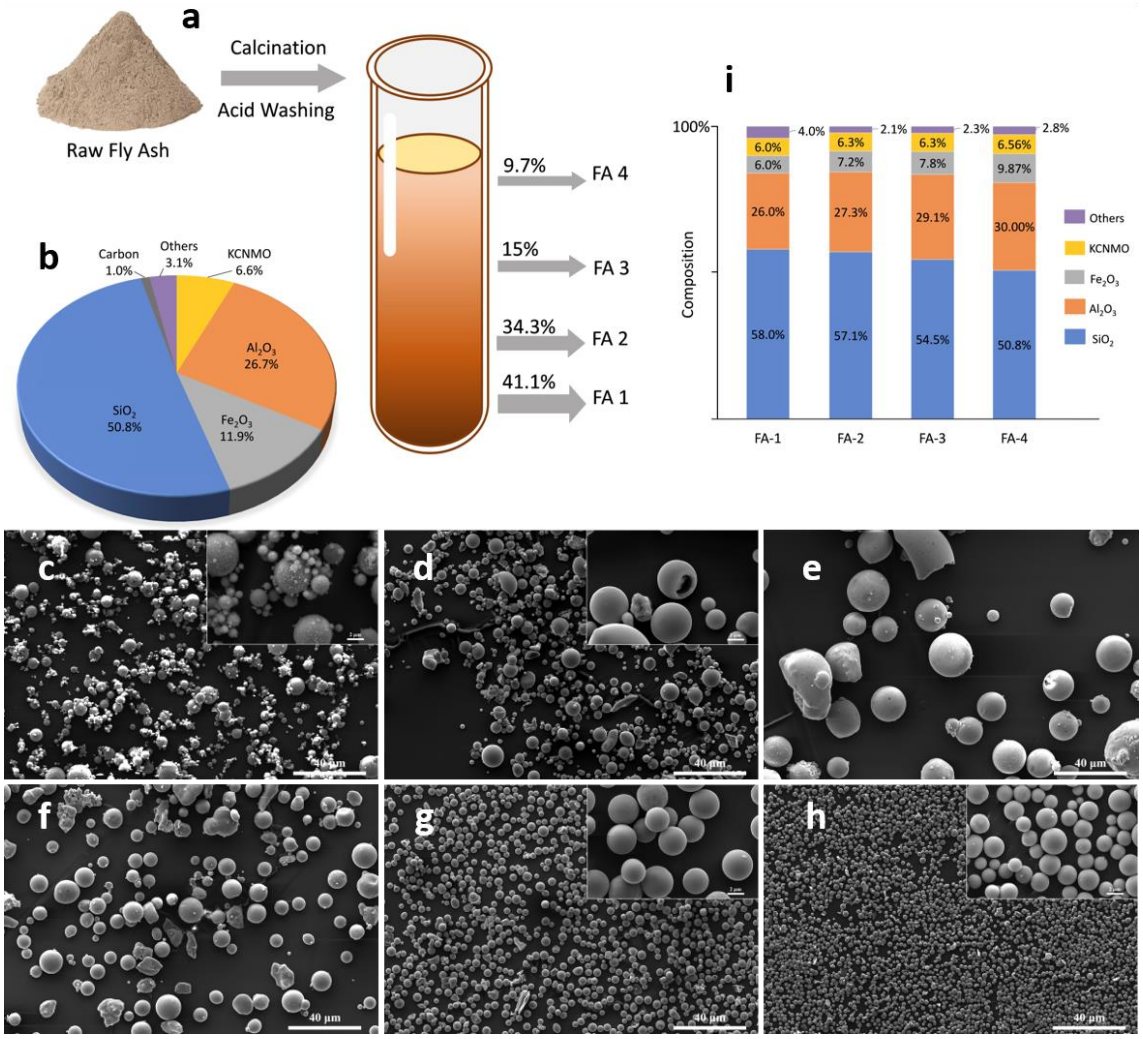

Figure 6. 1. (a) Pretreatment and classification of raw CFA. (b) composition of raw CFA. SEM images of (c) raw CFA, (d) acid washed CFA, (e) CFAB-1, (f) CFAB-2, (g) CFAB-3, (h) CFAB-4. (i) Chemical composition of etched CFABs.

XRF results in Figure 6.1b indicate that raw fly ash has the composition of 50.8% SiO_2, 11.9% Fe_2O_3, 26.7% Al_2O_3, 6.6% KCNMO (stands for the sum of K_2O, CaO, NaO, and MgO as they have similar properties), 1% carbon, and 3.1% others (trace cation's oxides). The high content of SiO_2 makes coal fly ash to be a promising feedstock for silicon anode. In addition, SiO_2 tends to form the thick outer crust, encapsulating compounds, such as Al_2O_3 and Fe_2O_3, during the formation of the coal fly ash beads.[136-137] The SEM image

(Figure 6.1c) shows the raw fly ash beads are mostly spherical in shape, with a diameter ranging from about 1-30 μm. From the magnified in-set, on the beads' surface, we can see a layer of nanoscale dust, which is supposed to be CaO absorbed by fly ash during its formation. By calcination and acid washing to eliminate its carbon and some soluble inorganic compounds, the generated SiO_2-rich beads show a similar diameter range but with a smooth surface (Figure 6.1d). Besides, we can also observe some broken SiO_2-rich beads have a hollow structure, which is an excellent template for synthesizing hollow porous Si anodes. To obtain monodisperse silicon-rich beads, we used a simple but very effective method – sedimentation – to classify these beads, as sedimentation speed is proportional to the square of particle size.[138]

$$Vg = \frac{D^2(\sigma - \rho)g}{18\eta}$$

By optimizing the sedimentation time and after repeated sedimentations, a series of deposits (CFAB-1, CFAB-2, CFAB-3, CFAB-4) were obtained. SEM images of these deposits (Figure 6.1e, 1f, 1g, 1h) demonstrate the classification's effectiveness. The particle size of each deposit is similar and gradually decreases from CFAB-1(~ 30 μm), CFAB-2 (~ 10 μm), CFAB-3 (~ 5 μm), to CFAB-4 (1-2 μm). XRF results (Figure 6.1i)of these deposits indicate a decrease in SiO_2 content from FA-1 (58%) to FA-4 (50.8%), with increases in Al_2O_3 and Fe_2O_3 content. The particle size and composition of the classified components will surely impact the morphology and electrochemical performance of synthesized composites.

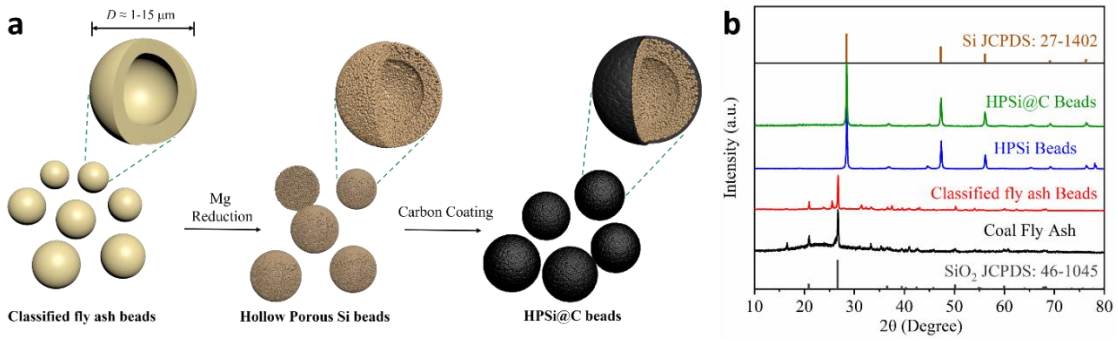

Figure 6. 2. (a) Schematic illustration of the synthetic process of the HPSi@C beads. (b) XRD patterns of raw fly ash, classified fly ash, HPSi beads, and final HPSi@C beads.

Figure 6.2 (a) illuminates the synthetic process of the HPSi@C beads. We make the most of the unique hollow structure of fly ash beads, by MR reaction, to reduce the SiO_2 and other metallic oxides in situ. After HCl washing to remove soluble matters, only Si is left with a hollow porous structure. The following RF coating and calcination process form a layer of carbon coating, which improve the electrical conductivity of the composite significantly while preventing the side reactions between the hollow porous Si and electrolyte. The XRD results in Figure 6.2b confirm the proposed phase change over the synthetic process. Raw coal fly ash possesses the XRD patterns with a broad bump in $2\theta = 15 - 35°$, containing many amorphous compounds, while the most significant peaks belong to SiO_2. Due to HCl washing, the broad bump disappears in the classified fly ash. The following MR reaction and HCl washing successfully converted SiO_2 to Si while removing other components, as indicated by the XRD pattern of the HPSi beads, with little impurity left. The final carbon coating process didn't make observable composition changes as indicated in the XRD pattern of HPSi@C beads.

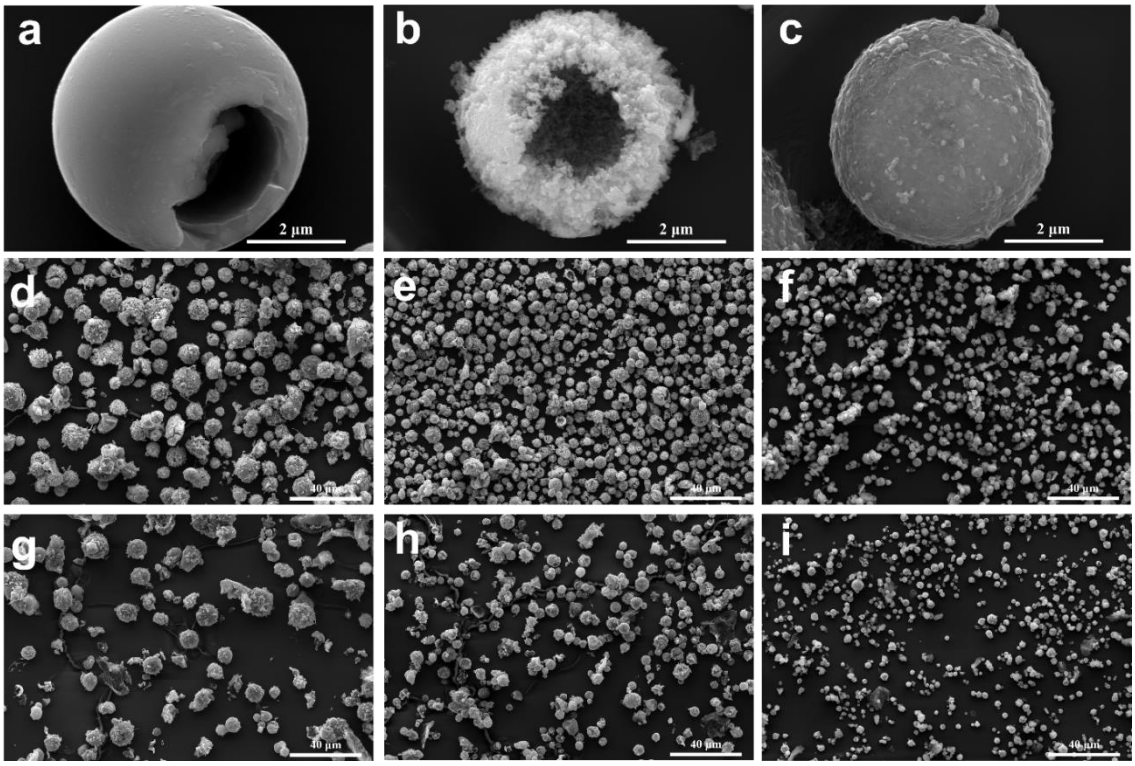

Figure 6. 3. HRSEM image of (a) a broken HCl-washed CFAB-3 bead, (b) a broken HPSi-3 bead, (c) a HPSi@C-3 bead. SEM image of (d) HPSi-2, (e) HPSi-3, (f) HPSi-4 beads produced from CFAB-2, CFAB-3, and CFAB-4, respectively. SEM of (g) HPSi@C-2, (h) HPSi@C-3, (i) HPSi@C-4 beads.

The HRSEM images (Figure 6.3a, b, c) show the morphology of a broken HCl-washed fly ash bead, a broken HPSi-3 bead, and an intact HPSi@C-3 bead, respectively, demonstrating that the unique structure template of coal fly ash is retained after all the synthetic procedures. The MR reaction removes O from SiO_2, leaving a porous Si structure. The void in the porous and hollow structure can accommodate the volume change of Si freely without breaking the structure, resulting in good structural stability. HPSi-2 (Figure 6.3d), HPSi-3 (Figure 6.3e), HPSi-4 beads (Figure 6.3f) and following HPSi@C-2 (Figure 6.3g), HPSi@C-3 (Figure 6.3h), and HPSi@C-4 (Figure 6.3i) beads were produced individually by using classified fly ash component CFAB-2, CFAB-3, and CFAB-4,

respectively. These SEM results show similar monodisperse beads to their corresponding fly ash components, suggesting the effectiveness of the design.

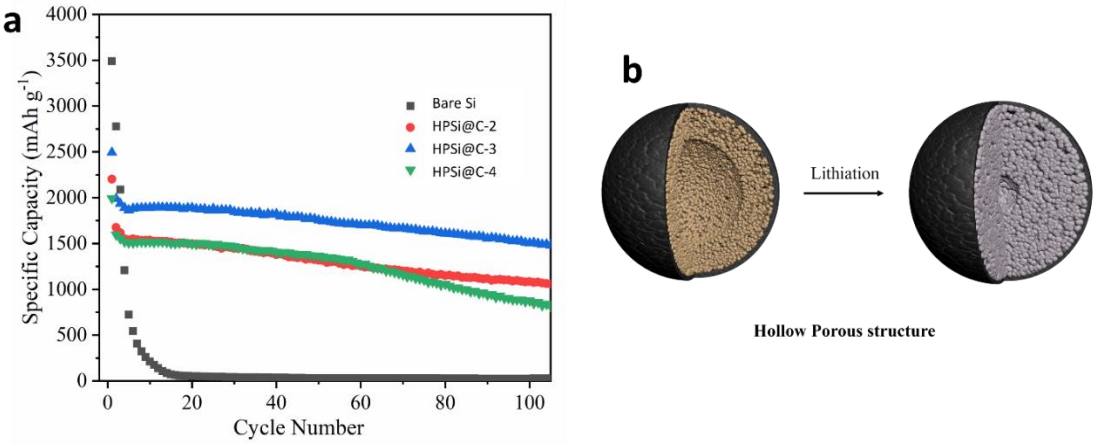

Figure 6. 4. (a) Cycling performance of HPSi@C-2, HPSi@C-3, HPSi@C-4 beads, and bare Si anodes. (b) Hollow-porous structure of Si and the hollow-porous structure after lithiation.

The cycling testing results (Figure 6.4a) reveal the cycling performance of HPSi@C-2, HPSi@C-3, HPSi@C-4 beads, and bare Si anodes. The capacity of bare Si dives quickly to below 100 mAh/g in 20 cycles despite a high initial discharge capacity of 3502 mAh/g, while all the HPSi@C composites present much better cycling life. Among them, the HPSi@C-3 presents the best cycling performance and delivers the highest reversible capacity and capacity retention (85.1% retention after 100 cycles). The significant improvements come from the unique hierarchical structure of CFA beads and the in-situ intact carbon coating. As shown in Figure 6.4b, the hollow porous structure formed in MR reaction effectively mitigates the stress from Si's volume change during lithiation/delithiation, while the carbon coating shell prevents the side reactions between Si and the electrolytes. As a result of the design, the excellent cycling performance of the HPSi@C beads is achieved.

6.4. Conclusion

In conclusion, power plant waste CFA as the Si feedstock and structural template is successfully used to synthesize hierarchical HP Si@C composites. The hollow and porous structure inherited from the CFA allows the Si anode to expand and contract freely during cycling. Besides, the in-situ synthesized carbon coating acts as a barrier to prevent the reactions between the Si and electrolyte. Benefiting from the design, the hierarchical HPSi@C composite shows promising potential for application in LIBs. In the booming era of renewable energy, the low-cost CFA brings new perspectives to the synthesis of Si anode materials.

REFERENCES

1. Armand, M.; Tarascon, J.-M., Building better batteries. *Nature* **2008,** *451* (7179), 652.

2. Yoshino, A., The birth of the lithium‐ion battery. *Angew. Chem. Int. Ed.* **2012,** *51* (24), 5798-5800.

3. Larcher, D.; Tarascon, J.-M., Towards greener and more sustainable batteries for electrical energy storage. *Nat. Chem.* **2015,** *7* (1), 19.

4. Zubi, G.; Dufo-López, R.; Carvalho, M.; Pasaoglu, G., The lithium-ion battery: State of the art and future perspectives. *Renew. Sustain. Energy Rev* **2018,** *89*, 292-308.

5. Tarascon, J.-M.; Armand, M., Issues and challenges facing rechargeable lithium batteries. In *Materials for Sustainable Energy: A Collection of Peer-Reviewed Research and Review Articles from Nature Publishing Group*, World Scientific: 2011; pp 171-179.

6. Nitta, N.; Wu, F.; Lee, J. T.; Yushin, G., Li-ion battery materials: present and future. *Mater. Today* **2015,** *18* (5), 252-264.

7. Marker, K.; Reeves, P. J.; Xu, C.; Griffith, K. J.; Grey, C. P., Evolution of structure and lithium dynamics in $LiNi_{0.8}Mn_{0.1}Co_{0.1}O_2$ (NMC811) cathodes during electrochemical cycling. *Chem. Mater.* **2019,** *31* (7), 2545-2554.

8. Casimir, A.; Zhang, H.; Ogoke, O.; Amine, J. C.; Lu, J.; Wu, G., Silicon-based anodes for lithium-ion batteries: Effectiveness of materials synthesis and electrode preparation. *Nano Energy* **2016,** *27*, 359-376.

9. Zuo, X.; Zhu, J.; Müller-Buschbaum, P.; Cheng, Y.-J., Silicon based lithium-ion battery anodes: A chronicle perspective review. *Nano Energy* **2017,** *31*, 113-143.

10. Shi, F.; Song, Z.; Ross, P. N.; Somorjai, G. A.; Ritchie, R. O.; Komvopoulos, K., Failure Mechanisms of Single-Crystal Silicon Electrodes in Lithium-ion Batteries. *Nat. Commun.* **2016,** *7*, 11886.

11. Ge, M.; Fang, X.; Rong, J.; Zhou, C., Review of Porous Silicon Preparation and its Application for Lithium-Ion Battery Anodes. *Nanotechnology* **2013,** *24* (42), 422001.

12. Liu, X. H.; Zhong, L.; Huang, S.; Mao, S. X.; Zhu, T.; Huang, J. Y., Size-dependent fracture of silicon nanoparticles during lithiation. *ACS Nano* **2012,** *6* (2), 1522-1531.

13. Gu, M.; He, Y.; Zheng, J.; Wang, C., Nanoscale silicon as anode for Li-ion batteries: The fundamentals, promises, and challenges. *Nano Energy* **2015,** *17*, 366-383.

14. Wang, B.; Li, X.; Qiu, T.; Luo, B.; Ning, J.; Li, J.; Zhang, X.; Liang, M.; Zhi, L., High volumetric capacity silicon-based lithium battery anodes by nanoscale system engineering. *Nano Lett.* **2013,** *13* (11), 5578-5584.

15. Kasavajjula, U.; Wang, C.; Appleby, A. J., Nano-and bulk-silicon-based insertion anodes for lithium-ion secondary cells. *J. Power Sources* **2007,** *163* (2), 1003-1039.

16. Szczech, J. R.; Jin, S., Nanostructured Silicon for High Capacity Lithium Battery Anodes. *Energy Environ. Sci.* **2011,** *4* (1), 56-72.

17. Chan, C. K.; Peng, H.; Liu, G.; McIlwrath, K.; Zhang, X. F.; Huggins, R. A.; Cui, Y., High-performance lithium battery anodes using silicon nanowires. *Nat. Nanotechnol.* **2008,** *3* (1), 31-35.

18. Hu, J.; Bando, Y.; Liu, Z.; Zhan, J.; Golberg, D.; Sekiguchi, T., Synthesis of crystalline silicon tubular nanostructures with ZnS nanowires as removable templates. *Angew. Chem.* **2004,** *116* (1), 65-68.

19. Park, M.-H.; Kim, M. G.; Joo, J.; Kim, K.; Kim, J.; Ahn, S.; Cui, Y.; Cho, J., Silicon nanotube battery anodes. *Nano Lett.* **2009,** *9* (11), 3844-3847.

20. Liu, N.; Wu, H.; McDowell, M. T.; Yao, Y.; Wang, C.; Cui, Y., A yolk-shell design for stabilized and scalable Li-ion battery alloy anodes. *Nano Lett.* **2012,** *12* (6), 3315-3321.

21. Rehman, W. U.; Wang, H.; Manj, R. Z. A.; Luo, W.; Yang, J., When Silicon Materials Meet Natural Sources: Opportunities and Challenges for Low‐Cost Lithium Storage. *Small* **2019**, 1904508.

22. Jia, H.; Zheng, J.; Song, J.; Luo, L.; Yi, R.; Estevez, L.; Zhao, W.; Patel, R.; Li, X.; Zhang, J.-G., A novel approach to synthesize micrometer-sized porous silicon as a high performance anode for lithium-ion batteries. *Nano Energy* **2018,** *50*, 589-597.

23. Ge, M.; Lu, Y.; Ercius, P.; Rong, J.; Fang, X.; Mecklenburg, M.; Zhou, C., Large-scale fabrication, 3D tomography, and lithium-ion battery application of porous silicon. *Nano Lett.* **2014,** *14* (1), 261-268.

24. Xiao, Q.; Gu, M.; Yang, H.; Li, B.; Zhang, C.; Liu, Y.; Liu, F.; Dai, F.; Yang, L.; Liu, Z., Inward lithium-ion breathing of hierarchically porous silicon anodes. *Nat. Commun.* **2015,** *6* (1), 1-8.

25. Ge, M.; Rong, J.; Fang, X.; Zhang, A.; Lu, Y.; Zhou, C., Scalable preparation of porous silicon nanoparticles and their application for lithium-ion battery anodes. *Nano Research* **2013,** *6* (3), 174-181.

26. Lai, Y.; Thompson, J. R.; Dasog, M., Metallothermic reduction of silica nanoparticles to porous silicon for drug delivery using new and existing reductants. *Chem. Eur. J.* **2018,** *24* (31), 7913-7920.

27. Shivaraju, G.; Sudakar, C.; Prakash, A., High-rate and long-cycle life performance of nano-porous nano-silicon derived from mesoporous MCM-41 as an anode for lithium-ion battery. *Electrochim. Acta* **2019,** *294*, 357-364.

28. Liu, N.; Lu, Z.; Zhao, J.; McDowell, M. T.; Lee, H.-W.; Zhao, W.; Cui, Y., A pomegranate-inspired nanoscale design for large-volume-change lithium battery anodes. *Nat. Nanotechnol.* **2014,** *9* (3), 187-192.

29. Entwistle, J.; Rennie, A.; Patwardhan, S., A review of magnesiothermic reduction of silica to porous silicon for lithium-ion battery applications and beyond. *J. Mater. Chem. A* **2018,** *6* (38), 18344-18356.

30. Bao, Z.; Weatherspoon, M. R.; Shian, S.; Cai, Y.; Graham, P. D.; Allan, S. M.; Ahmad, G.; Dickerson, M. B.; Church, B. C.; Kang, Z., Chemical reduction of three-dimensional silica micro-assemblies into microporous silicon replicas. *Nature* **2007,** *446* (7132), 172-175.

31. Shi, L.; Wang, W.; Wang, A.; Yuan, K.; Yang, Y., Understanding the impact mechanism of the thermal effect on the porous silicon anode material preparation via magnesiothermic reduction. *J. Alloys Compd.* **2016,** *661*, 27-37.

32. Wang, W.; Favors, Z.; Ionescu, R.; Ye, R.; Bay, H. H.; Ozkan, M.; Ozkan, C. S., Monodisperse porous silicon spheres as anode materials for lithium ion batteries. *Sci. Rep.* **2015,** *5*, 8781.

33. Michan, A. L.; Parimalam, B. S.; Leskes, M.; Kerber, R. N.; Yoon, T.; Grey, C. P.; Lucht, B. L., Fluoroethylene carbonate and vinylene carbonate reduction: Understanding lithium-ion battery electrolyte additives and solid electrolyte interphase formation. *Chem. Mater.* **2016,** *28* (22), 8149-8159.

34. Ren, W.-F.; Zhou, Y.; Li, J.-T.; Huang, L.; Sun, S.-G., Si anode for next-generation lithium-ion battery. *Curr. Opin. Electrochem.* **2019,** *18*, 46-54.

35. Choi, S.; Kwon, T.-w.; Coskun, A.; Choi, J. W., Highly elastic binders integrating polyrotaxanes for silicon microparticle anodes in lithium ion batteries. *Science* **2017,** *357* (6348), 279-283.

36. Guo, J.; Wang, C., A polymer scaffold binder structure for high capacity silicon anode of lithium-ion battery. *Chem. Commun.* **2010,** *46* (9), 1428-1430.

37. Jiao, X.; Yin, J.; Xu, X.; Wang, J.; Liu, Y.; Xiong, S.; Zhang, Q.; Song, J., Highly Energy‐Dissipative, Fast Self‐Healing Binder for Stable Si Anode in Lithium‐Ion Batteries. *Adv. Funct. Mater.* **2021,** *31* (3), 2005699.

38. Kwon, T.-w.; Choi, J. W.; Coskun, A., The emerging era of supramolecular polymeric binders in silicon anodes. *Chem. Soc. Rev.* **2018,** *47* (6), 2145-2164.

39. Kim, J.-H.; Park, C.-M.; Kim, H.; Kim, Y.-J.; Sohn, H.-J., Electrochemical Behavior of SiO Anode for Li Secondary Batteries. *J. Electroanal. Chem.* **2011,** *661* (1), 245-249.

40. Liu, Z.; Yu, Q.; Zhao, Y.; He, R.; Xu, M.; Feng, S.; Li, S.; Zhou, L.; Mai, L., Silicon Oxides: A Promising Family of Anode Materials for Lithium-Ion Batteries. *Chem. Soc. Rev.* **2019,** *48* (1), 285-309.

41. Yang, J.; Takeda, Y.; Imanishi, N.; Capiglia, C.; Xie, J.; Yamamoto, O., SiOx-based anodes for secondary lithium batteries. *Solid State Ion.* **2002,** *152*, 125-129.

42. Yasaitis, J. A.; Kaplow, R., Structure of amorphous silicon monoxide. *J. Appl. Phys.* **1972,** *43* (3), 995-1000.

43. Hohl, A.; Wieder, T.; Van Aken, P.; Weirich, T.; Denninger, G.; Vidal, M.; Oswald, S.; Deneke, C.; Mayer, J.; Fuess, H., An interface clusters mixture model for the structure of amorphous silicon monoxide (SiO). *J. Non-Cryst. Solids* **2003,** *320* (1-3), 255-280.

44. Brady, G. W., A study of amorphous SiO. *J. Phys. Chem.* **1959,** *63* (7), 1119-1120.

45. Philipp, H. R., Optical and bonding model for non-crystalline SiO_x and SiO_xN_y materials. *J. Non-Cryst. Solids* **1972,** *8*, 627-632.

46. Hirata, A.; Kohara, S.; Asada, T.; Arao, M.; Yogi, C.; Imai, H.; Tan, Y.; Fujita, T.; Chen, M., Atomic-scale disproportionation in amorphous silicon monoxide. *Nat. Commun.* **2016,** *7* (1), 1-7.

47. Jung, S. C.; Kim, H.-J.; Kim, J.-H.; Han, Y.-K., Atomic-level Understanding Toward a High-capacity and High-power Silicon Oxide (SiO) Material. *J. Phys. Chem. C* **2015,** *120* (2), 886-892.

48. Tan, T.; Lee, P.-K.; Denis, Y., Probing the reversibility of silicon monoxide electrodes for lithium-ion batteries. *J. Electrochem. Soc.* **2018,** *166* (3), A5210.

49. Doh, C.-H.; Park, C.-W.; Shin, H.-M.; Kim, D.-H.; Chung, Y.-D.; Moon, S.-I.; Jin, B.-S.; Kim, H.-S.; Veluchamy, A., A new SiO/C anode composition for lithium-ion battery. *J. Power Sources* **2008,** *179* (1), 367-370.

50. Choi, I.; Lee, M. J.; Oh, S. M.; Kim, J. J., Fading mechanisms of carbon-coated and disproportionated Si/SiO_x negative electrode (Si/SiO_x/C) in Li-ion secondary batteries: Dynamics and component analysis by TEM. *Electrochim. Acta* **2012,** *85*, 369-376.

51. Xiao, H.; Fang, C.; Zheng, T.; Bai, H.; Liu, G., Investigation of SiO_x anode fading mechanism with limited capacity cycling. *APL Materials* **2022,** *10* (1), 011108.

52. Lin, Z.; Li, J.; Huang, Q.; Xu, K.; Fan, W.; Yu, L.; Xia, Q.; Li, W., Insights into the Interfacial Instability between carbon-coated SiO anode and electrolyte in lithium-ion batteries. *J. Phys. Chem. C* **2019,** *123* (20), 12902-12909.

53. Nguyen, C. C.; Choi, H.; Song, S.-W., Roles of oxygen and interfacial stabilization in enhancing the cycling ability of silicon oxide anodes for rechargeable lithium batteries. *J. Electrochem. Soc.* **2013,** *160* (6), A906.

54. Li, H.; Li, H.; Yang, Z.; Yang, L.; Gong, J.; Liu, Y.; Wang, G.; Zheng, Z.; Zhong, B.; Song, Y., SiO_x Anode: From Fundamental Mechanism toward Industrial Application. *Small* **2021,** *17* (51), 2102641.

55. Shi, L.; Pang, C.; Chen, S.; Wang, M.; Wang, K.; Tan, Z.; Gao, P.; Ren, J.; Huang, Y.; Peng, H., Vertical Graphene Growth on SiO Microparticles for Stable Lithium Ion Battery Anodes. *Nano Lett.* **2017,** *17* (6), 3681-3687.

56. Xia, M.; Zhou, Z.; Su, Y.; Li, Y.; Wu, Y.; Zhou, N.; Zhang, H.; Xiong, X., Scalable Synthesis SiO@C Anode by Fluidization Thermal Chemical Vapor Deposition in Fluidized Bed Reactor for High-energy Lithium-ion Battery. *Appl. Surf. Sci.* **2019,** *467*, 298-308.

57. Liu, Z.; Zhao, Y.; He, R.; Luo, W.; Meng, J.; Yu, Q.; Zhao, D.; Zhou, L.; Mai, L., Yolk@ Shell SiO_x/C microspheres with semi-graphitic carbon coating on the exterior and interior surfaces for durable lithium storage. *Energy Storage Mater.* **2019,** *19*, 299-305.

58. Ren, Y.; Li, M., Facile synthesis of SiO_x@C composite nanorods as anodes for lithium ion batteries with excellent electrochemical performance. *J. Power Sources* **2016,** *306*, 459-466.

59. Lee, J. I.; Lee, K. T.; Cho, J.; Kim, J.; Choi, N. S.; Park, S., Chemical‐assisted thermal disproportionation of porous silicon monoxide into silicon‐based multicomponent systems. *Angew. Chem.* **2012,** *124* (11), 2821-2825.

60. Lu, Z.; Liu, N.; Lee, H.-W.; Zhao, J.; Li, W.; Li, Y.; Cui, Y., Nonfilling carbon coating of porous silicon micrometer-sized particles for high-performance lithium battery anodes. *ACS nano* **2015,** *9* (3), 2540-2547.

61. Li, H.; Zhou, H., Enhancing the Performances of Li-ion Batteries by Carbon-Coating: Present and Future. *Chem. Commun.* **2012,** *48* (9), 1201-1217.

62. Wu, J.; Cao, Y.; Zhao, H.; Mao, J.; Guo, Z., The Critical Role of Carbon in Marrying Silicon and Graphite Anodes for High‐energy Lithium‐ion Batteries. *Carbon Energy* **2019**.

63. Raccichini, R.; Varzi, A.; Passerini, S.; Scrosati, B., The Role of Graphene for Electrochemical Energy Storage. *Nat. Mater.* **2015,** *14* (3), 271-279.

64. Radich, J. G.; McGinn, P. J.; Kamat, P. V., Graphene-based Composites for Electrochemical Energy Storage. *Electrochem Soc Interface* **2011,** *20* (1), 63-66.

65. Su, F.-Y.; He, Y.-B.; Li, B.; Chen, X.-C.; You, C.-H.; Wei, W.; Lv, W.; Yang, Q.-H.; Kang, F., Could Graphene Construct an Effective Conducting Network in a High-power Lithium Ion Battery. *Nano Energy* **2012,** *1* (3), 429-439.

66. Son, I. H.; Park, J. H.; Kwon, S.; Park, S.; Rümmeli, M. H.; Bachmatiuk, A.; Song, H. J.; Ku, J.; Choi, J. W.; Choi, J.-m., Silicon Carbide-free Graphene Growth on Silicon for Lithium-ion Battery with High Volumetric Energy Density. *Nat. Commun.* **2015,** *6*, 7393.

67. Xu, Q.; Sun, J. K.; Yu, Z. L.; Yin, Y. X.; Xin, S.; Yu, S. H.; Guo, Y. G., SiOx Encapsulated in Graphene Bubble Film: An Ultrastable Li‐Ion Battery Anode. *Adv. Mater.* **2018,** *30* (25), 1707430.

68. Kucinskis, G.; Bajars, G.; Kleperis, J., Graphene in Lithium Ion Battery Cathode Materials: A Review. *J. Power Sources* **2013,** *240*, 66-79.

69. Guo, Z.; Wang, C.; Chen, M.; Li, M., Hard carbon derived from coal tar pitch for use as the anode material in lithium ion batteries. *Int. J. Electrochem. Sci* **2013,** *8* (8), 2702-2709.

70. Li, Y.; Yan, K.; Lee, H.-W.; Lu, Z.; Liu, N.; Cui, Y., Growth of Conformal Graphene Cages on Micrometre-Sized Silicon Particles as Stable Battery Anodes. *Nat. Energy* **2016,** *1* (2), 15029.

71. Bora, M.; Bhattacharjya, D.; Saikia, B. K., Coal-Derived Activated Carbon for Electrochemical Energy Storage: Status on Supercapacitor, Li-Ion Battery, and Li–S Battery Applications. *Energy & Fuels* **2021,** *35* (22), 18285-18307.

72. Ye, R.; Xiang, C.; Lin, J.; Peng, Z.; Huang, K.; Yan, Z.; Cook, N. P.; Samuel, E. L.; Hwang, C.-C.; Ruan, G., Coal as an Abundant Source of Graphene Quantum Dots. *Nat. Commun.* **2013,** *4* (1), 1-7.

73. Ghani, M.; Rajoka, M.; Akhtar, K., Investigations in fungal solubilization of coal: Mechanisms and significance. *Biotechnology and bioprocess engineering* **2015,** *20* (4), 634-642.

74. Yao, Z.; Ji, X.; Sarker, P.; Tang, J.; Ge, L.; Xia, M.; Xi, Y., A comprehensive review on the applications of coal fly ash. *Earth-Sci. Rev.* **2015,** *141*, 105-121.

75. Blissett, R.; Rowson, N., A review of the multi-component utilisation of coal fly ash. *Fuel* **2012,** *97*, 1-23.

76. Jiang, Y.; Zhang, Y.; Yan, X.; Tian, M.; Xiao, W.; Tang, H., A sustainable route from fly ash to silicon nanorods for high performance lithium ion batteries. *Chem. Eng. J.* **2017,** *330*, 1052-1059.

77. Miyachi, M.; Yamamoto, H.; Kawai, H.; Ohta, T.; Shirakata, M., Analysis of SiO Anodes for Lithium-ion Batteries. *J. Electrochem. Soc.* **2005,** *152* (10), A2089-A2091.

78. Yasuda, K.; Kashitani, Y.; Kizaki, S.; Takeshita, K.; Fujita, T.; Shimosaki, S., Thermodynamic Analysis and Effect of Crystallinity for Silicon Monoxide Negative Electrode for Lithium Ion Batteries. *J. Power Sources* **2016,** *329*, 462-472.

79. Kim, J.-H.; Park, C.-M.; Kim, H.; Kim, Y.-J.; Sohn, H.-J., Electrochemical behavior of SiO anode for Li secondary batteries. *J. Electroanal. Chem.* **2011,** *661* (1), 245-249.

80. Sepehri-Amin, H.; Ohkubo, T.; Kodzuka, M.; Yamamura, H.; Saito, T.; Iba, H.; Hono, K., Evidence for nano-Si clusters in amorphous SiO anode materials for rechargeable Li-ion batteries. *Scr. Mater.* **2013,** *69* (1), 92-95.

81. Feroughi, O.; Sternemann, C.; Sahle, C. J.; Schroer, M.; Sternemann, H.; Conrad, H.; Hohl, A.; Seidler, G.; Bradley, J.; Fister, T., Phase separation and Si nanocrystal formation in bulk SiO studied by x-ray scattering. *Appl. Phys. Lett.* **2010,** *96* (8), 081912.

82. Sasikala, S. P.; Henry, L.; Yesilbag Tonga, G.; Huang, K.; Das, R.; Giroire, B.; Marre, S.; Rotello, V. M.; Penicaud, A.; Poulin, P., High Yield Synthesis of Aspect Ratio Controlled Graphenic Materials from Anthracite Coal in Supercritical Fluids. *ACS Nano* **2016,** *10* (5), 5293-5303.

83. Ikeya, K.; Sleighter, R. L.; Hatcher, P. G.; Watanabe, A., Characterization of the Chemical Composition of Soil Humic Acids Using Fourier Transform Ion Cyclotron Resonance Mass Spectrometry. *Geochim. Cosmochim. Acta* **2015,** *153*, 169-182.

84. Stevenson, F. J., *Structural Basis of Humic Substances. Humus chemistry: genesis, composition, reactions*. John Wiley & Sons: New Jersey, **1994**; p 287-294.

85. Powell, C.; Beall, G. W., Graphene oxide and graphene from low grade coal: Synthesis, characterization and applications. *Curr Opin Colloid Interfa.* **2015,** *20* (5-6), 362-366.

86. El-shazly, M. D.; Henderson, B.; Beall, G. W., Reduced Humic Acid Nanosheets and its Uses as Nanofiller. *J. Phys. Chem. Solids* **2015,** *85*, 86-90.

87. Li, Q.; Liu, X.; Han, X.; Xiang, Y.; Zhong, G.; Wang, J.; Zheng, B.; Zhou, J.; Yang, Y., Identification of the Solid Electrolyte Interface on the Si/C Composite Anode with FEC as the Additive. *ACS Appl. Mater. Interfaces* **2019,** *11* (15), 14066-14075.

88. Wang, J.; Zhou, J.; Hu, Y.; Regier, T., Chemical Interaction and Imaging of Single Co3O4/Graphene Sheets Studied by Scanning Transmission X-Ray Microscopy and X-Ray Absorption Spectroscopy. *Energy Environ. Sci.* **2013,** *6* (3), 926-934.

89. El-Kady, M. F.; Shao, Y.; Kaner, R. B., Graphene for Batteries, Supercapacitors and Beyond. *Nat. Rev. Mater.* **2016,** *1* (7), 1-14.

90. Chang, W.-C.; Ma, C.-C. M.; Tai, N.-H.; Chen, C.-B., Effects of Processing Methods and Parameters on the Mechanical Properties and Microstructure of Carbon/Carbon Composites. *J. Mater. Sci.* **1994,** *29* (22), 5859-5867.

91. Choi, S. H.; Nam, G.; Chae, S.; Kim, D.; Kim, N.; Kim, W. S.; Ma, J.; Sung, J.; Han, S. M.; Ko, M., Robust Pitch on Silicon Nanolayer–Embedded Graphite for Suppressing Undesirable Volume Expansion. *Adv. Energy Mater.* **2019,** *9* (4), 1803121.

92. Park, C.-M.; Choi, W.; Hwa, Y.; Kim, J.-H.; Jeong, G.; Sohn, H.-J., Characterizations and Electrochemical Behaviors of Disproportionated SiO and its Composite for Rechargeable Li-Ion Batteries. *J. Mater. Chem.* **2010,** *20* (23), 4854-4860.

93. David, L.; Bhandavat, R.; Barrera, U.; Singh, G., Silicon Oxycarbide Glass-graphene Composite Paper Electrode for Long-cycle Lithium-ion Batteries. *Nat. Commun.* **2016,** *7*, 10998.

94. Wang, F.; Wang, B.; Ruan, T.; Gao, T.; Song, R.; Jin, F.; Zhou, Y.; Wang, D.; Liu, H.; Dou, S., Construction of structure-tunable Si@void@C anode materials for lithium-ion batteries through controlling the growth kinetics of resin. *ACS Nano* **2019,** *13* (10), 12219-12229.

95. Huang, X.; Li, M., Multi-channel and Porous SiO@N-doped C Rods as Anodes for High-performance Lithium-ion Batteries. *Appl. Surf. Sci.* **2018,** *439*, 336-342.

96. Qiao, R.; Chuang, Y.-D.; Yan, S.; Yang, W., Soft X-ray irradiation effects of Li_2O_2, Li_2CO_3 and Li_2O revealed by absorption spectroscopy. *PloS one* **2012,** *7* (11).

97. Shin, J.-S.; Han, C.-H.; Jung, U.-H.; Lee, S.-I.; Kim, H.-J.; Kim, K., Effect of Li_2CO_3 Additive on Gas Generation in Lithium-ion Batteries. *J. Power Sources* **2002,** *109* (1), 47-52.

98. Xia, M.; Li, Y.; Zhou, Z.; Wu, Y.; Zhou, N.; Zhang, H.; Xiong, X., Improving the Electrochemical Properties of SiO@C Anode for High-Energy Lithium Ion Battery by Adding Graphite through Fluidization Thermal Chemical Vapor Deposition Method. *Ceram. Int.* **2019,** *45* (2), 1950-1959.

99. Luo, J.; Ma, B.; Peng, J.; Wu, Z.; Luo, Z.; Wang, X., Modified Chestnut-like Structure Silicon Carbon Composite as Anode Material for Lithium-Ion Batteries. *ACS Sustainable Chem. Eng.* **2019,** *7* (12), 10415-10424.

100. Tian, H.; Tan, X.; Xin, F.; Wang, C.; Han, W., Micro-sized Nano-porous Si/C Anodes for Lithium Ion Batteries. *Nano Energy* **2015,** *11*, 490-499.

101. Xu, S.; Zhou, J.; Wang, J.; Pathiranage, S.; Oncel, N.; Robert Ilango, P.; Zhang, X.; Mann, M.; Hou, X., In Situ Synthesis of Graphene‐Coated Silicon Monoxide Anodes from Coal‐Derived Humic Acid for High‐Performance Lithium‐Ion Batteries. *Adv. Funct. Mater.* **2021,** *31* (32), 2101645.

102. Kasrai, M.; Yin, Z.; Bancroft, G. M.; Tan, K. H., X‐ray fluorescence measurements of X‐ray absorption near edge structure at the Si, P, and SL edges. *J. Vac. Sci. Technol* **1993,** *11* (5), 2694-2699.

103. Wang, D.; Zuin, L., Li K-edge X-ray absorption near edge structure spectra for a library of lithium compounds applied in lithium batteries. *J. Power Sources* **2017,** *337,* 100-109.

104. Zhang, Y.; Tang, Y.; Lam, C.; Wang, N.; Lee, C.; Bello, I.; Lee, S., Bulk-quantity Si nanowires synthesized by SiO sublimation. *J. Cryst. Growth* **2000,** *212* (1-2), 115-118.

105. Dewald, W.; Borschel, C.; Stichtenoth, D.; Niermann, T.; Ronning, C., Phase diagram of Si nanowire growth by disproportionation of SiO. *J. Cryst. Growth* **2010,** *312* (10), 1751-1754.

106. Zhang, R.; Zhao, M.; Lee, S., Silicon monoxide clusters: the favorable precursors for forming silicon nanostructures. *Phys. Rev. Lett.* **2004,** *93* (9), 095503.

107. Kitada, K.; Pecher, O.; Magusin, P. C.; Groh, M. F.; Weatherup, R. S.; Grey, C. P., Unraveling the reaction mechanisms of SiO anodes for Li-ion batteries by combining in situ ^{7}Li and ex situ ^{7}Li/^{29}Si solid-state NMR spectroscopy. *J. Am. Chem. Soc.* **2019,** *141* (17), 7014-7027.

108. Dorofeev, S.; Ischenko, A.; Kononov, N.; Fetisov, G., Effect of annealing temperature on the optical properties of nanosilicon produced from silicon monoxide. *Curr Appl Phys* . **2012,** *12* (3), 718-725.

109. Wang, J.; Wang, X.; Liu, B.; Lu, H.; Chu, G.; Liu, J.; Guo, Y.-G.; Yu, X.; Luo, F.; Ren, Y., Size effect on the growth and pulverization behavior of Si nanodomains in SiO anode. *Nano Energy* **2020,** *78*, 105101.

110. Tepper, T.; Berger, S., Correlation between microstructure, particle size, dielectric constant, and electrical resistivity of nano-size amorphous SiO_2 powder. *Nanostruct. Mater.* **1999,** *11* (8), 1081-1089.

111. Long, Z.; Fu, R.; Ji, J.; Feng, Z.; Liu, Z., Unveiling the Effect of Surface and Bulk Structure on Electrochemical Properties of Disproportionated SiO_x Anodes. *ChemNanoMat* **2020,** *6* (7), 1127-1135.

112. Li, W.; Tang, R.; Yuan, B.; Wang, Y.; Sun, T., A study of CNT fiber-reinforced multi-carbon resource-coated SiO x composite as anode materials. *J. Mater. Sci.* **2020,** *55* (14), 6005-6016.

113. Yao, Y.; Zhang, J.; Xue, L.; Huang, T.; Yu, A., Carbon-coated SiO_2 nanoparticles as anode material for lithium ion batteries. *J. Power Sources* **2011,** *196* (23), 10240-10243.

114. Qiao, R.; Chuang, Y.-D.; Yan, S.; Yang, W., Soft X-ray Irradiation Effects of Li_2O_2, Li_2CO_3 and Li_2O Revealed by Absorption Spectroscopy. *PloS one* **2012,** *7* (11), e49182.

115. Kasrai, M.; Lennard, W.; Brunner, R.; Bancroft, G.; Bardwell, J.; Tan, K., Sampling depth of total electron and fluorescence measurements in Si L-and K-edge absorption spectroscopy. *Appl. Surf. Sci.* **1996,** *99* (4), 303-312.

116. Zhou, J.; Hu, Y.; Li, X.; Wang, C.; Zuin, L., Chemical bonding in amorphous Si-coated carbon nanotubes as anodes for Li ion batteries: a XANES study. *RSC Adv.* **2014,** *4* (39), 20226-20229.

117. Kumar, R.; Jain, H.; Chaudhary, A.; Kumari, S.; Mondal, D.; Srivastava, A., Thermal conductivity and fire-retardant response in graphite foam made from coal tar pitch derived semi coke. *Compos. B: Eng.* **2019,** *172*, 121-130.

118. Yu, M.; Zhong, C.; Zhang, Y.; Chen, Q.-l.; Ao, X.; Lei, X.; Li, C., Pyrolysis behavior and chemical composition of the precursors influence on structure and properties of coal-tar-pitch-based carbon foams. *J. Anal. Appl. Pyrolysis.* **2018,** *134*, 293-300.

119. Wang, D.; Wang, Y.; Chen, Y.; Liu, W.; Wang, H.; Zhao, P.; Li, Y.; Zhang, J.; Dong, Y.; Hu, S., Coal tar pitch derived N-doped porous carbon nanosheets by the in-situ formed g-C_3N_4 as a template for supercapacitor electrodes. *Electrochim. Acta* **2018,** *283*, 132-140.

120. Xing, B.; Zhang, C.; Liu, Q.; Zhang, C.; Huang, G.; Guo, H.; Cao, J.; Cao, Y.; Yu, J.; Chen, Z., Green synthesis of porous graphitic carbons from coal tar pitch templated by nano-$CaCO_3$ for high-performance lithium-ion batteries. *J. Alloys Compd.* **2019,** *795*, 91-102.

121. Zhao, Q.; Xie, H.; Ning, H.; Liu, J.; Zhang, H.; Wang, L.; Wang, X.; Zhu, Y.; Li, S.; Wu, M., Intercalating petroleum asphalt into electrospun ZnO/Carbon nanofibers as enhanced free-standing anode for lithium-ion batteries. *J. Alloys Compd.* **2018,** *737*, 330-336.

122. Wang, Y.-X.; Chou, S.-L.; Kim, J. H.; Liu, H.-K.; Dou, S.-X., Nanocomposites of silicon and carbon derived from coal tar pitch: cheap anode materials for lithium-ion batteries with long cycle life and enhanced capacity. *Electrochim. Acta* **2013,** *93*, 213-221.

123. Liu, Y.; Li, P.; Wang, Y.; Liu, J.; Wang, Y.; Zhang, J.; Wu, M.; Qiu, J., A green and template recyclable approach to prepare Fe_3O_4/porous carbon from petroleum asphalt for lithium-ion batteries. *J. Alloys Compd.* **2017,** *695*, 2612-2618.

124. Park, C.-M.; Kim, J.-H.; Kim, H.; Sohn, H.-J., Li-alloy based anode materials for Li secondary batteries. *Chem. Soc. Rev.* **2010,** *39* (8), 3115-3141.

125. Ma, D.; Cao, Z.; Hu, A., Si-based anode materials for Li-ion batteries: a mini review. *Nano-Micro Letters* **2014,** *6* (4), 347-358.

126. Li, Y.; Yan, K.; Lee, H.-W.; Lu, Z.; Liu, N.; Cui, Y., Growth of conformal graphene cages on micrometre-sized silicon particles as stable battery anodes. *Nat. Energy* **2016,** *1* (2), 1-9.

127. Parr, S. W. *The classification of coal*; University of Illinois at Urbana Champaign, College of Engineering …: 1928.

128. Stevenson, F. J., *Humus chemistry: genesis, composition, reactions*. John Wiley & Sons: **1994**.

129. Powell, C.; Beall, G. W., Graphene Oxide and Graphene from Low Grade Coal: Synthesis, Characterization and Applications. *Curr. Opin. Colloid Interface Sci.* **2015,** *20* (5-6), 362-366.

130. Beall, G. W.; Duraia, E.-S. M.; Yu, Q.; Liu, Z., Single crystalline graphene synthesized by thermal annealing of humic acid over copper foils. *Physica E Low Dimens. Syst. Nanostruct.* **2014,** *56*, 331-336.

131. Vehring, R., Pharmaceutical particle engineering via spray drying. *Pharmaceutical research* **2008,** *25* (5), 999-1022.

132. Cui, J.; Cui, Y.; Li, S.; Sun, H.; Wen, Z.; Sun, J., Microsized Porous SiO x@ C Composites Synthesized through Aluminothermic Reduction from Rice Husks and Used as Anode for Lithium-Ion Batteries. *ACS Appl. Mater. Interfaces* **2016,** *8* (44), 30239-30247.

133. Gollakota, A. R.; Volli, V.; Shu, C.-M., Progressive utilisation prospects of coal fly ash: A review. *Sci. Total Environ.* **2019,** *672*, 951-989.

134. El-Mogazi, D.; Lisk, D. J.; Weinstein, L. H., A review of physical, chemical, and biological properties of fly ash and effects on agricultural ecosystems. *Sci. Total Environ.* **1988,** *74*, 1-37.

135. Xing, A.; Zhang, J.; Wang, R.; Wang, J.; Liu, X., Fly ashes as a sustainable source for nanostructured Si anodes in lithium-ion batteries. *SN Appl. Sci.* **2019,** *1* (2), 181.

136. Li, F.; Liu, Q.; Li, M.; Fang, Y., Understanding fly-ash formation during fluidized-bed gasification of high-silicon-aluminum coal based on its characteristics. *Energy* **2018,** *150*, 142-152.

137. Gao, Q.; Li, S.; Xu, Y.; Liu, J., A general mechanistic model of fly ash formation during pulverized coal combustion. *Combust. Flame* **2019,** *200*, 374-386.

138. Hinch, E., Sedimentation of small particles. In *Disorder and Mixing*, Springer: **1988**; pp 153-162.